

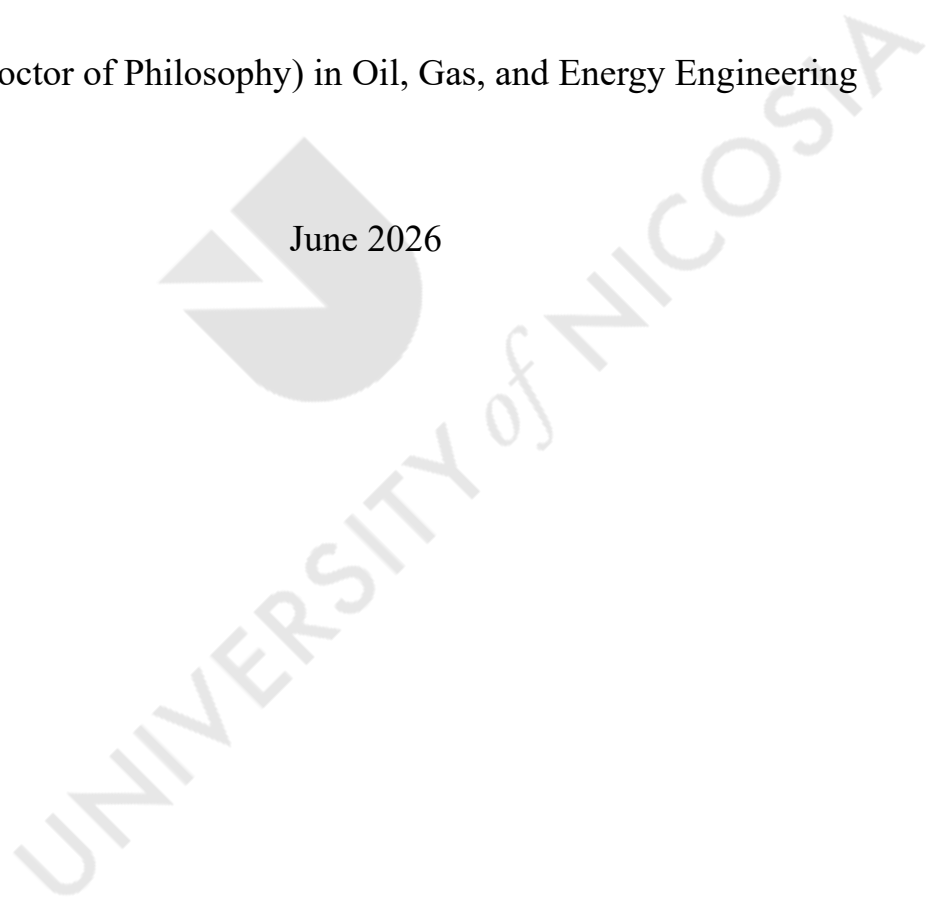
UNIVERSITY OF NICOSIA

Multiscale Modelling of Arsenic Behaviour in Carbonate Aquifers

Ms Jumana Sharanik

PhD (Doctor of Philosophy) in Oil, Gas, and Energy Engineering

June 2026



Jumana Sharanik

NICOSIA
PhD
2026


UNIVERSITY of NICOSIA



UNIVERSITY *of* NICOSIA

Multiscale Modelling of Arsenic Behaviour in Carbonate Aquifers

Ms Jumana Sharanik

A thesis submitted to the University of Nicosia in accordance with the requirements of the degree of PhD (Doctor of Philosophy) in Oil, Gas and Energy Engineering

Department of Engineering

June 2026

Abstract

Chronic exposure to arsenic, primarily from groundwater sources, constitutes a major global public health concern owing to the skin lesions and cancer it can cause. Arsenic transport and retention in carbonate aquifers were investigated using an integrated combination of micro-CT, digital rock physics, and multiscale reactive transport modelling. Focusing on carbonate-rich groundwater systems of Cyprus, this study yields new insights into how pore-scale structure, hydrodynamic forcing, and solid-phase contamination history control arsenic mobilisation under pumping conditions. High-resolution micro-CT imaging was used to characterise pore geometry and generate image-based permeability maps, which were incorporated into CrunchFlow simulations transcending the pore- (μm), core- (mm), and aquifer-scale (m) scales. The simulations revealed a pronounced spatial scale dependence in arsenic behaviour. At the metre level, increasing pumping rates raised outlet arsenic concentrations from $\sim 3.5 \mu\text{g/L}$, at 0.36 L/h , to $\sim 17.5 \mu\text{g/L}$, at $1,800 \text{ L/h}$, exceeding the World Health Organization drinking-water guideline threshold of $10 \mu\text{g/L}$, while adsorption onto the solid matrix declined from $\sim 39 \mu\text{g}$ to $\sim 24 \mu\text{g}$. Finer-scale domains exhibited substantially greater sensitivity, with aqueous concentrations approaching $\sim 30 \mu\text{g/L}$, which is about threefold the WHO recommendation, while retained inventories dropped $\sim 12 \mu\text{g}$, at high flow rates.

The amount of arsenic initially stored in the rock matrix controlled the concentration of arsenic measured in groundwater. Increasing the initial amount of $\text{Ca}_3(\text{AsO}_4)_2$ content from 20% to 60% and 100% consistently produced higher aqueous arsenic concentrations (up to $\sim 18\%$) across all spatial scales, indicating control by solid-phase availability rather than extensive mineral dissolution. Desorption-focused simulations showed rapid elevations in concentration with pumping rates, peaking near $\sim 17.7 \mu\text{g/L}$ before reaching residence-time-controlled plateaus. Long-term dilution scenarios (500 L/h over 50 years) lowered dissolved arsenic by $\sim 20\text{--}25\%$ but marginally tempered solid-phase inventories ($\leq 2\%$), indicating that the carbonate matrix acts as a persistent but reversible arsenic sink.

To assess transboundary environmental impacts, a multiphase-flow analysis of the September 2022 Nord Stream pipeline leak was conducted. The study estimated a methane release of 478,000 tonnes, making it one of the largest methane emission events in recent history. Results showed that around 63% of the total methane was released within the first 48 hours due to the high-pressure difference between the pipelines and the surrounding seawater.

Keywords: Porosity-permeability relationship; Arsenic behaviour; hydrogeochemical reactions; reactive transport modelling; carbonate-rich aquifers; CrunchFlow; Avizo; Particula1.3; Digital rock physics; Multiscale modelling.



Acknowledgments

Firstly, I would like to express my special appreciation and thanks to my advisor, **Professor Constantinos Hadjistassou**, for his valuable guidance, encouragement, and continuous support of my Ph.D. studies and related research. His patience, motivation, and immense knowledge have been invaluable throughout my research and the writing of this thesis.

I would also like to sincerely thank **Professor Anastasis Polycarpou** and **Dr Natalia Kovalchuk** for their insightful questions, constructive comments, and valuable discussions, which helped me broaden my perspective and strengthen the quality of my research. I am also grateful to Ms Chrysanthi Papaioannou for her excellent coordination and support, and to Agios Therissos for providing the micro-CT facilities and supporting the research.

I would like to extend my sincere gratitude to the members of my defence committee: chair of the defence committee, **Professor Marios Nestoros**, Internal Examiner, **Professor Nectarios Papanicolaou** and External Examiner, **Professor Wael Hamd**, Chemical Engineering Department, University of Balamand, for their time, careful evaluation, and valuable feedback on this work.

This research has been supported by the Cyprus Research and Innovation Foundation (RIF) under the project protocol number: CONCEPT-HYDRO/0421/0002, which partly funded the FabRocks project.

Finally, I would like to express my deepest appreciation to my beloved husband, **Ali**, whose unwavering support, patience, and encouragement sustained me throughout this journey.

Declaration

I declare that the work in this thesis was carried out in accordance with the regulations of the University of Nicosia. This thesis has been composed solely by me except where stated otherwise by reference or acknowledgment. It has not been previously submitted, in whole or in part, to this or any other institution for a degree, diploma or other qualifications.

Signed:



Date: 08/06/2026



Table of Contents

Abstract	i
Acknowledgments.....	iii
Declaration.....	iv
Nomenclature.....	viii
List of Figures.....	xi
List of Tables.....	xiv
List of Publications	xv
1 Introduction.....	2
1.1 Problem Definition.....	4
1.2 Research Objectives.....	5
1.3 Thesis Outline	6
2 Theoretical Background.....	9
2.1 Porous Media and Fluid Flow in Geological Systems.....	9
2.2 Sedimentary Rocks: Sandstones and Carbonates	11
2.2.1 Sandstones.....	12
2.2.2 Carbonates.....	12
2.2.3 Petrophysical and Hydraulic Characteristics of Sandstones and Carbonates	13
2.3 Image-Based Characterisation of Porous Media: The Role of DRP.....	16
2.3.1 Fundamentals of Digital Rock Physics.....	16
2.3.2 Imaging and Visualisation Techniques.....	17
2.3.3 Advantages and Limitations.....	17
3 Literature Review.....	20
3.1 Water Scarcity and Groundwater Use in Cyprus	20
3.2 Arsenic in Groundwater: Sources and Risks.....	22
3.2.1 Environmental Policy Framework and Arsenic Monitoring in Cyprus	23
3.3 Global Overview of Arsenic in Groundwater	24
3.4 Geochemical Mechanisms of Arsenic Speciation and Transport.....	27
3.4.1 Arsenic-Calcite Interactions.....	30
3.5 Numerical and Computational Approaches to Arsenic Mobility.....	31
3.6 Multiscale Modelling and Image-Based Approaches	32
3.7 Knowledge Gaps and Research Needs	33
4 Materials and Methods.....	36
4.1 Methodological Framework of the FabRocks Project	36

4.1.1 Geological Settings	37
4.1.2 Experimental Measurement of Porosity and Permeability	40
4.1.3 Micro-CT scans of Sandstone and Carbonate Rocks.....	43
4.1.4 Image-Based Rock Characterisation and Pore-Scale Modelling	44
4.1.5 Synthetic Sediment Pack Modelling (DEM Approach).....	46
4.2 Framework of Arsenic Behaviour in Carbonate-Rich Aquifers.....	48
4.2.1 Analytical Techniques	49
4.2.1.1 X-ray Fluorescence (XRF)-based Chemical Composition	49
4.2.1.2 X-ray Diffraction (XRD)-based Chemical Composition.....	52
4.2.2 Generation of 2D Domains from Imaging Data for Numerical Modelling	54
4.2.2.1 Nuclear Magnetic Resonance (NMR) Imaging	54
4.2.2.2 Optical Thin Sectioning	55
4.2.2.3 Hydraulic Conductivity Mapping	56
4.2.3 Domain Geometry and Mesh.....	56
4.2.4 Simulating Arsenic Mobility and Retention Using Crunchflow.....	59
4.2.4.1 Mass Balance Equation.....	59
4.2.4.2 Surface complexation.....	60
4.2.4.3 Precipitation and Dissolution of Arsenic	61
4.2.5 Arsenic Contamination Scenarios	62
4.2.6 Model Development and Reactive Transport Framework	64
4.3 Framework for Modelling Methane Leakage from Nord Stream Pipelines	66
5 Research Findings.....	70
5.1 Results and Analysis of Rock Characterisation	70
5.1.1 Experimentally Determined Porosities and Permeabilities.....	70
5.1.2 The Porosity-Permeability Relationship in Sandstone Cores	72
5.1.3 Gas Volumetric Flow Rate-Permeability Relationship in Sandstone Cores	73
5.1.4 Gas Volumetric Flow Rate-Porosity Relationship in Sandstone Cores	76
5.1.5 Storage Capacity-Porosity Relationship in Sandstone Packs	76
5.1.6 The Impact of Granular Roundness on Storage Capabilities.....	78
5.2 Results and Interpretation of Arsenic Transport Behaviour.....	79
5.2.1 Effect of Flow Rate on Arsenic Transport Across Scales	79
5.2.2 Influence of the Rock Matrix Contamination Level.....	83
5.2.3 Validation of Arsenic Release Through Desorption Analysis.....	85
5.2.4 Arsenic Removal Under Dilution Conditions	86
5.2.5 Arsenic Retention to Rock Matrix	88

5.2.6 Effect of Flow Rate on Arsenic Retained Across Scales	89
5.2.7 Influence of the Rock Matrix Contamination Level	91
5.2.8 Arsenic Retention Under Dilution Conditions	94
5.2.9 Numerical Robustness and Model Verification	96
5.3 Methane Release from the Nord Stream Pipeline System	98
6 Conclusions	101
6.1 Concluding Remarks	101
6.2 Future Research Directions	103
References	106



Nomenclature

a_i	Activity of species i	
As(III)	Arsenite oxidation state of arsenic	
As(V)	Arsenate oxidation state of arsenic	
Ba	Barium (trace element, XRF)	mg/kg
Ca^{2+}	Calcium ion (aqueous)	
$\text{Ca}_3(\text{AsO}_4)_2$	Calcium arsenate (solid contaminant phase)	
CaCO_3	Calcite (solid mineral)	
$\text{CaHAsO}_3(\text{s})$	Calcium hydrogen arsenite (solid)	
$\text{CaHAsO}_4(\text{s})$	Calcium hydrogen arsenate (solid)	
$\text{CaH}_2\text{AsO}_4^+$	Calcium dihydrogen arsenate (aqueous complex)	
Cd	Cadmium (trace element, XRF)	mg/kg
CFD	Computational Fluid Dynamics	
C_i	Concentration of species i in the fluid phase	mol/L (or mg/L)
COMSOL	COMSputer and SOLution Multiphysics (simulation platform)	
CO_3^{2-}	Carbonate ion (aqueous)	
Cr	Chromium (trace element, XRF)	mg/kg
CrunchFlow	Reactive-transport simulator used	
CT	Computed Tomography (e.g., micro-CT)	
Cu	Copper (trace element, XRF)	mg/kg
D	Hydrodynamic dispersion coefficient/tensor	m^2/s
D_m	Molecular diffusion coefficient	m^2/s
EEA	European Environment Agency	
Eh (EH)	Redox potential	V
F	Faraday constant	C/mol
Fe	Iron (element)	
Fe(II)	Ferrous iron	
Fe(III)	Ferric iron	
γ_i	Activity coefficient of species i	
H^+	Proton	
H_2AsO_4^-	Arsenate species (circumneutral pH)	
H_3AsO_3	Arsenous acid (dominant As(III) at $\text{pH} < \sim 9$)	
HAsO_4^{2-}	Arsenate species (more alkaline pH)	
HYTEC	Hydro-geochemical / reactive-transport simulator	
I	Ionic strength	mol/L
K	Equilibrium constant	

K^0	Intrinsic equilibrium constant	
K_{sp}	Solubility product (e.g., $\text{CaCO}_3 \approx 10^{-8.48}$; $\text{CaHAsO}_4(\text{s}) \approx 10^{-6.5}$; $\text{CaHAsO}_3(\text{s}) \approx 10^{-7.4}$)	
L/h	Liters per hour (flow-rate unit)	L/h
L/s	Liters per second (flow-rate unit)	L/s
LOQ	Limit of quantitation (analytical)	method-dependent
M	Metre (length; domain scale)	M
MATLAB	MATrix LABoratory	
Mm	Millimetre (length; domain scale)	Mm
NMR	Nuclear Magnetic Resonance (imaging)	
Nb	Niobium (trace element, XRF)	mg/kg
Ni	Nickel (trace element, XRF)	mg/kg
Π	Product operator (law of mass action)	
pH	$-\log_{10}(a_{\text{H}^+})$	
Pb	Lead (trace element, XRF)	mg/kg
PFLOTRAN	Parallel FLOW and TRANsport	
Ψ	Surface potential (electrostatic term)	V
Q	Darcy flux (specific discharge)	m/s
R	Universal gas constant	J/mol·K
R_i	Net reaction rate of species i (sum of all phases)	mol/L·s
$R_{aq,i}$	Aqueous-phase reaction rate of species i	mol/L·s
$R_{min,i}$	Mineral reaction rate (dissolution/precipitation) of species i	mol/L·s
$R_{surf,i}$	Surface reaction rate (adsorption/desorption) of species i	mol/L·s
Rb	Rubidium (trace element, XRF)	mg/kg
P	Fluid mass density	kg/m ³
SI	Saturation index = $\log \Omega$	
Sr	Strontium (trace element, XRF)	mg/kg
T	Absolute temperature	K
TOUGHREACT	Reactive-transport simulator	
$\nabla \cdot$	Divergence vector operator applied to velocity vector	
∇P	Pressure gradient.	Pa
μ	Fluid dynamic viscosity	Pa·s
∇^2	Laplacian operator	
dP	Infinitesimal pressure drop	Pa

Q	Global flow rate	m^3/s
A_t	Pore throat area	m^2
ℓ_t	Length of pore throat	M
α_t	Shape factor	
N	Stoichiometric coefficient	
Ω	Saturation state (ion-activity product/ K_{sp})	
Φ	Porosity of the porous medium	
$\partial/\partial t$	Temporal derivative	s^{-1} (operator)
V	Vanadium (trace element, XRF)	mg/kg
WHO	World Health Organization	
XRD	X-ray diffraction	
XRF	X-ray fluorescence	
Zn	Zinc (trace element, XRF)	mg/kg
Zr	Zirconium (trace element, XRF)	mg/kg
z_i	Ionic charge of species i	
μ	Metric prefix “micro” (10^{-6})	
$\mu\text{g/L}$	Micrograms per litre (aqueous-concentration unit)	$\mu\text{g/L}$
μm	Micrometre (length; domain scale)	μm

List of Figures

Figure 2.1: Thin-section photomicrograph of a sandstone showing a framework of quartz grains and intergranular pore spaces. Blue arrows indicate detrital quartz grains, red arrows highlight pore-filling cement and partially occluded pore throats, and green arrows mark preserved intergranular porosity. Scale bar = 100 μm . Adapted from: Liang et al. (2020).	9
Figure 2.2: A typical digital rock workflow. Adapted from: Varfolomeev et al. (2019).....	16
Figure 3.1: Global prediction of the distribution of arsenic in groundwater. Adapted from: Podgorski and Berg (2020).	25
Figure 3.2: Eh–pH diagram for the system As-O-H, at 25°C, and 1 bar. Arsenic concentration is set at 10^{-6} M. The gray shaded area denotes the solid phase. Adapted from: Lu and Zhu (2011).....	27
Figure 3.3: Eh–pH diagrams for the system As-O-H-Fe, at 25°C, and 1 bar. Adapted from: Randall et al. (2001).....	29
Figure 4.1: Integrated experimental and digital workflow for petrophysical characterisation and 3D rock modelling.....	37
Figure 4.2: Stratigraphic columns of the (a) Kantou, (b) Agios Theodoros, (c) Xylophagou, and (d) Tochni sections, illustrating the sampled sandstone and carbonate outcrops.....	38
Figure 4.3: Geological map of Cyprus displaying the four sampling locations.	39
Figure 4.4: Workflow of core sample preparation, including coring, cutting, and drying done at the petrophysics laboratory of the University of Nicosia.	41
Figure 4.5: Representative DICOM images of carbonate (X2) and sandstone (T1 & A.T.S1) rock cores, showing cross-sectional views (top and bottom) and a longitudinal section (middle). Measured core dimensions are indicated, highlighting differences in internal pore structure and heterogeneity between carbonate and sandstone lithologies.....	43
Figure 4.6: Flowchart depicting the process for computing the rock porosity (volume fraction) and permeability, via the Avizo (2019.1) image analysis software.	44
Figure 4.7: Creation of unconsolidated sand packs using the Particula 1.3 software.....	47
Figure 4.8: Segmentation of an unconsolidated material pack using the Avizo analysis and visualisation tool, showing 3D reconstruction and orthogonal views (XY, XZ, YZ) of the pore structure.....	48
Figure 4.9: XRD diffractogram of sample C459 showing major peaks of calcite (red) and quartz (blue).	53
Figure 4.10: NMR-derived microscale image of C459 sample showing pore-solid differentiation. Scale: 1cm = 1.75 μm	55
Figure 4.11: Thin section micrograph of a carbonate rock (sample C459) showing pore types and mineral matrix. Scale: 1cm = 125 μm	56
Figure 4.12: Permeability maps across different spatial scales: (a) Micrometre scale, (b) Millimetre scale, and (c) Metre scale representations showing spatial variability in permeability (m^2). The colour gradient from blue to red indicates increasing permeability values, with corresponding scales expressed in scientific notation.	58

Figure 4.13: Reactive transport model of arsenic in groundwater under pump-induced upward flow, in a 2D porous medium.....	65
Figure 4.14: Rendering of a breached cross-section of the Nord Stream 2 pipeline displaying the concurrent leakage of gas out of the pipeline and the line seawater flooding during the early stages of the leak Drawing not to scale.....	67
Figure 5.1: Relationship between porosity and permeability for sandstone natural cores. The blue dots correspond to natural sandstone cores (T1, K1, A.T.S2, A.T.C1, and A.T.C2). The black line represents the best-fit linear regression through these cores' values.....	73
Figure 5.2: Correlation between the natural gas flow rate and the pressure gradient ΔP for a sandstone natural core (K1). The blue dots are measured data points whereas the red line is their linear regression.....	74
Figure 5.3: Magnitude between the gas flow rate and permeability for sandstone natural cores.....	75
Figure 5.4: Relationship between natural gas flow rate and porosity for the sandstone natural cores. The blue dots correspond to natural sandstone cores (T1, K1, A.T.S2, A.T.C1, and A.T.C2). The black line represents the best-fit linear regression through these cores' values.....	76
Figure 5.5: Variation of the gas volume inventory relative to the rock porosity for sand packs. The blue dots are the measured gas volumes for seven different sand packs while the red line is the linear regression of the recorder data.	78
Figure 5.6: Arsenic concentration in pumped water ($\mu\text{g/L}$) as a function of the pumping rate for different porous media scales (μm , mm , m) where rock matrix contamination is set at 20%.	80
Figure 5.7: Arsenic concentrations in pumped water as a function of pumping rate across three spatial scales (μm , mm , m) for two levels of rock matrix arsenic contamination: a) 60% and b) 100%.	82
Figure 5.8: Influence of rock matrix and Arsenic contamination level on arsenic concentrations in pumped water, at three spatial scales of μm , mm and m	84
Figure 5.9: Arsenic released via desorption at varying pumping rates across spatial scales (μm , mm and m).	85
Figure 5.10: Long-term effect of dilution on arsenic concentrations in pumped water at 500 L/h, at the metre scale considering initial concentrations of $[\text{As}] = 20 \mu\text{g/L}$ under normal flow and $[\text{As}] = 4 \mu\text{g/L}$ and diluted flow conditions.	87
Figure 5.11: Long-term effect of dilution on arsenic concentrations in pumped water, at 500 L/h for the micrometre and the millimetre scales considering initial concentrations of $[\text{As}] = 20 \mu\text{g/L}$ under normal flow and $[\text{As}] = 4 \mu\text{g/L}$ and diluted flow conditions.	88
Figure 5.12: Arsenic mass retained to rock matrix (μg) as a function of the pumping rate for different porous media scales (μm , mm , m) for a rock matrix contamination set at 20%.	89
Figure 5.13: Arsenic mass retained to rock matrix (μg) as a function of the pumping rate for different porous media scales (μm , mm , m) where rock matrix contamination is set at 60%.	90
Figure 5.14: Arsenic mass retained (μg) at three spatial scales as a function of pumping rate (180–1,800 L/h), for two initial contamination levels (20% and 60%).	92

Figure 5.15: Long-term effect of dilution on arsenic mass retained at the metre scale under 20% rock-matrix contamination.94

Figure 5.16: Long-term effect of dilution on arsenic mass retained at the μm and mm scale under 20% rock-matrix contamination.95

Figure 5.17: CrunchFlow and MIN3P comparison of scale-dependent arsenic retention versus pumping rate for: a) 20% and b) 60% rock-matrix contamination levels.....97



List of Tables

Table 2.1: Comparative properties of sandstones and carbonates.	15
Table 2.2: Experimental and digitally derived porosity alongside experimental and modelled permeability values for benchmark datasets. Digital porosity is computed from image segmentation, whereas modelled permeability is obtained through pore-scale simulations. Adapted from: Andrä et al. (2013a), Andrä et al. (2013b).....	18
Table 3.1: Comparative overview of arsenic occurrence in selected groundwater systems worldwide.	26
Table 3.2: Speciation of arsenic and its interaction with calcite and Fe/Mn oxides under near neutral to alkaline pH conditions.	31
Table 4.1: Sampling site locations in Cyprus, showing province, projected coordinates (X, Y), and geographic coordinates (latitude and longitude).	40
Table 4.2: Physical dimensions of the cylindrical natural rock cores.	41
Table 4.3: Calibration curve ranges, accuracy, limits of detection (LOD), and limits of quantitation (LOQ) for major oxides and trace elements determined by XRF analysis of the Kantou carbonate samples.	50
Table 4.4: Major oxide composition (mg/kg) (wt.%) of Kantou rock samples determined by X-ray fluorescence (XRF).	51
Table 4.5: Traces composition (mg/kg) of Kantou rock samples determined by X-ray Fluorescence (XRF).	52
Table 4.6: Summary of the key model parameters, boundary conditions, and geochemical processes used in the reactive transport simulations.	63
Table 5.1: Experimentally obtained core porosity and permeability measurements.	71
Table 5.2: The experimental and digital porosities and permeabilities of various sandstone and carbonate rock cores.	72
Table 5.3: The variation in gas volume as a function of the porosity and the sand pack's permeability.	77
Table 5.4: The respective gas volume of natural sandstone core samples at specific porosities.	78
Table 5.5: The variation of porosity and gas volume in relation to grain roundness.	79
Table 5.6: Grid sensitivity analysis of normalized outlet arsenic concentration (C/C_0) for meter-scale simulations.	96

List of Publications

Sharanik, J.; Hadjistassou, C. (2026) Reactive Transport Modelling of Arsenic Retention in Carbonate-Rich Rock Matrices, *Hydrogeology*, (under review).

Sharanik, J., Hadjistassou, C. (2026) Factors Governing the Contamination of Potable Water by Arsenic in Subterranean Reservoirs, *Hydrogeology*, (under review).

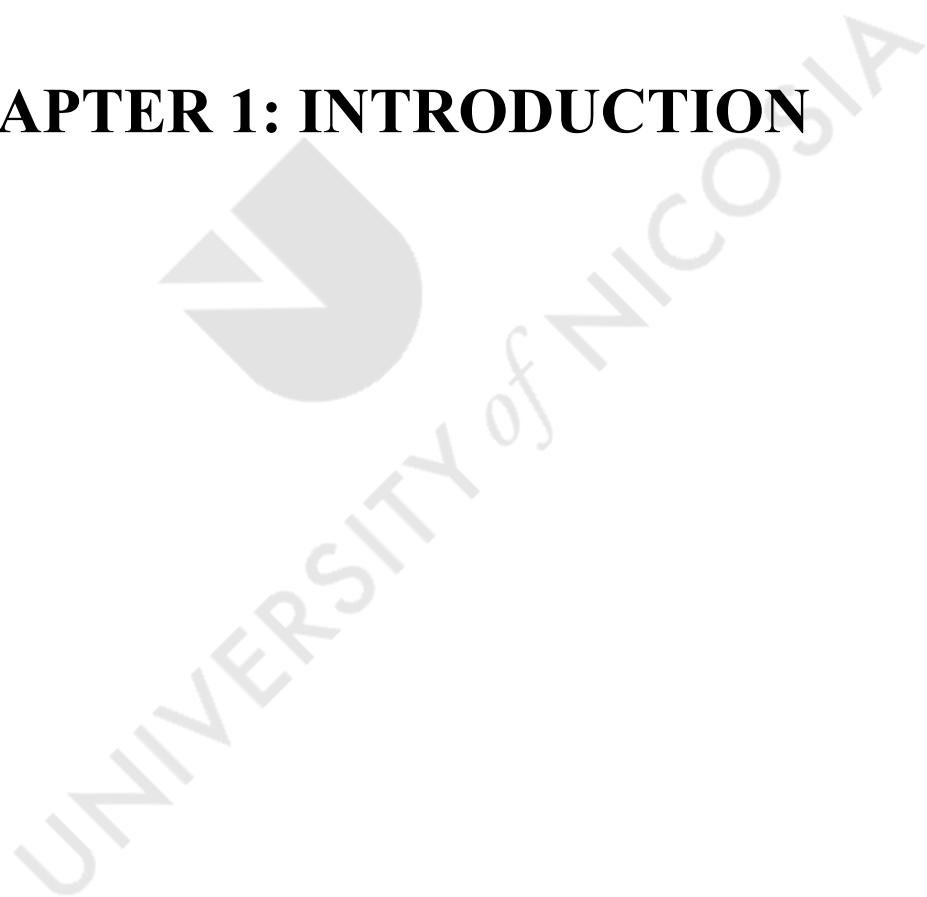
Sharanik, J.; Sarris, E.; Hadjistassou, C. (2025) Storage and Production Aspects of Reservoir Fluids in Sedimentary Core Rocks. *Geosciences* (MDPI), 15, 386, pp. 19, DOI: <https://doi.org/10.3390/geosciences15100386>

Poursanidis, K., Sharanik, J., & Hadjistassou, C. (2024). World's largest natural gas leak from Nord Stream pipeline estimated at 478,000 tonnes. *iScience* (Cell Press), 27(1), 108772, pp. 10; DOI: <https://doi.org/10.1016/j.isci.2023.108772>

Sharanik, J., Duri, M., & Hadjistassou, C. (2023). Liquefied natural gas (LNG). *Encyclopaedia of Toxicology* (4th ed., Vol. 5, pp. 871–892). *Elsevier*, DOI: <https://doi.org/10.1016/B978-0-12-824315-2.00602-3>



CHAPTER 1: INTRODUCTION



1 Introduction

Fluids such as oil, gas, and water are stored and transported within the pore networks of geological formations, where rock properties such as porosity, permeability, and mineral composition control fluid flow and storage. Understanding fluid behaviour in porous media is fundamental to applications ranging from hydrocarbon recovery to groundwater management and contaminant transport (Raats, 1973, Blunt, 2017).

In petroleum systems, hydrocarbons accumulate in porous and permeable sedimentary rocks, where porosity and permeability control fluid storage, flow, and recovery efficiency (Gholami et al., 2012, Sharanik et al., 2025). However, sandstones typically exhibit a strong porosity-permeability correlation, carbonate systems show greater variability due to complex pore geometries and diagenetic processes (Ahr, 2008), with important implications for reservoir performance (Tiab and Donaldson, 2003).

Traditional core analysis provides valuable porosity and permeability data but is destructive in nature for the porous media, time-consuming, and offers limitation in capturing pore-scale heterogeneity. Digital rock physics (DRP) overcomes these limitations by integrating high-resolution imaging with numerical simulations to characterise rock properties non-destructively (Blunt, 2017), enabling three-dimensional visualisation of pore structures and fluid pathways. Furthermore, multiscale imaging approaches combining micro-CT and SEM improve model accuracy and facilitate the evaluation of flow properties in complex carbonate systems (Lee et al., 2024, Wang et al., 2025).

The discovery of major gas fields in the Eastern Mediterranean, including those offshore Cyprus, highlights the importance of understanding carbonate reservoir behaviour, although such systems remain underrepresented in digital studies (Kahveci, 2019). This investigation addresses this gap by adopting an integrated imaging and modelling framework, while also recognising that the underlying principles extend beyond hydrocarbon systems to groundwater environments, where pore structure, permeability, and geochemical interactions govern fluid transport and contaminant behaviour (Raats, 1973).

In carbonate-rich groundwater systems, mineral-fluid interactions strongly control water quality, with Cyprus representing a water-stressed region where reliance on groundwater increases arsenic exposure risk (Smedley and Kinniburgh, 2013). Arsenic mobility in

calcareous environments is governed by complex interactions with calcite, including adsorption, co-precipitation, and redox transformations (Renard et al., 2015, Benedetto et al., 2006). However, most prevailing studies rely on static batch experiments, which partly fail to capture the effects of flow dynamics, pore heterogeneity, and mineral variability that control arsenic transport in natural aquifers.

Recent advances in high-resolution imaging and reactive transport modelling provide a robust framework for linking pore-scale heterogeneity to large-scale transport processes and simulating contaminant behaviour in porous media (Blunt, 2017, Wang et al., 2024, Li et al., 2018, Zhong et al., 2023, Arora et al., 2015). Despite these developments, arsenic behaviour in carbonate-rich systems remains insufficiently understood due to its complex geochemical interactions.

Advanced 3D visualisation and image-analysis tools, including Avizo, Dragonfly, PerGeos, and ImageJ, enable detailed characterisation of pore-scale structures and fluid flow in geological materials, providing a foundation for linking microstructure to macroscopic transport behaviour. When combined with reactive transport modelling, these approaches support the simulation of contaminant migration in groundwater systems without the need for destructive laboratory testing. Reactive transport platforms such as CrunchFlow, alongside PFLOTRAN, TOUGHREACT, COMSOL Multiphysics, and HYTEC, offer robust frameworks for simulating coupled flow and geochemical processes (Steefel et al., 2015, Xie et al., 2015).

Environmental impacts can arise not only from gradual contamination processes but also from accidental events, such as infrastructure failures, which can trigger rapid and large-scale pollutant release. The 2022 Nord Stream pipeline rupture in the Baltic Sea is a prominent example, leading to substantial methane emissions.

In this study, CrunchFlow was used to simulate arsenic transport in a digital carbonate-rich porous medium, building on micro-CT analysis of rock samples from Cyprus. Image data processed in Avizo were used to derive pore-scale properties, and a MATLAB-based algorithm was developed to generate synthetic permeability maps incorporated into the simulations. This framework enabled evaluation of the effects of pore structure, permeability variability, and initial contamination on arsenic mobility, providing a mechanistic basis for improved groundwater quality prediction. In parallel, a transient multiphase flow model was developed to quantify methane release from the 2022 Nord Stream pipeline rupture in the

Baltic Sea, estimating about 478,000 tonnes of emissions (Poursanidis et al., 2024). This complementary work strengthened the modelling framework and underpinned the broader applicability of advanced computational approaches for analysing fluid transport and the climate change impacts across diverse subsurface systems.

1.1 Problem Definition

Understanding how fluids are stored and transported in porous geological media is essential for both energy resource management and groundwater sustainability. However, the relationships between porosity, permeability, and microstructural characteristics in natural rocks remain poorly constrained, particularly in carbonate formations, where heterogeneity, variable mineral composition, and complex pore geometries raise difficulties when predicting fluid behaviour. In contrast, while sandstones often exhibit more regular pore structures, the extent to which their internal architecture governs permeability and flow connectivity under natural conditions is still not fully established. These knowledge gaps hinder the accurate modelling of fluid flow, the storage capacity, and the transport mechanisms in subsurface systems. This motivated the application of DRP and micro-CT imaging on a suite of sandstone and carbonate samples from onshore Cyprus to investigate the variability of petrophysical properties across lithological types and how they can be parameterized for use in numerical models of subsurface flow.

Extending these pore-scale insights to environmental systems, the same controls on fluid behaviour are directly relevant to groundwater processes. These insights are particularly pertinent to groundwater systems in water-stressed regions such as Cyprus, where prolonged droughts, limited recharge, and increasing water demand have led to aquifer overexploitation, declining water tables, and seawater intrusion. In addition to these pressures, arsenic contamination presents a significant environmental and public health risk, with concentrations in some wells exceeding the World Health Organization guideline of 10 $\mu\text{g/L}$. Arsenic mobility is controlled by complex interactions between groundwater and the rock matrix, governed by pH, redox conditions, and mineral composition, which regulate its release, transport, and retention within aquifer systems. Therefore, this research was undertaken to develop a mechanistic understanding of arsenic behaviour in calcareous groundwater systems. Collectively, it integrates digital rock characterisation with reactive transport modelling to assess how pore structure, mineral composition, and hydrological conditions influence contaminant mobility and retention in subsurface environments.

As a separate side investigation, a numerical analysis of the Nord Stream pipeline methane leak was conducted to enhance the research team's capability in multiphase flow simulation and environmental modelling. While distinct from the present study, this work provided valuable experience in coupling fluid flow with environmental transport processes, which informed the computational framework adopted for the reactive transport simulations in this thesis.

1.2 Research Objectives

This research aims to develop a comprehensive, multiscale understanding of fluid-rock interactions in porous media, linking the physical properties of geological formations to the geochemical processes that control contaminant mobility and retention. By integrating digital rock physics (DRP), high-resolution imaging, and reactive transport modelling, the research bridges the gap between reservoir-scale petrophysical characterisation and aquifer-scale groundwater quality assessment. The overarching objective is to establish a mechanistic framework capable of predicting flow, transport, and geochemical reactions across multiple spatial and temporal scales. Specifically, this research aims to:

- Characterise the petrophysical properties of sandstone and carbonate rock samples from onshore Cyprus using micro-CT imaging and Avizo 2019.1, quantifying porosity, permeability, and grain morphology and their influence on fluid storage and flow.
- Develop a DRP-to-simulation digital workflow by creating a MATLAB algorithm that generates permeability maps and converts microstructural data into model-ready parameters.
- Quantify the impact of water flow rate on arsenic mobilisation and retention across the pore-, core-, and metre-scale domains.
- Evaluate how the contamination level (20%, 60%, 100% $\text{Ca}_3(\text{AsO}_4)_2$) affects arsenic release into groundwater and retention under varying pumping conditions.
- Assess scale-dependent processes governing arsenic mobilisation versus retention, focusing on the adsorption, desorption, and precipitation mechanisms.
- Characterise the arsenic-calcite geochemical interactions, including surface complexation and mineral precipitation/dissolution under alkaline conditions.

- Analyse long-term dilution scenarios (500 L/h over 50 years) to determine how sustained pumping influences aqueous arsenic and the stability of solid-phase arsenic.
- Develop a mechanistic framework linking pore-scale retention/release to field-scale groundwater quality predictions.
- Provide groundwater management recommendations, including pumping strategies, dilution practices, and treatment considerations for mitigating arsenic contamination in Cyprus.
- Conduct multiphase flow modelling of the Nord Stream methane leak to quantify amount of released methane and understand transient dynamics as well as apply numerical modelling of reactive transport simulations in the main study.

1.3 Thesis Outline

This thesis is organised into seven sections, each addressing a specific component of the research workflow. The first section, introduces the motivation for the study, outlining Cyprus's acute water scarcity, the emerging concerns surrounding arsenic in groundwater, and the central research objectives. The second part provides a comprehensive literature review covering the fundamentals of porous media, the characteristics of sandstone and carbonate systems, advances in digital rock physics, groundwater stress in Cyprus, arsenic sources and geochemical behaviour, and numerical approaches used to investigate contaminant transport. These themes collectively highlight the knowledge gaps that motivate a multiscale reactive transport investigation. The third section, details the materials and methods employed, including field sampling across Cyprus, XRF and XRD characterisation, micro-CT imaging, thin-section analysis, and the extraction of porosity-permeability relationships. This section also outlines the workflow used to generate permeability maps that feed into numerical simulations. The fourth section describes the modelling tools and simulation framework, presenting the construction of micrometre-, millimetre-, and metre-scale domains, the implementation of CrunchFlow for reactive transport, and a brief overview of the Nord Stream side project that supported the development of additional multiphase-flow modelling expertise. The fifth section, presents the research findings, focusing on the scale-dependent mobilisation and retention of arsenic, the effects of flow rate and the contamination levels, desorption processes, and long-term dilution scenarios. The sixth section synthesizes the key outcomes and contributions of the study, emphasizing their

relevance for groundwater quality management in carbonate-rich aquifers. Finally, the last section, proposes future research directions, including model extensions, improved mineralogical and microbial coupling, 3D simulations, and opportunities for field-scale validation in Cyprus and similar semi-arid environments.



CHAPTER 2:
THEORETICAL BACKGROUND

UNIVERSITY of TUCOSIA

2 Theoretical Background

2.1 Porous Media and Fluid Flow in Geological Systems

Porous media are natural or synthetic materials that contain interconnected void spaces through which fluids can move. In geological formations, these voids, referred to as pores, occur within rocks, sediments, or soils and vary widely in size, shape, and connectivity as shown in Figure 2.1 (Ranjbarzadeh and Sappa, 2025). The ability of a rock or sediment to store and transmit fluids such as water, oil, or gas depends primarily on its porosity and permeability, two of the most fundamental properties governing subsurface flow and transport processes. Porosity represents the fraction of the total volume occupied by void spaces, whereas permeability quantifies the ease with which a fluid can pass through those voids (Raats, 1973). These two parameters are often interrelated but can behave independently depending on the geometry, connectivity, and distribution of the pore network.

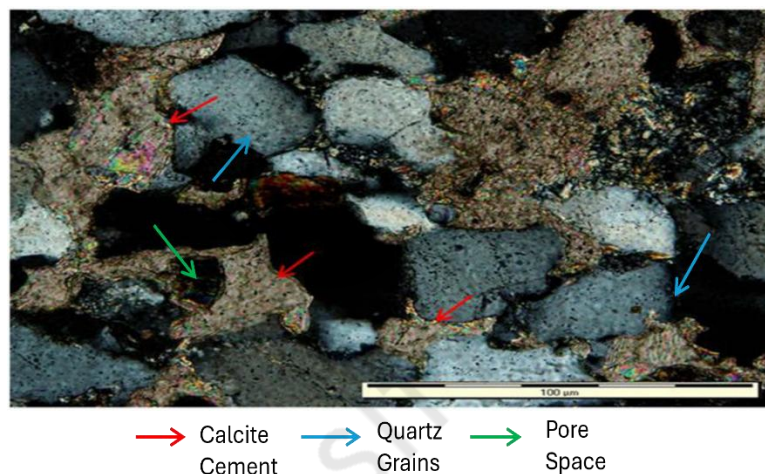


Figure 2.1: Thin-section photomicrograph of a sandstone showing a framework of quartz grains and intergranular pore spaces. Blue arrows indicate detrital quartz grains, red arrows highlight pore-filling cement and partially occluded pore throats, and green arrows mark preserved intergranular porosity. Scale bar = 100 μm. Adapted from: Liang et al. (2020).

Porosity is classified according to the pore origin into primary (intergranular) and secondary (fracture or dissolution-related). Primary porosity develops during sediment deposition and compaction, while secondary porosity morphs the structure later as a result of chemical, mechanical, or tectonic processes such as dissolution, fracturing, or recrystallisation (Tiab and Donaldson, 2003).

Fluid flow in porous media is governed by Darcy's law, which relates the volumetric flow rate to the hydraulic gradient and the intrinsic permeability of the material (Marle, 2006). While Darcy's law is valid for laminar flow regimes typically found in groundwater and hydrocarbon systems, more complex relationships may emerge in cases of multiphase or turbulent flow (Bear and Cheng, 2010). In natural subsurface environments, the movement of fluids is influenced by a combination of advective, diffusive, and dispersive mechanisms, each dependent on the physical and chemical characteristics of the medium. Capillary forces, wettability, and interfacial tension further affect fluid distribution, especially in systems containing multiple immiscible phases such as oil, gas, and water (Morrow and Mason, 2001).

The heterogeneity of porous media introduces significant challenges in predicting and modelling flow behaviour. Variations in grain size, sorting, cementation, and mineral composition can lead to localised differences in permeability, resulting in preferential flow pathways and stagnant zones (Blunt, 2017). These microscale variations influence not only the hydraulic performance of reservoirs and aquifers but also the transport and fate of dissolved substances, including contaminants such as arsenic. As a result, accurate characterisation of pore structure and connectivity is essential for clarifying the movement, storage, and long-term stability of fluids and solutes in the subsurface.

Porous media serve as the foundation for a broad range of environmental and industrial processes, including hydrocarbon recovery, groundwater extraction, contaminant remediation, and carbon dioxide sequestration (Flewelling and Sharma, 2014). In each of these cases, the interaction between fluid dynamics and rock structure determines both the efficiency and the sustainability of the process. For instance, in aquifer systems, the distribution and interconnectivity of pores govern groundwater recharge rates and the mobility of dissolved chemical compounds. Similarly, in hydrocarbon reservoirs, these properties dictate storage capacity, production potential, and sweep efficiency during extraction (Young and Kabala, 2024). Therefore, understanding the fundamental physics of porous media is indispensable for interpreting flow and transport behaviour in both the energy and the water resource contexts.

Recent advances in imaging and computational modelling have enabled the study of porous media at unprecedented resolution. High-resolution micro-CT scanning, combined with digital image analysis and numerical simulations, now allows the visualisation and

quantification of pore networks in three dimensions (Andrä et al., 2013a, Blunt, 2017). These developments have transformed traditional concepts of porosity and permeability from bulk parameters into spatially resolved, structure-dependent descriptors. Such tools provide the basis for linking pore-scale heterogeneity to macroscopic flow behaviour which is an essential step for developing predictive models of groundwater flow, contaminant transport, and reactive geochemical processes in complex geological formations.

In geological settings, the behaviour of porous media is most prominently manifested within sedimentary formations, where variations in grain size, mineralogy, and diagenetic history create a wide spectrum of pore structures and flow characteristics. Among these, sandstones and carbonates are particularly important because they constitute the dominant reservoirs for both groundwater and hydrocarbons. Understanding how their depositional and diagenetic evolution governs porosity, permeability, and fluid transport provides the essential link between the physical principles of the porous media and their natural geological origins.

2.2 Sedimentary Rocks: Sandstones and Carbonates

Sedimentary rocks represent a major component of the Earth's upper crust and serve as the principal host media for subsurface fluids, including hydrocarbons, groundwater, and dissolved solutes. They are formed through the accumulation and lithification of detrital, chemical, or biochemical materials that have been transported and deposited under varying environmental conditions. These depositional and post-depositional processes impart a diverse range of mineralogical, textural, and structural attributes, which ultimately determine the porosity, permeability, and mechanical properties of the resulting rock (Boggs, 2009, Blatt Harvey, 1980). Among the sedimentary rock classes, sandstones and carbonates constitute the most significant lithologies for both hydrocarbon reservoir engineering and groundwater hydrology due to their relatively high fluid storage and transmission capacities (Tiab and Donaldson, 2003).

In the Eastern Mediterranean region, and particularly in Cyprus, sedimentary rocks dominate the geological framework, forming extensive onshore and offshore successions that record complex depositional and tectonic histories. The island's stratigraphy is characterised by widespread carbonate formations, including limestones and dolomites, interbedded with clastic sandstones and marls, which together host the majority of its groundwater resources (Grohmann et al., 2019). These lithologies exhibit pronounced heterogeneity in their pore structure and permeability, reflecting variations in the depositional environment, diagenetic

overprint, and structural deformation associated with the Cyprus Arc and Troodos Ophiolite uplift. As a result, the island provides a natural laboratory for studying fluid storage, flow, and reactive transport in mixed carbonate-clastic aquifer systems, with direct implications for water resource management and contaminant mobility in semi-arid environments.

2.2.1 Sandstones

Sandstones are clastic sedimentary rocks composed primarily of detrital grains of quartz, feldspar, and lithic fragments bound by a variable matrix of clay minerals and cementing agents such as silica, calcite, or iron oxides (Peter A. Scholle et al., 1983). The depositional environment, energy regime, and sediment supply strongly influence grain size, sorting, and packing which are factors that collectively govern the rock's primary intergranular porosity and permeability (Boggs, 2009). Primary porosity in sandstones is established during the deposition stage but is subsequently modified by mechanical compaction and chemical diagenesis. Processes such as quartz overgrowth, clay authigenesis, and carbonate cementation reduce pore volume and pore-throat size, whereas dissolution of unstable minerals or the formation of microfractures may enhance secondary porosity (Worden and Burley, 2009).

The porosity-permeability relationship in sandstones is typically positive and relatively predictable, as increased intergranular connectivity enhances the ease of fluid flow (Nadeau and Ehrenberg, 2006). However, deviations from this trend often occur in rocks exhibiting heterogeneities in grain coatings, cement distribution, or compaction intensity. Quantitatively, sandstone porosity generally ranges between 5% and 30%, while permeability may vary from millidarcies to several darcies, depending on the degree of diagenetic alteration (Tiab and Donaldson, 2003). The relatively homogeneous nature of sandstones and their well-developed pore connectivity make them valuable analogues for evaluating fundamental fluid transport processes in porous media, including the advective and diffusive mechanisms that control contaminants or hydrocarbon migration.

2.2.2 Carbonates

In contrast to sandstones, carbonate rocks, comprising mainly limestones and dolomites, are predominantly formed through chemical and biochemical precipitation in marine environments, often mediated by biological activity (Pan et al., 2025). Their mineralogy is dominated by calcite (CaCO_3) and dolomite ($\text{CaMg}(\text{CO}_3)_2$), and their fabric reflects the

interplay between depositional processes, biological assemblages, and post-depositional diagenetic transformations (Peter A. Scholle et al., 1983). Carbonates are inherently more heterogeneous than clastic rocks due to the wide range of pore types and scales that develop during both sedimentation and diagenesis.

Porosity in carbonate rocks is commonly classified as interparticle, intraparticle, moldic, vuggy, channel, and fracture porosity, each of which arises from distinct geological processes (Choquette and Pray, 1970). Interparticle and intraparticle pores represent primary depositional features, whereas moldic and vuggy porosity typically form through selective dissolution of unstable grains or fossils. Fracture porosity may result from tectonic stress or karstification, creating secondary conduits for fluid migration (Lucia, 2007). These diverse pore types collectively produce a complex and anisotropic permeability field that defies simple scaling relationships. As a result, the correlation between porosity and permeability in carbonate rocks is weak or scattered, in contrast to the more consistent relationship observed in sandstones (Nadeau and Ehrenberg, 2006).

Diagenetic processes, including dolomitization, cementation, and recrystallization, exert dominant control on carbonate pore evolution. Dolomitization, for example, may either enhance or occlude porosity depending on the replacement geometry and fluid chemistry involved. Cementation can significantly reduce both porosity and permeability, while dissolution during meteoric or burial diagenesis may create high-permeability pathways (Dar et al., 2022, Salah et al., 2023, Yang et al., 2020). These dynamic and competing processes produce multimodal pore systems spanning several orders of magnitude, from nanoscale pores associated with matrix microporosity to centimetre-scale vugs and fractures (Khan and Mandal, 2022). Consequently, flow within carbonate systems is often governed by dual- or triple-porosity behaviour, where matrix storage coexists with fracture dominated permeability networks.

2.2.3 Petrophysical and Hydraulic Characteristics of Sandstones and Carbonates

The contrasting petrophysical architectures of sandstones and carbonates produce fundamentally different hydraulic responses. As shown in Table 2.1, sandstones typically exhibit uniform pore networks with relatively predictable permeability-porosity trends, facilitating the application of continuum-based models for flow and transport (Tiab and Donaldson, 2003). In contrast, carbonates display highly heterogeneous pore distributions, where localised features such as fractures, dissolution channels, and vugs dominate fluid

migration (Lucia, 2007). These characteristics give rise to non-linear flow regimes, preferential flow pathways, and spatially variable retention zones that complicate the prediction of contaminant or solute transport.

From a hydrogeological perspective, both lithologies serve as important aquifer systems in regions such as Cyprus. Sandstone aquifers tend to exhibit higher predictability in flow behaviour due to their more uniform pore geometry, while carbonate aquifers are often characterised by heterogeneous flow fields and anisotropic permeability emanating from fracture and dissolution networks. These contrasts have direct implications for groundwater storage, extraction efficiency, and contaminant dispersion, particularly for reactive species such as arsenic that interact with carbonate minerals during transport (Zhou et al., 2024, Chou et al., 2025).



Table 2.1: Comparative properties of sandstones and carbonates.

Property	Sandstone	Carbonate
Composition	Quartz, feldspar, lithic fragments (Schicker et al., 2021)	Calcite, dolomite, aragonite (Zhang et al., 2022)
Depositional environment	Fluvial, deltaic, aeolian, shallow marine (Schicker et al., 2021)	Marine platforms, reefs, lagoons (Blunt, 2017)
Porosity (%)	5–35 (Zanganeh Kamali et al., 2022)	0.5–30 (Zhang et al., 2022)
Permeability (mD)	10^{-1} – 10^4 (Schicker et al., 2021)	10^{-3} – 10^4 (Zanganeh Kamali et al., 2022)
Dominant pore types	Intergranular (Schicker et al., 2021)	Intergranular, vuggy, moldic, fractures (Zhang et al., 2022)
Pore throat geometry	Relatively uniform (Blunt, 2017)	Highly variable (Zhang et al., 2022)
Heterogeneity	Low–moderate (Schicker et al., 2021)	High (matrix + fractures + vugs) (Zhang et al., 2022)
Flow behavior	Predictable, uniform (Blunt, 2017)	Complex, dual-porosity, preferential flow (Blunt, 2017)
Examples	Berea, Fontainebleau	Edwards, Arab-D

The integration of micro-computed tomography (micro-CT), digital rock physics (DRP), and numerical simulation techniques presently enables detailed quantitative assessment of these lithologies. Such approaches provide three-dimensional reconstructions of pore geometries and permit direct computation of petrophysical parameters including porosity, permeability, tortuosity, and specific surface area (Blunt, 2017). Such digital datasets bridge the gap between microscale rock structure and macroscale hydraulic behaviour, facilitating more accurate simulations of flow, transport, and reactive geochemical processes in both sandstone and carbonate systems.

2.3 Image-Based Characterisation of Porous Media: The Role of DRP

The characterization of porous media has traditionally relied on laboratory core analysis, including techniques such as gas porosimetry, mercury intrusion capillary pressure, and steady-state or pulse-decay permeability tests. While these approaches have long provided reliable estimates of bulk petrophysical parameters, they are inherently destructive, time-intensive, and spatially limited, often failing to capture the heterogeneity and multiscale nature of pore systems (Arns et al., 2004, Andrä et al., 2013a, Mehmani et al., 2020). The development of Digital Rock Physics (DRP) has revolutionised the study of porous materials by providing a non-catastrophic, image-based alternative that allows the visualisation, quantification, and simulation of physical processes directly from digitised three-dimensional rock volumes (Mehmani et al., 2020).

2.3.1 Fundamentals of Digital Rock Physics

Digital Rock Physics integrates high-resolution imaging, image segmentation, and numerical modelling to extract and simulate physical properties from digital representations of rock samples (Blunt, 2017). As shown in Figure 2.2, the workflow typically involves three main stages: 1) sample imaging using techniques such as X-ray micro-computed tomography (micro-CT), focused ion beam-scanning electron microscopy (FIB-SEM), or synchrotron-based tomography; 2) digital reconstruction and segmentation of the pore and solid phases; and 3) computation of physical properties, such as porosity, permeability, tortuosity, specific surface area, and elastic moduli, through numerical simulations or direct image analysis (Arns et al., 2004).

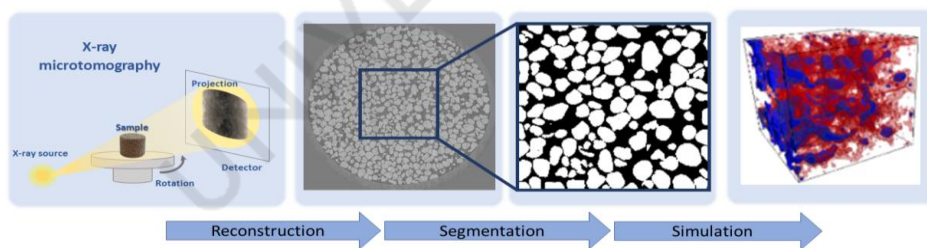


Figure 2.2: A typical digital rock workflow. Adapted from: Varfolomeev et al. (2019).

This approach enables the quantitative characterisation of the three-dimensional pore structure at the micrometre to the nanometre resolution, thereby capturing the intricate geometry of intergranular pores, throats, and microfractures that govern fluid transport in

natural rocks. Compared to traditional core methods, DRP offers substantial advantages in preserving rare or delicate samples, enabling repeatable virtual experiments, and establishing a direct link between the microstructure and macroscopic behaviour (Arns et al., 2005).

2.3.2 Imaging and Visualisation Techniques

Among the various imaging modalities, micro-CT has emerged as the most popular technique in rock physics due to its ability to provide volumetric datasets with isotropic voxel sizes ranging from the submicron to several microns (Cnudde and Boone, 2013). The reconstructed grey-scale images represent variations in X-ray attenuation, which correspond to differences in mineral density and pore space. Advanced image processing software such as Avizo, Dragonfly, PerGeos, and ImageJ/Fiji are used for segmentation, morphological analysis, and quantitative pore-network extraction (Latham et al., 2008).

The segmentation stage is particularly critical, as it determines the boundary between the solid and the pore phases. Thresholding, machine-learning algorithms, and morphological filtering are often combined to achieve accurate classification (Schlüter et al., 2014). Once segmented, the 3D pore network can be visualised and analysed to determine geometrical parameters such as pore size distribution, coordination number, and throat radius, which directly influence fluid flow, permeability, and tortuosity.

In this research, micro-CT scans of eleven sandstone and carbonate samples collected from onshore Cyprus were processed using Avizo 2019.1, enabling a detailed quantification of porosity, permeability, and grain morphology. These digital measurements formed the foundation for developing a MATLAB-based computational tool capable of generating synthetic permeability maps for various lithological types. Such synthetic models are instrumental in linking microstructural attributes to macroscopic transport behaviour, serving as the input framework for subsequent COMSOL Multiphysics simulations.

2.3.3 Advantages and Limitations

The transition from traditional experimental methods to digital approaches represents a paradigm shift in geoscientific research. However, limitations remain, including resolution constraints, segmentation uncertainties, and representative elementary volume (REV) selection, which can affect the extrapolation of microscale results to core or field scales (Andrä et al., 2013a, Blunt, 2017).

Beyond its traditional applications in reservoir engineering, the principles of digital rock physics also provide a quantitative foundation for deriving relationships between pore-scale structure and bulk petrophysical properties. Such relationships enable the generation of synthetic permeability maps that could serve as boundary conditions or property distributions in numerical transport models.

Andrä et al. (2013a), Andrä et al. (2013b) provided a benchmark application of Digital Rock Physics by reconstructing pore-scale geometries from micro-CT images of sandstones and the simulation of their petrophysical properties. The results demonstrated that the model’s permeability predictions deviated by only 10–15% from experimental results, while porosity was calculated at 20–25%. This close alignment proves the model accurately replicates real-world pore connectivity. As summarised in Table 2.2, the comparison between experimental and digital porosity displays minimal deviation for sandstone samples, whereas permeability predictions exhibit greater variability, particularly in carbonate rocks, reflecting the influence of heterogeneity and numerical modelling approaches on flow properties.

Table 2.2: Experimental and digitally derived porosity alongside experimental and modelled permeability values for benchmark datasets. Digital porosity is computed from image segmentation, whereas modelled permeability is obtained through pore-scale simulations. Adapted from: Andrä et al. (2013a), Andrä et al. (2013b).

Rock Type	Dataset	Experimental Porosity (%)	Digital Porosity (%)	SD (%)	Experimental Permeability (mD)	Model Permeability (mD)
Sandstone	Fontainebleau	15.2	14.7	0.35	15–20.1mD	15.3 – 19.14
Sandstone	Berea	20	20.9	0.64	~100–200	113 – 124
Carbonate	Grosmont	21	27.1	4.31	Not mentioned	353 – 1706
Synthetic	Sphere pack	34.3	34.3	0.00	Not mentioned	221,587 – 270,220

Within the scope of the present study, this approach is applied to carbonate-rich sandstones from onshore Cyprus, where the porosity-permeability relationship derived from digital analysis supports the simulation of arsenic reactive transport discussed in the following sections.

CHAPTER 3: LITERATURE REVIEW



3 Literature Review

This section will provide the theoretical background underpinning the study, including the fundamental principles of fluid flow in porous media, the characteristics of sedimentary rocks with emphasis on sandstones and carbonates, and the role of image-based characterisation techniques such as digital rock physics (DRP) in analysing pore structure and transport properties.

3.1 Water Scarcity and Groundwater Use in Cyprus

Cyprus is among the most water-stressed countries in the European Union. In 2022, Cyprus' Water Exploitation Index Plus (WEI+) reached 71%, well above the severe water scarcity threshold of 40%, indicating unsustainable use of its limited freshwater resources (Ellinas, 2025). The country's long-term average freshwater availability is approximately 400m³ per person per year, the second lowest in Europe after Malta, while EU households typically access around 4,000m³ per person per year (European Union, 2020). This scarcity stems from a semi-arid climate, chronic droughts, and declining precipitation. Over the past 90 years, annual rainfall has dropped by 15%, and by September 2025, reservoir levels had fallen to just 14.7% of their capacity (Michele Kambas and Kourtoglou, 2025). Demand has intensified dramatically, water usage has tripled since 1990 due to population growth and tourism, resulting in a 2023 water deficit of approximately 66 million cubic meters (Michele Kambas and Kourtoglou, 2025). Agriculture remains the dominant water user, accounting for nearly 59% of total demand, followed by domestic use (~29%) and tourism (~5%) (Suwanu, .2021). Groundwater remains the backbone of Cyprus's water supply, especially in rural areas and during dry seasons. However, decades of overexploitation have led to declining water tables, seawater intrusion in coastal aquifers, and deteriorating aquifer health (Aeoliki Ltd, 2009, Suwanu, .2021). Additionally, the island is increasingly turning to desalination to address shortages, with desalinated water now supplying around 70% of drinking water (Michele Kambas and Kourtoglou, 2025).

Cyprus's desalination capacity has steadily expanded since the 1990s, with four permanent plants now producing over 220,000 m³/day, supplemented by mobile reverse-osmosis units that can add ~15,000 m³/day during drought emergencies (Zachariadis, 2010, Hadjigeorgiou, 2022). While desalination secures municipal and tourism supplies, it is accompanied with the challenge of high energy consumption (Elimelech and Phillip, 2011),

dependence on imported fuel (Zachariadis, 2010), and brine disposal impacts on coastal ecosystems (Missimer and Maliva, 2018). This highlights the importance of coupling desalination with demand management and water reuse strategies (Angelakis and Gikas, 2014).

Beyond quantity concerns, groundwater quality issues are emerging. Monitoring under the EU Water Framework Directive shows that while heavy metal concentrations, including arsenic, often remain below regulatory limits, episodic alarms have prompted closer attention (Nikolaou et al., 2020). Notably, a survey of 84 boreholes found arsenic levels ranging from 0.3 to

In a broader Mediterranean context, Cyprus's situation resembles that of Malta, where chronic structural water deficits have long necessitated reliance on desalination and efforts to reduce losses from the municipal distribution network (Xevgenos et al., 2021), and Crete, where spatially uneven rainfall drives recurrent local imbalances (Tzanakakis et al., 2020). Comparative studies suggest that while desalination provides security, sustainable water management also requires managed aquifer recharge (Dillon et al., 2019), reduction of water distribution network losses (European Environment Agency (EEA), 2018) and integration of reclaimed wastewater (Angelakis and Gikas, 2014). These strategies are increasingly recognised under EU directives as critical complements to supply-side solutions (European Union, 2020).

This dual challenge, namely, the water scarcity in both quantity and quality, highlights the urgent need for better understanding of groundwater dynamics in Cyprus. In particular, this research must address how hydrological stress, aquifer mineralogy, and geochemical processes interact to influence the mobilisation and retention of inorganic chemical contaminants, such as, arsenic.

3.2 Arsenic in Groundwater: Sources and Risks

Arsenic is a naturally occurring element in the Earth's crust and can infiltrate groundwater through the weathering of minerals and ores, as well as through geogenic processes such as the reductive dissolution of iron oxides (Chung et al., 2014). In this process, arsenic that is initially adsorbed onto or co-precipitated with iron oxide minerals is mobilised into the aqueous phase when reducing conditions lead to the dissolution of these host phases (Cai et al., 2022). Globally, arsenic contamination of groundwater is a critical issue because of its toxicity even at low concentrations and widespread geological occurrence (Shankar et al., 2014). The World Health Organization (WHO) has established a guideline threshold of 10 µg/L for arsenic in drinking water to mitigate its serious health impacts, including skin, bladder, and lung cancers, as well as neurological and cardiovascular diseases. Arsenic exists predominantly as the inorganic species arsenite (As(III)) and arsenate (As(V)) in groundwater, with speciation controlled by redox conditions and pH levels (Shankar et al., 2014).

In Cyprus, arsenic concentrations in groundwater are generally moderate, but violations of the WHO guideline have been recorded in certain aquifers, especially in rural agricultural zones (Christodoulidou et al., 2012). Later field assessments confirmed sporadic elevated values, with arsenate identified as the predominant species. The widespread severe arsenic pollution is not pervasive, but these episodic exceedances highlight the need for careful monitoring. The occurrence of arsenic in Cyprus groundwater is primarily geogenic, influenced by aquifer mineralogy, including carbonate content and iron oxides, which control arsenic sorption and release (Christodoulidou et al., 2012). However, anthropogenic pressures such as excessive groundwater abstraction, reduced natural recharge, and saline intrusion further alter aquifer geochemistry and can enhance arsenic mobilisation. These stresses disturb the redox balance, promote desorption processes, and may accelerate the transfer of arsenic from the solid matrix into the aqueous phase (Christodoulidou et al., 2012, Chung et al., 2014).

Although the sources and health risks of arsenic in Cyprus have been characterised in several localised studies, the broader policy and monitoring framework remains limited. The following subsection outlines the current environmental regulations and analytical practices related to arsenic testing and groundwater quality management.

3.2.1 Environmental Policy Framework and Arsenic Monitoring in Cyprus

The management of groundwater quality in Cyprus operates under the overarching European Union Water Framework Directive (WFD; 2000/60/EC), which provides a legally binding framework for the protection and sustainable use of water resources. This directive requires all EU Member States to classify groundwater bodies, monitor their status, and achieve “good quantitative and chemical conditions.” Complementary directives, namely, the Groundwater Directive (2006/118/EC) and the Drinking Water Directive (98/83/EC), recently updated as Directive (EU) 2020/2184, define the chemical standards for contaminants, including trace metals and metalloids. The World Health Organization (WHO, 2017) and the EU Drinking Water Directive both set a parametric value of 10 µg/L for arsenic in drinking water. However, while this limit is adopted in Cypriot legislation, arsenic is not routinely included in national monitoring programs unless its presence is suspected or confirmed through site-specific investigations.

The Cyprus Water Development Department (WDD) and Cyprus Geological Survey Department (GSD) are responsible for implementing groundwater monitoring and reporting under the WFD. Standard analyses typically target parameters such as chloride, nitrate, sulfate, total hardness, conductivity, pH, and major cations (Ca^{2+} , Mg^{2+} , Na^+ , K^+), with trace metals like iron, manganese, and zinc tested selectively. Arsenic, cadmium, and mercury are analysed only in targeted sampling campaigns—usually when linked to potential contamination sources such as agricultural return flows, mine drainage, or geothermal discharge zones (Shahid et al., 2018). Reports by the Water Development (2021) and the European Environment Agency (EEA) (2018) note that arsenic is absent from the majority of regular groundwater testing datasets in Cyprus due to historically low concentrations and the lack of industrial inputs. This monitoring gap poses a potential risk given the natural geochemical variability of Cyprus’s carbonate-rich aquifers, where localised exceedances have been documented (Christodoulidou et al., 2012, Golfopoulos et al., 2021, Konstantinou et al., 2014).

When tested, arsenic determinations typically follow ISO 11885 (ICP-OES) or ISO 17294-2 (ICP-MS) protocols for trace element quantification, achieving detection limits below 0.1 µg/L. Sampling procedures conform to ISO 5667-11:2009, requiring filtration through 0.45µm membranes and acidification to $\text{pH} < 2$ with ultrapure nitric acid. Analytical quality assurance is maintained through inter-laboratory calibration under the European

Reference Laboratory for Water Quality (ERAWAT). Despite the technical capacity of national laboratories, arsenic testing remains sporadic and largely research-driven rather than part of systematic surveillance. Consequently, long-term datasets suitable for trend analysis are scarce, and site-specific assessments provide valuable complementary insights into potential geochemical risks.

The absence of arsenic in standard monitoring programs underscores the importance of geochemically informed modelling as an approach to predict and interpret possible mobilisation events. By integrating mineralogical, hydrological, and redox controls, numerical simulations such as those implemented in this thesis can identify conditions likely to trigger arsenic release and help inform the design of targeted monitoring strategies. This approach aligns with the adaptive management principles of the Water Framework Directive and strengthens the scientific basis for early detection and prevention of groundwater contamination.

3.3 Global Overview of Arsenic in Groundwater

Arsenic contamination of groundwater is a global problem, with significant regional variability in both concentrations and health impacts (Podgorski and Berg, 2020). Major arsenic hotspots include the alluvial and deltaic aquifers of South and Southeast Asia, the Andean regions of South America, parts of the western United States, and arid to semi-arid regions of the Mediterranean (P. Ravenscroft et al., 2009, Smedley and Kinniburgh, 2013). In Bangladesh and West Bengal (India), where millions rely on shallow tubewells for drinking water, concentrations frequently exceed 50–100 $\mu\text{g/L}$, exposing more than 40 million people to levels above the WHO guideline of 10 $\mu\text{g/L}$ (Ahmed et al., 2004). Vietnam and Cambodia report similarly elevated levels in the Mekong delta aquifers, linked to reductive dissolution of Fe oxyhydroxides. In Latin America, northern Chile and Argentina's Chaco-Pampean plain show chronic exceedances, often associated with volcanic glass weathering and hydrothermal inputs (Bundschuh et al., 2012). In the United States (U.S.), arsenic contamination has been documented in aquifers across Nevada, Arizona, and California primarily linked to geothermal systems and volcanic lithologies (Welch, 2000). Figure 3.1 demonstrates the global distribution of arsenic in groundwater, highlighting regions where concentrations frequently exceed the WHO guideline value of 10 $\mu\text{g/L}$. The map illustrates that the most severely affected areas include South and Southeast Asia, parts of South America, and specific regions of the United States, while moderate hotspots are also present in Europe and

the Mediterranean. This global perspective ranks Cyprus within a broader spectrum of arsenic-contaminated aquifer systems.

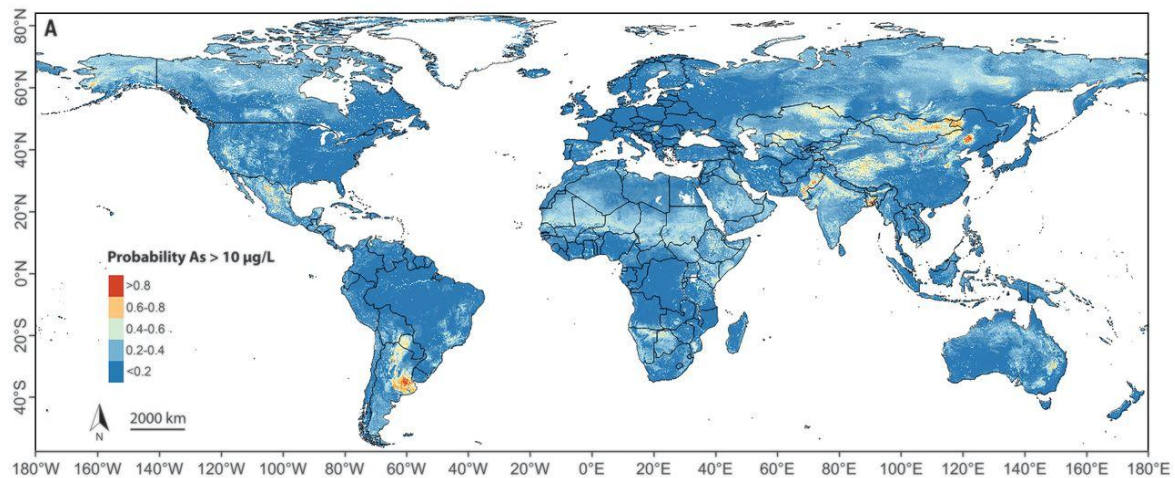


Figure 3.1: Global prediction of the distribution of arsenic in groundwater. Adapted from: Podgorski and Berg (2020).

Importantly, the geochemical settings differ in Asia's large alluvial basins, reductive dissolution of Fe(III) minerals releases As(III), whereas in carbonate-rich terrains such as parts of Spain, Italy, and Cyprus, arsenic occurs mainly as As(V), mobilised under alkaline, oxic conditions through desorption from calcite and co-precipitation processes (Matschullat, 2000, Smedley and Kinniburgh, 2002). This contrast highlights why carbonate aquifers present distinct risks, with arsenic behaviour governed predominantly by pH buffering and carbonate saturation rather than by redox-driven dissolution.

Table 3.1 demonstrates arsenic concentrations in major groundwater settings by concentration, speciation, and the mobilisation mechanism. Fe-rich alluvial/deltaic aquifers in South Asia (Bangladesh, West Bengal, Mekong) are the most severe, often displaying concentrations in excess of 100 µg/L, driven by reductive dissolution releasing As(III). Volcanic terrains (northern Chile, Chaco-Pampean Argentina) can surpass 1,000 µg/L, with As(V) sourced from volcanic glass weathering/hydrothermal inputs under oxic conditions. The western USA shows mixed As(III)/As(V) linked to geothermal/volcanic systems, sometimes >300 µg/L. Carbonate aquifers in Europe (Spain, Cyprus) are typically lower—~10–200 µg/L in Spain and up to 41 µg/L in Cyprus—where As(V) is mobilised mainly by desorption from calcite and competition with phosphate/bicarbonate. Framed globally, Cyprus is not extreme but still exceeds WHO limits, making it a key Mediterranean analogue for arsenic behaviour in semi-arid, groundwater-dependent regions.

Table 3.1: Comparative overview of arsenic occurrence in selected groundwater systems worldwide.

Region/Setting	Typical Concentrations ($\mu\text{g/L}$)	Dominant Speciation	Main Mobilisation Mechanism	References
Bangladesh, West Bengal (India) – large alluvial/ deltaic aquifers	10–500 (often >100)	As(III) dominant	Reductive dissolution of Fe(III) oxyhydroxides under anoxic conditions	P. Ravenscroft et al. (2009), Ahmed et al. (2004)
Vietnam, Cambodia- Mekong Delta	10–300	As(III) dominant	Similar to Bengal Basin: Fe-oxide reduction releases adsorbed Arsenic	Smedley and Kinniburgh (2002), Berg et al. (2007).
Chile (Atacama, Antofagasta) & Argentina (Chaco-Pampean Plain)	50–1000 (sometimes >2000)	As(V) dominant	Volcanic glass weathering, hydrothermal inputs, evaporation concentration	Bundschuh et al. (2012), Nicolli et al. (1989).
Western USA (Nevada, California, Arizona)	10–300	Mixed As(III)/As(V)	Geothermal fluids, volcanic lithologies, evaporite dissolution	Welch (2000), Degnan et al. (2020)
Spain (La Mancha aquifer, Madrid Basin)	10–200	As(V) dominant	Carbonate-buffered systems: desorption from calcite and exchange with phosphate/bicarbonate	Smedley and Kinniburgh (2002), López-Pamo et al. (1999).

Region/Setting	Typical Concentrations ($\mu\text{g/L}$)	Dominant Speciation	Main Mobilisation Mechanism	References
Cyprus (various boreholes)	<0.3–41	As(V) dominant	Alkaline carbonate aquifers: desorption, limited co-precipitation with calcite	Christodoulidou et al. (2012)

Consequently, Cyprus serves as a representative carbonate case where management should target geochemical controls (pH, competing anions) and pumping regimes—linking directly to the mechanistic analysis in the next section.

3.4 Geochemical Mechanisms of Arsenic Speciation and Transport

The geochemical behaviour of arsenic in aquifer systems is governed by complex interactions among aqueous speciation, mineralogical composition, and hydrogeochemical conditions.

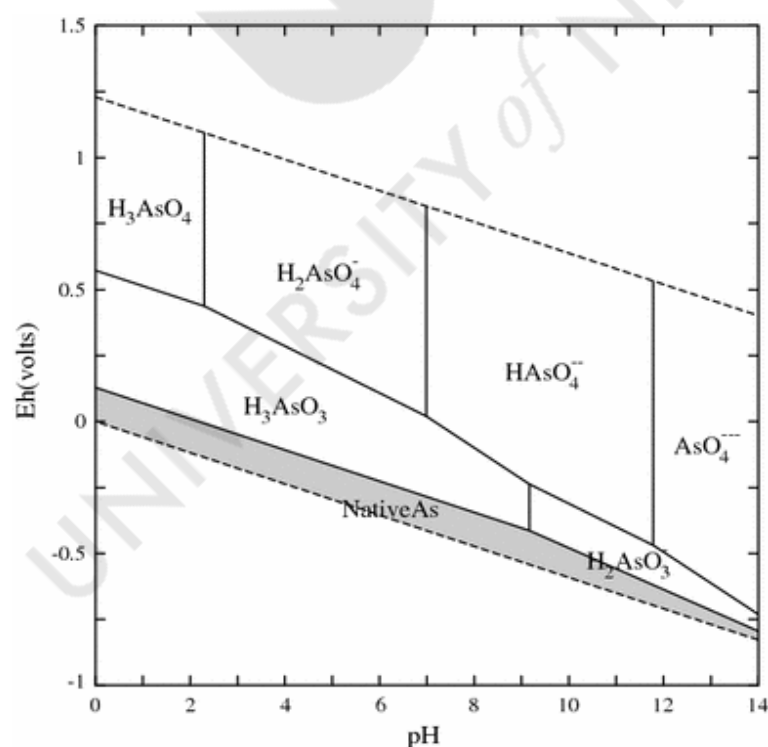


Figure 3.2: Eh–pH diagram for the system As–O–H, at 25°C, and 1 bar. Arsenic concentration is set at 10^{-6} M. The gray shaded area denotes the solid phase. Adapted from: Lu and Zhu (2011).

Arsenic occurs predominantly in two inorganic oxidation states: arsenite (As(III)) and arsenate (As(V)). The relative abundance of these species is dictated primarily by the redox potential (Eh) and the hydrogen ion activity (pH) of the groundwater system.

Figure 3.2 demonstrates that arsenite species (e.g., H_3AsO_3) are stable under reducing conditions at neutral pH, whereas arsenate species (e.g., H_2AsO_4^- , HAsO_4^{2-}) dominate under oxidising conditions. These transitions are particularly relevant to aquifers where pumping, organic matter degradation, or mixing with seawater can shift Eh and pH, altering arsenic speciation and mobility. This distinction is of a critical importance, as As(III) is more toxic and exhibits lower sorption affinity for mineral surfaces relative to As(V), thereby, conferring higher mobility in aquifers (Smedley and Kinniburgh, 2002).

The partitioning of arsenic between the solid and the aqueous phases is strongly influenced by sorption-desorption reactions on mineral substrates. Ferric oxyhydroxides, manganese oxides, aluminosilicates, and clay minerals constitute the principal sorbents in many aquifers. However, the competitive presence of other oxyanions, particularly phosphate, silicate, and bicarbonate, can reduce sorption capacity and facilitate the release of arsenic into solution (Parkinson, 2016). The geochemical context of agricultural regions, where phosphate inputs are elevated, may therefore exacerbate arsenic mobilisation.

Another critical mobilisation mechanism is the reductive dissolution of Fe (III)-bearing phases. Under anoxic conditions, microbial reduction of Fe (III) to Fe (II) results in the dissolution of Fe-oxyhydroxides and the concomitant release of sorbed arsenic into the aqueous phase. This process has been identified as the principal mechanism responsible for extensive arsenic contamination in the Bengal Basin aquifers (Islam et al., 2013). In contrast, under oxic to mild alkaline conditions, arsenic may be released via desorption processes, as the increasing activity of hydroxyl ions reduces surface complexation, leading to greater mobility. Thus, pH exerts a first-order control on arsenic sorption, with maximum sorption typically observed at circumneutral values and decreasing retention under alkaline conditions.

Figure 3.3 expands the Eh-pH framework by including Fe and sulfur phases. Under oxidising conditions, scorodite ($\text{FeAsO}_4 \cdot 2\text{H}_2\text{O}$) becomes a stable phase, effectively removing As(V) from solution. Conversely, under reducing conditions, Fe (III) oxyhydroxides dissolve, liberating sorbed arsenic and stabilising As (III) in solution. This dual role of iron minerals such as sinks in oxic environments and sources under anoxic conditions, is central to arsenic cycling in aquifers. For carbonate-rich aquifers such as those found in Cyprus, where Fe

concentrations are lower than in Fe-rich alluvial basins, these processes are less dominant but still influence local arsenic retention and release, especially in zones where iron oxides spatially associated with carbonate minerals.

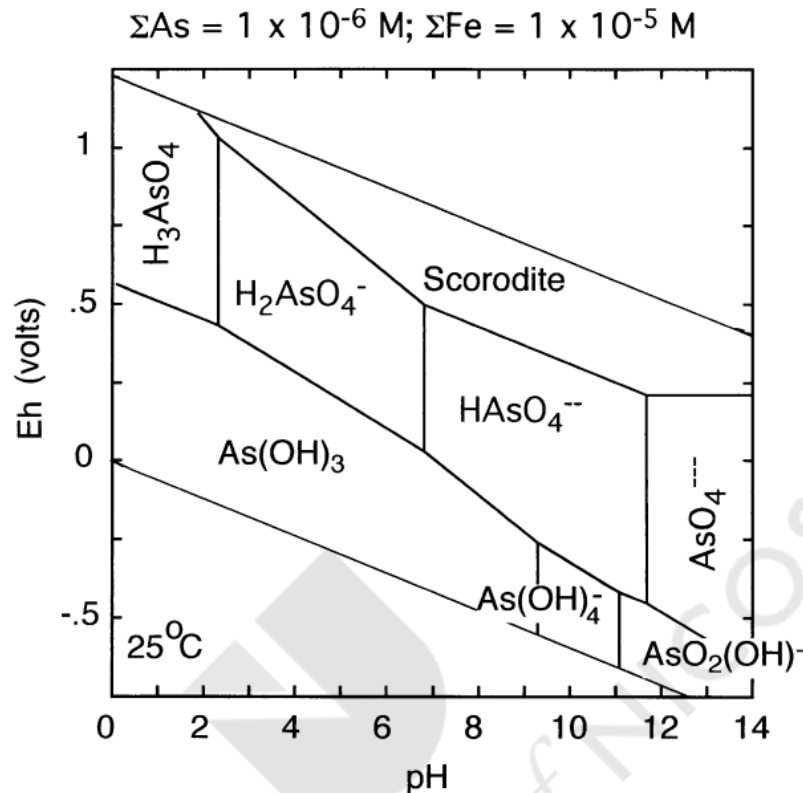


Figure 3.3: Eh-pH diagrams for the system As-O-H-Fe, at 25°C, and 1 bar. Adapted from: Randall et al. (2001).

Precipitation and co-precipitation phenomena also regulate arsenic mobility. Arsenic may form sparingly soluble phases, such as arsenic sulfides under sulfidic conditions, or may be structurally incorporated into carbonates and iron-bearing minerals. Although, these processes can attenuate arsenic concentrations in solution, they are not necessarily permanent sinks, as subsequent shifts in pH-Eh conditions may destabilise the solid phases and reintroduce arsenic into groundwater (P. Ravenscroft et al., 2009).

The mineralogical composition of the host aquifer further modulates arsenic geochemistry. In silicate-dominated aquifers, the retention of arsenic is largely controlled by Fe- and Mn-oxide phases, whereas in carbonate-rich systems, arsenic can be immobilised through surface complexation on calcite or through the precipitation of calcium arsenate phases. In addition, natural organic matter plays a dual role, both by providing sorption sites

and by serving as an electron donor for microbial processes that mediate redox-driven arsenic transformations (Oremland and Stolz, 2003).

In summary, arsenic geochemistry in aquifers reflects a dynamic equilibrium between immobilisation and mobilisation pathways that are highly sensitive to environmental perturbations. These processes operate within narrow geochemical windows where small shifts in redox conditions, pH, or competitive ion concentrations can strongly influence arsenic retention or release. Given the anthropogenic pressures on groundwater systems, including over-abstraction, reduced recharge, and saltwater intrusion, understanding these mechanisms is essential for predicting the long-term fate of arsenic in aquifers and for developing strategies to safeguard water quality.

3.4.1 Arsenic-Calcite Interactions

Arsenic occurs in both inorganic and organic forms, but inorganic species such as As (III) and As (V) are dominant in groundwater (World Health Organization (WHO), Shankar et al., 2014). Arsenic actively reacts with calcite through both surface complexation (adsorption and desorption) and mineral precipitation/dissolution processes, which play a crucial role in controlling its mobility in groundwater systems (Roman Ross et al., 2008, Sørensen et al., 2008). The interaction between arsenic and calcite is strongly controlled by pH, with secondary influences from temperature, pressure, and aquifer composition, particularly in systems dominated by calcite and lacking iron or aluminium oxides (Renard et al., 2015, Bhattacharya et al., 2007). Table 3.2 summarises the relevant arsenic species, their interactions with calcite, and how pH affects these processes. In this study, the groundwater pH was assumed to be around 8, arsenite (As (III)) exists mainly as H_3AsO_3 and, to a lesser extent, H_2AsO_3^- , while arsenate (As(V)) is present predominantly as H_2AsO_4^- and HAsO_4^{2-} , reflecting well-established speciation trends at this pH (Smedley and Kinniburgh, 2013, Sørensen et al., 2008).

Table 3.2: Speciation of arsenic and its interaction with calcite and Fe/Mn oxides under near neutral to alkaline pH conditions.

Arsenic Form	Aqueous Species (pH 7–10)	Interaction with Calcite	Interaction with Fe/Mn Oxides	References
As(III)	H ₃ AsO ₃ (neutral, dominant ≤ pH ~9.2); H ₂ AsO ₃ ⁻ (appears ≥ pH 9.2).	H ₃ AsO ₃ shows weak adsorption; after deprotonation (H ₂ AsO ₃ ⁻), adsorption increases.	Weak adsorption: more mobile, adsorption limited compared to As(V).	Smedley and Kinniburgh (2013), Sørensen et al. (2008).
As(V)	H ₂ AsO ₄ ⁻ (dominant ≤ pH ~9); HAsO ₄ ²⁻ (dominant ≥ pH 9–10).	H ₂ AsO ₄ ⁻ is strongly adsorbed; HAsO ₄ ²⁻ both adsorbs and co-precipitates.	Strong adsorption onto Fe/Mn oxides, can be released under reductive dissolution.	

3.5 Numerical and Computational Approaches to Arsenic Mobility

Experimental studies of arsenic in groundwater have long relied on batch adsorption tests, column flow-through experiments, and core-scale laboratory measurements to determine sorption capacity, transport dynamics, and breakthrough behaviour under controlled chemical conditions. These methods have clarified the influence of pH, redox potential, and competing anions on arsenic mobility (Smedley and Kinniburgh, 2002, Dixit and Hering, 2003). Despite their importance, such experiments are inherently limited by scale, duration, and the difficulty of reproducing natural heterogeneity in aquifers. To overcome these constraints, numerical approaches have become central in recent arsenic research. Widely used reactive transport codes such as PHREEQC (Parkhurst and Appelo, 2013), TOUGHREACT (Xu et al., 2011), and CrunchFlow (Steeffel et al., 2015) integrate flow, geochemical reactions, and transport to predict the behaviour of several dissolved species and mineral reactions in subsurface systems. These approaches provide a robust framework that can be extended to investigate arsenic speciation, sorption-desorption equilibria, and mineral transformations.

More recent studies highlight the importance of surface complexation models to mechanistically represent arsenic-calcite interactions in carbonate-rich aquifers (Renard et al., 2015, Sørensen et al., 2012). At finer resolutions, pore-scale simulations using lattice Boltzmann (LBM) or computational fluid dynamics (CFD) provide a powerful way to explicitly represent pore structures and capture mineralogical heterogeneity (Chen et al., 2022, Yoon et al., 2015). These methods extend beyond experimental constraints, enabling long-term and site-specific predictions of arsenic fate in aquifers subject to environmental perturbations. Experiments provide calibration and validation, while numerical modelling offers predictive capability at scales and conditions not feasible in the laboratory, rendering their integration crucial for assessing arsenic risk in groundwater systems.

3.6 Multiscale Modelling and Image-Based Approaches

Although extensive research on arsenic contamination has been conducted in Fe-rich alluvial aquifers of South and Southeast Asia, where reductive dissolution of Fe-oxhydroxides constitutes the principal mobilisation pathway (Smedley and Kinniburgh, 2002, P. Ravenscroft et al., 2009), investigations in carbonate-dominated aquifers remain comparatively limited. This gap is critical, given the global significance of carbonate lithologies as major aquifer systems, particularly in arid and semi-arid regions.

Advances in reactive transport modelling and CT-based pore-scale imaging have enabled mechanistic investigation of arsenic behaviour in carbonate aquifers. Previous studies employing coupled numerical simulations have revealed that microstructural heterogeneity, pore connectivity, and calcite abundance exert first-order controls on arsenic retention and transport (Wang et al., 2024, Bia et al., 2021). In these studies, model predictions are typically validated against experimental datasets reported in the literature, with varying degrees of agreement depending on the complexity of geochemical interactions and model assumptions. Furthermore, these approaches, as reported in the literature, extend the temporal and spatial scales beyond laboratory constraints and provide a predictive framework for assessing how carbonate buffering capacity governs arsenic immobilisation pathways (Wang et al., 2024, Bia et al., 2021). Furthermore, these approaches provide a framework that can be applied to arsenic systems. In such studies, model predictions are typically validated against experimental datasets reported in the literature, with varying degrees of agreement depending on the complexity of the geochemical interactions and the model assumptions.

Collectively, these findings suggest that, in carbonate aquifers, a contaminant such as arsenic cannot be attributed solely to bulk porosity or permeability, but the behaviour is strongly influenced by mineralogical composition, sorption equilibria, and competitive geochemical reactions. For regions such as Cyprus and the Eastern Mediterranean, where carbonate lithologies predominate, integrated experimental and numerical approaches provide a valuable framework for assessing the long-term fate of arsenic under both natural and anthropogenic perturbations.

3.7 Knowledge Gaps and Research Needs

Although digital rock physics (DRP) has advanced significantly as a tool for quantifying and visualising pore-scale structures, its application in establishing quantitative correlations between petrophysical properties such as porosity and permeability remains restricted. Most studies focus on pore-scale imaging and qualitative assessments rather than linking these structural parameters to macroscopic flow and transport behaviour, representing an important methodological gap—particularly for carbonate formations, where heterogeneity is pronounced. At the same time, much progress has been realised in understanding arsenic geochemistry, yet uncertainties persist regarding its behaviour in carbonate-dominated aquifers. Most global studies have emphasised Fe-rich alluvial systems, whereas the controls on arsenic mobility in carbonate reservoirs are still insufficiently constrained. Sørensen et al. (2008) and Renard et al. (2015), provide valuable insights into calcite-arsenic interactions, but they are often limited by simplified conditions and do not fully capture the heterogeneity of natural aquifers.

Recent advances in numerical modelling have highlighted the significance of pore-scale variability, pore connectivity, and carbonate buffering (Bia et al., 2021, Wang et al., 2024). However, the translation of these findings into reservoir-scale predictions remains a challenge, particularly when porosity, permeability, and mineralogical composition act together to regulate arsenic storage and release.

The present work contributes to addressing these gaps by integrating image-based characterisation, numerical simulations, and reactive transport modelling in the context of carbonate aquifers. This combined approach provides new insights into how porosity-permeability relationships influence arsenic mobility, with specific relevance to the carbonate reservoirs of Cyprus and the broader Eastern Mediterranean.

In parallel, the Nord Stream methane leak presents a large-scale environmental modelling challenge, where determining the total quantity of methane released has been approached using two complementary numerical methods: one based on multiphase flow simulations with OLGA simulator and another employing COMSOL Multiphysics for plume evolution and gas dispersion modelling. These efforts underscore the versatility of advanced numerical frameworks in quantifying coupled flow-transport phenomena and highlight their broader applicability to subsurface contaminant transport studies.



CHAPTER 4:
MATERIALS AND METHODS

UNIVERSITY of NICOSIA

4 Materials and Methods

This section summarises the materials, datasets, and computational approaches employed to investigate fluid flow and arsenic transport in porous carbonate and sandstone systems. The study integrates digital rock physics, micro-CT imaging, and reactive transport modelling to understand how pore structure, flow rate, and geochemical conditions influence arsenic mobility in groundwater. Eleven rock samples from onshore Cyprus were analysed using Avizo (2019.1) to obtain three-dimensional pore-scale images and deduce porosity, permeability, and grain morphology. The derived porosity-permeability relationships were implemented in a MATLAB-based algorithm to generate permeability maps used as structural inputs for subsequent simulations. A multiscale reactive transport model was developed in CrunchFlow to examine arsenic mobilisation and retention under varying hydrodynamic and geochemical conditions, accounting for As(III) and As(V) speciation, surface complexation, and mineral precipitation/dissolution. In addition, computational expertise was further enhanced through a supplementary modelling study of the Nord Stream methane release using OLGA and COMSOL Multiphysics, which contributed to refining the numerical framework adopted throughout this research.

4.1 Methodological Framework of the FabRocks Project

This section presents the integrated experimental and digital workflow used in this study. Carbonate and sandstone core samples were first characterised through porosity and permeability measurements in accordance with API standards, followed by high-resolution micro-CT scanning. The acquired images were reconstructed in Avizo 2019.1 to generate 3D digital rock models and extract key petrophysical properties, enabling a comprehensive analysis of fluid flow behaviour.

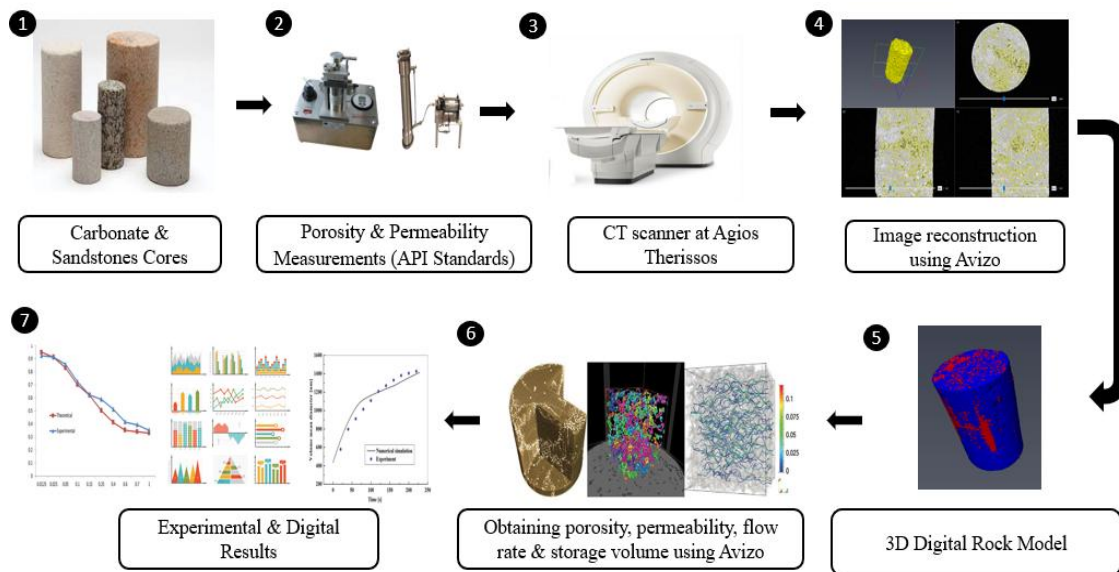


Figure 4.1: Integrated experimental and digital workflow for petrophysical characterisation and 3D rock modelling.

4.1.1 Geological Settings

After obtaining permission from the Cyprus Department of Geological Survey (DGS), which is the island's competent authority for geological matters, the consortium of FabRocks¹ research project identified several physical locations from which rock samples were collected. More specifically, rock specimens were retrieved from the Kantou area in Limassol and from Tochni, Agios Theodoros, and Xylophagou, in Larnaca, Cyprus. Figure 4.2 illustrates the lithological profiles of each section visited during the field expedition, along with the stratigraphic sequences of the collected samples.

¹The FabRocks research project focused on the characterisation and fabrication of digital and physical rock models to investigate pore structure, fluid flow, and storage properties in sedimentary rocks. The project was funded by the Cyprus Research and Innovation Foundation (RIF) under the CONCEPT-HYDRO/0421/0002 programme.

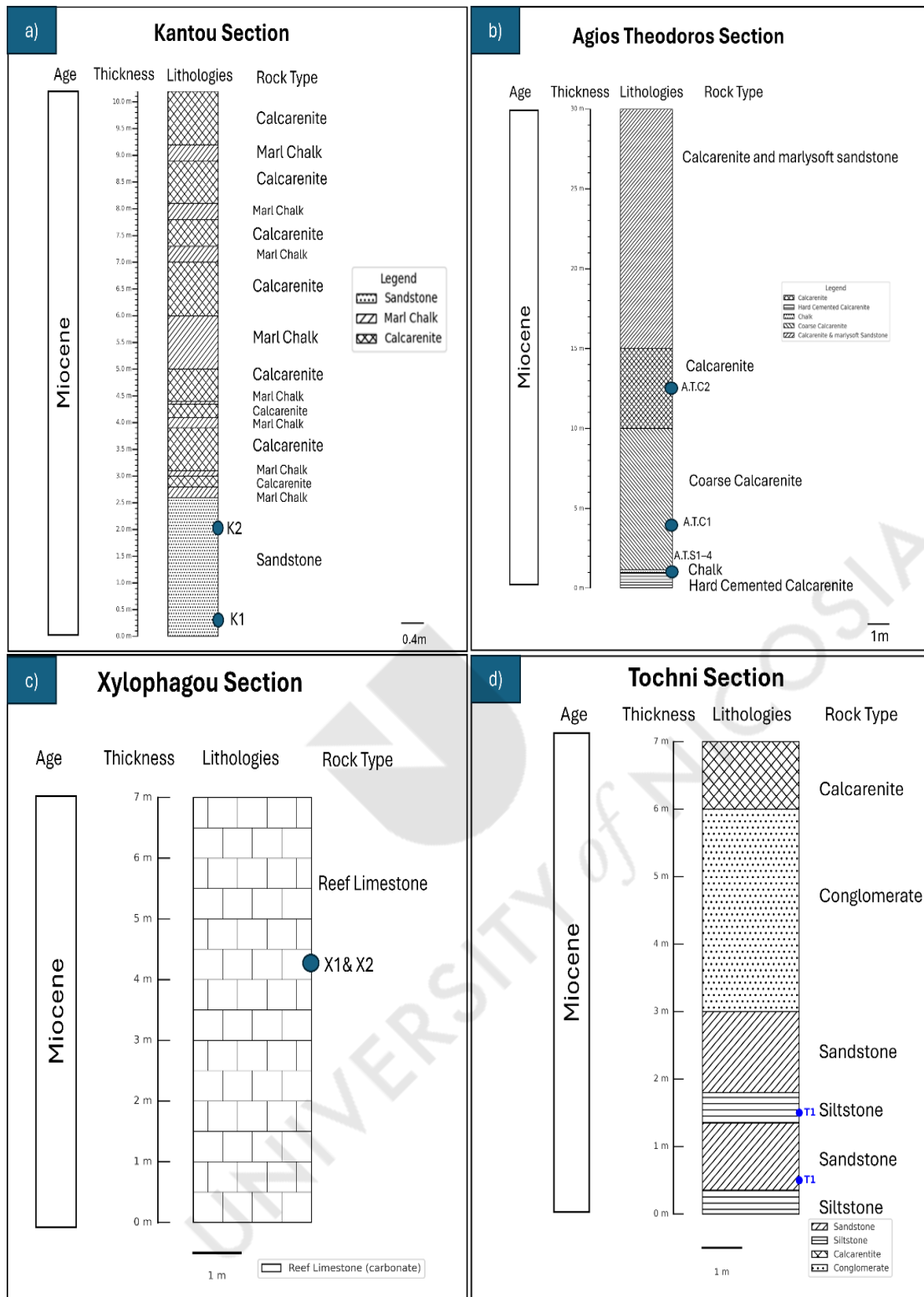


Figure 4.2: Stratigraphic columns of the (a) Kantou, (b) Agios Theodoros, (c) Xylophagou, and (d) Tochni sections, illustrating the sampled sandstone and carbonate outcrops.

Physical locations of the sampling sites are depicted in Figure 4.3. The geological settings of Kantou, Tochni, Agios Theodoros, and Xylophagou villages were shaped by the

Troodos Ophiolite, the Mamonia Complex, and the Messaoria Basin formations, respectively. Rocks belonging to the Mamonia Complex are mainly deep-marine sediments and may serve as analogues to offshore source rocks. The lithologies found at Agios Theodoros, Tochni, and Kantou consist of sandstones and calcarenites, which can be compared to offshore clastic reservoirs. In contrast, the Xylophagou area is characterised by carbonate formations, particularly limestones, making it a good analogue for offshore carbonate reservoirs.



Figure 4.3: Geological map of Cyprus displaying the four sampling locations.

Kantou village located at the southern part of the Troodos Ophiolite is dominated by pillow lavas and sheeted dikes, which were once part of the upper oceanic crust. The geology of the village is associated with sulfide mineralisation and Cyprus-type volcanogenic massive sulfide (VMS) deposits. Of equal geological interest are the Neogene and Quaternary aged sediments, which contain sandstones, calcarenites, marls, and conglomerates. At the villages of Tochni and Agios Theodoros, located in the Larnaca district, one could encounter late Miocene sedimentary rocks, primarily sandstones and calcarenites. These formations were deposited in shallow-marine environments, influenced by fluvial, deltaic, or nearshore processes. However, the Mamonia Complex and the Kannaviou formation, which are much older in age, do not directly pertain to the cores studied in this research. Instead, these Neogene formations provide better analogues for offshore sandstone reservoirs.

Geographically, the village of Xylophagou, situated at the boundary of the Larnaca and the Famagusta districts, is part of the Mesaoria Basin, which boasts thick sequences of Miocene to Pleistocene marine sediments, primarily limestones, calcarenites, and marls. These units constitute a shallow-marine carbonate platform, with evidence of karstification features in the limestones. The area's relatively flat topography also includes quaternary coastal deposits.

Notably, the limestone outcrops from Xylophagou, being carbonate dominant in nature, renders them valuable analogues for offshore hydrocarbon bearing carbonate reservoirs.

The formations listed in Table 4.1 were selected due to their relevance as analogues to hydrocarbon systems in the Eastern Mediterranean, as they exhibit key characteristics of reservoir, seal, and source rocks. Rock samples from the Kantou area contain sandstones from Neogene-Quaternary deposits, which resemble fluvial and coastal sandstone reservoirs. Rock samples from Tochni and Agios Theodoros consist of sandstones and calcarenites potentially serving as source rocks. In contrast, outcrops from Xylophagou are predominantly reef limestones, representing a shallow-marine carbonate platform like some Middle Eastern and Mediterranean carbonate reservoirs. These formations exhibit good secondary porosity emanating from karstification and dissolution, analogous to Egypt’s offshore Zohr gas field. Therefore, studying these core samples provides valuable insights for regional hydrocarbon exploration (Stanton and Macgregor, 2018, Ganat, 2020, El-Fattah et al., 2021).

Table 4.1: Sampling site locations in Cyprus, showing province, projected coordinates (X, Y), and geographic coordinates (latitude and longitude).

Location	Province	Coordinates			
		X	Y	Latitude	Longitude
Kantou	Limassol	491955	3838379	34.665	32.92679
Tochni	Larnaca	529502	3849020	34.78294	33.32245
Agios Theodoros	Larnaca	536508	3847715	34.77095	33.39897
Agios Theodoros	Larnaca	536518	3847731	34.73422	33.39089
Xylophagou	Larnaca	577302	3868146	34.95289	33.84663

4.1.2 Experimental Measurement of Porosity and Permeability

After collecting the rock samples from the geological sites of interest, suitable size cores were obtained by drilling the rock samples and then trimming their edges. In total, 11 cores were extracted from the preceding rock specimens (Figure 4.4).

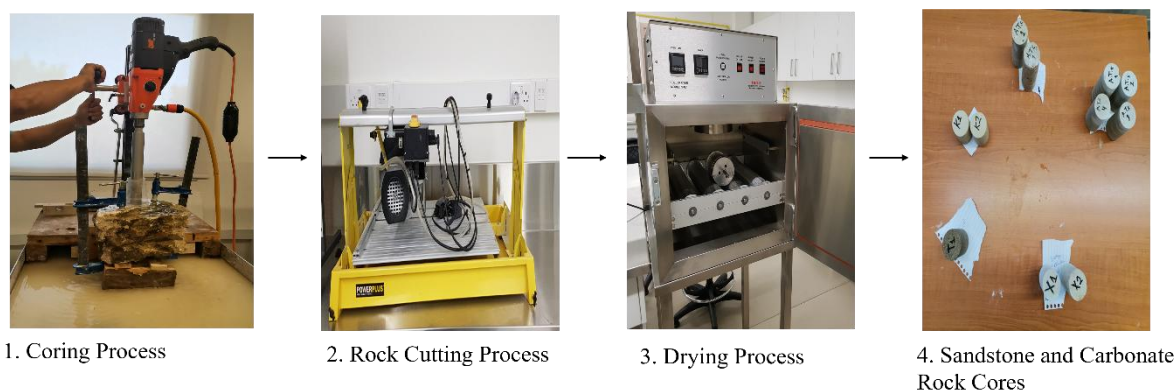


Figure 4.4: Workflow of core sample preparation, including coring, cutting, and drying done at the petrophysics laboratory of the University of Nicosia.

The core samples were prepared at the Petrophysics Laboratory, at the University of Nicosia, which is fully equipped with Routine Core Analysis Laboratory (RCAL) devices, where essential petrophysical tests are conducted. Further to coring and trimming, all rock cores were thoroughly washed with water and oven dried at a temperature of 70°C for a duration of 2 days to preserve any embedded carbonate material liable to the exposure of excessive heat. This setpoint is far below the temperature at which calcite (CaCO_3) decomposes ($\geq 750^\circ\text{C}$) and below the $\sim 80^\circ\text{C}$ which is the dehydration threshold for gypsum. Table 4.2 lists the dimensions of the core samples.

Table 4.2: Physical dimensions of the cylindrical natural rock cores.

Core Name	Rock Type	Average Diameter (mm)	Average Length (mm)
K1	Sandstone	36.33	43.77
K2	Sandstone	36.04	46.24
A.T.C1	Sandstone	36.39	75.53
A.T.C2	Sandstone	36.89	66.83
A.T.S1	Sandstone	36.5	72.91
A.T.S2	Sandstone	36.84	66.15
A.T.S3	Sandstone	36.34	65.91
A.T.S4	Sandstone	36.79	59.31
T1	Sandstone	36.89	67.84
X1	Carbonate	36.83	54.63
X2	Carbonate	36.96	62.64

Helium porosimetry measurements were performed using a Vinci Helium porosimeter, which measures the effective porosity of cores samples by applying Boyle's law in the context of helium gas expansion, in accordance with the American Petroleum Institute (API)

standards. The bulk volume of each sample was determined using a vernier calliper. Individual core samples were placed in a sealed chamber, and the porosimeter was calibrated using a reference volume billet to ensure precision. This reference volume billet is a solid stainless-steel cylinder measuring 36.8mm in diameter and 65.9mm in length. The billet has a volume of 70.06cm³, at 20°C, while measurements exhibit an uncertainty of ±0.5mm. Once the hardware attained equilibrium at 20°C after 30 minutes, the pressure sensors were reset to 0, and an empty cell leak test was run. During this test, the cell was sealed in the absence of a rock core, pressurised to ~300 kPa (3 bar; 43.51 psi), and isolated for 60s. The test has successful provided the pressure drop which was less than 2 kPa (0.02 bar; 0.3 psi). For volume verification, multi-pressure checks (100–500 kPa or 14.5–72.5 psi) were applied. Volume calibration was realised when the computed cell volume matched the billet within ≤0.1% during 3 iterations, which deviated to within 0.05cm³. During measurements, the reference cell was charged to 200psi (≈1,380kPa); then, helium was allowed to expand into the sample cell, and the equilibrium pressure was recorded. The pressure sensor exhibited an accuracy of 0.1%. Grain volume was then calculated using Boyle's law by subtracting the void volume from the total chamber volume. The porosimeter exhibits a precision of ±0.5% and an accuracy of ±1%, ensuring reliable measurement performance. This method yields accurate measurements of effective porosity (Pirrot et al., 2025).

Absolute permeability was determined using a Vinci permeameter in a Hassler-type core holder. Cores were loaded into the sleeve, and a confining pressure was applied to simulate overburden pressure and ensure radial sealing while the confining pressure was kept higher than the pore pressure. Distilled water was used as the test fluid. An upstream water reservoir was pressurised with nitrogen gas to provide a controlled inlet pressure. Nitrogen gas presumably did not completely permeate the core. After steady state was reached, the effluent water was collected in a container of known volume, and the time to fill that volume was recorded to calculate the flow rate. The pressure drop across the core was measured between the inlet and the outlet. Utilising Darcy's law, permeability was determined from the measured flow rate, water viscosity, core dimensions (length and cross-sectional area), and the pressure drop. This procedure yielded reproducible absolute permeability values for the samples, with an accuracy of ±0.01 mD and a precision of ±0.05 mD. Accurate permeability measurements of rock cores are instrumental for evaluating their fluid flow potential and the transmissibility characteristics of petroleum and water reservoirs (El-Fattah et al., 2021).

4.1.3 Micro-CT scans of Sandstone and Carbonate Rocks

After the rock cores were prepared, the next step was to scan them and generate their 2D images (Figure 4.5). These renderings were subsequently used to create digital models of the respective porous rocks. Rock core samples were scanned at the Agios Therissos medical laboratory, in Nicosia, using a Philips 256 CT imaging device (Philips Healthcare, Best, The Netherlands). The cores were scanned using the fine-bone ear/sinus protocol (120 kV). Data were acquired as multiple small, overlapping scans at $15\mu\text{m}$ isotropic voxels, each reconstructed at 1024×1024 pixels and 256 slices. Scanned images overlapped by 10% across the core diameter and along its length and were then fused into a single 3D volume. Pixel spacing and slice thickness from the DICOM headers both measured 0.015 mm.

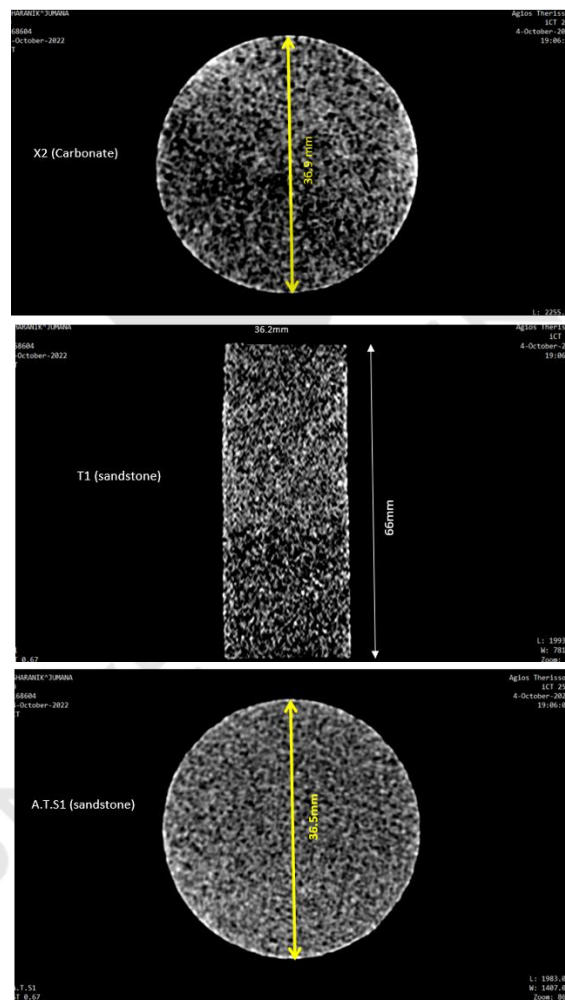


Figure 4.5: Representative DICOM images of carbonate (X2) and sandstone (T1 & A.T.S1) rock cores, showing cross-sectional views (top and bottom) and a longitudinal section (middle). Measured core dimensions are indicated, highlighting differences in internal pore structure and heterogeneity between carbonate and sandstone lithologies.

4.1.4 Image-Based Rock Characterisation and Pore-Scale Modelling

Pore network modelling involves segmenting 2D images of rock samples into pore and solid phases, with the goal of reconstructing the pore space geometry and simulating fluid transport behaviour through the network. The accuracy of such estimations rests on the fidelity of the digital pore network that replicates geometrical and topological features of the natural pore system. The efforts initially focused on identifying a software tool that combines various processes, such as segmentation, re-construction, volume rendering, meshing, and eventually the computation of the rock physical properties. The Avizo materials characterisation suite was used to segment the 2D images. Many subroutines and algorithms, such as the watershed filter, 12 auto-thresholding, axis connectivity, and the object separation function were applied to distinguish between the solid matrix and the pore network of rocks (Figure 4.6).

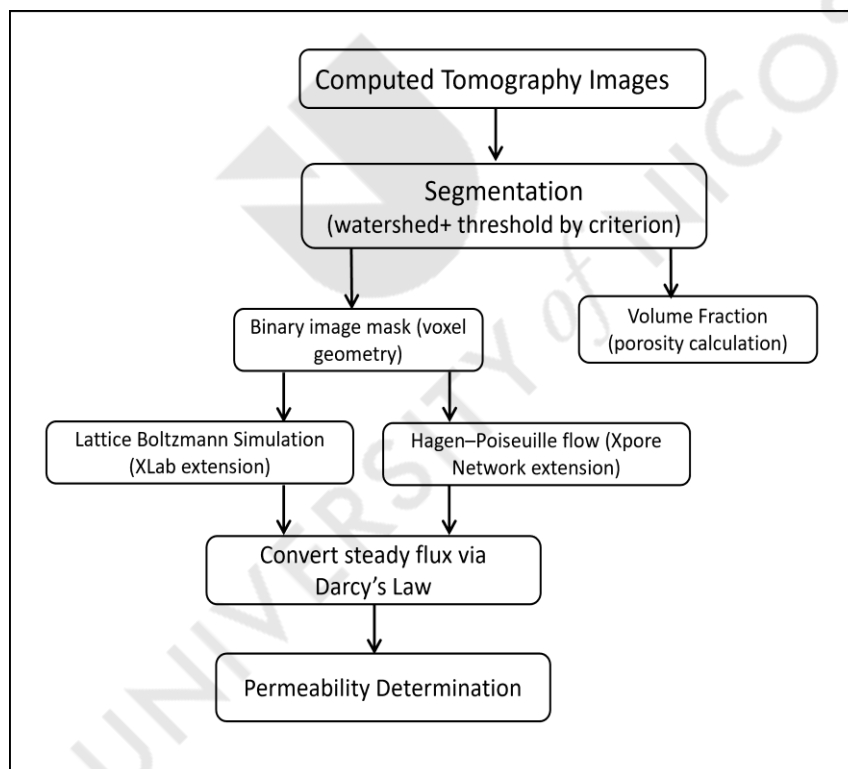


Figure 4.6: Flowchart depicting the process for computing the rock porosity (volume fraction) and permeability, via the Avizo (2019.1) image analysis software.

Porosity was determined using the volume fraction method, which calculates the ratio of pore voxels to total sample voxels. Simply put, Avizo can compute the collective porosity of the pores and their throats. The Avizo network modelling extensions of Xlab and Xpore

(Avizo (2019.1)) were utilised to determine the absolute permeability and the natural gas flow rate through the porous structure.

According to Zhang et al. (2011) Avizo's pore-network module estimates throat conductance using the Hagen-Poiseuille relation. In this study, permeability was computed from the CT-segmented voxel geometry using two independent approaches under single-phase, incompressible, low-Reynold's conditions ($Re \ll 1$): Continuum flow on voxels (Avizo Xlab extension) and Pore-Network Modelling (Avizo Xpore Network extension).

While using Xlab extension, the flow in the creeping-flow (Stokes) limit of the incompressible Navier-Stokes equations was solved using XLab's lattice-Boltzmann method. The governing equations are:

$$\begin{aligned}\nabla \cdot \vec{V} &= 0 \\ \mu \nabla^2 \vec{V} - \nabla P &= 0\end{aligned}\quad (4.1)$$

where $\nabla \cdot$ is the divergence operator, ∇P is the pressure gradient, μ is the dynamic viscosity of the fluid, and ∇^2 is the Laplacian operator.

A pressure drop, dP , was prescribed between the inlet and outlet faces, and no-slip conditions were imposed at the solid surface. After steady state, the global flow rate (Q) is converted to absolute permeability via Darcy's law:

$$Q = \frac{kA}{\mu} \frac{dP}{dx} = g_t (p_i - p_j), \quad g_t = \frac{A_t^2}{\alpha_t \mu \ell_t} \quad (4.2)$$

where Q is the global flow rate supported by the porous medium (m^3/s), A is the cross-sectional area of the sample that the fluid permeates (m^2), k is the absolute permeability (m^2), and μ is the dynamic viscosity of the flowing fluid ($\text{Pa}\cdot\text{s}$).

Flow rates were computed from Darcy's law, using each core's permeability, geometry, the applied pressure drop, and the gas viscosity at laboratory temperature. The second approach utilised the Xpore Network extension, where a pore-throat network was extracted from the binary images. For each throat t between pores i and j , flow is given by Poiseuille conductance:

$$Q_t = g_t (p_i - p_j), \quad g_t = \frac{A_t^2}{\alpha_t \mu \ell_t} \quad (4.3)$$

Q_t is volumetric flow through throat t (m^3/s). Positive flow rate from pore $i \rightarrow j$, g_t is the hydraulic conductance of throat t ($\text{m}^3/\text{Pa}\cdot\text{s}$), $(p_i - p_j)$ denotes the pressure differential at the pore nodes i and j (Pa) connected by throat t , A_t is the throat area, ℓ_t is the length of throat t , μ is the dynamic viscosity of the fluid ($\text{Pa}\cdot\text{s}$), and α_t a shape factor (provided by the Avizo/equivalent-radius model). Nodal pressures satisfy the conservation of mass $\sum_{t \in i} Q_t = 0$. The network's total outlet flow Q is used to derive the medium's permeability using Darcy's law, as shown in equation (4.3).

4.1.5 Synthetic Sediment Pack Modelling (DEM Approach)

Many difficulties were encountered while converting the DICOM into vector images. For this reason, realistic unconsolidated sediments were built using Particula 1.3 (Al Ibrahim et al., 2018). The deposition of grains of specified shape and size for 17 sand pack (structure) distributions was simulated by means of a discrete element method (DEM). Such a robust approach considers the interactions between the individual elements and is commonly used in the context of soil mechanics and geotechnical studies (Al Ibrahim et al., 2018). Because individual grains were successively deposited under the influence of gravity, this process resembles—to a large degree—the natural sedimentation process. In this project, the DEM approach was utilised owing to the possibility of implementing irregularly shaped convex particles. Depending on the application, this may constitute a major advantage as simplified spheres or ellipsoids, generally, do not reflect the granulometric characteristics of natural sandstone and carbonate rocks.

Structurally, the irregularly shaped grains were generated by stochastically perturbing regular shapes by means of a three-dimensionally correlated Perlin noise, whereby the volume of the underlying regular particles was conserved. Considering that each particle exhibits a separate realisation of Perlin noise, all distinct grains are unique in shape and size. Moreover, the selected amplitude of the noise governs the strength of the perturbations and, thus, it offers a good approximation for natural shapes of sub- to well-rounded grains. Primarily, the basic input parameters for generating the synthetic sediments are the grain size distribution and the aspect ratio, which in turn, determine the ellipsoidal grain shape. In this respect, a Perlin noise of 0.75 was used to generate the irregularly shaped particles. The pack consisted of 5,000 quartz grains of a mass-density of $2,650 \text{ kg/m}^3$ and with a controlled size distribution, featuring three distinct grain diameters, namely $50\mu\text{m}$, $35\mu\text{m}$, and $20\mu\text{m}$.

All grains were deposited under the influence of gravity into a cylindrical container measuring 36mm, in diameter, by 66mm, in length. This irregularity in shape, raised inter-particle friction and mechanical interlocking, which in turn enhanced the complexity of the interactions and led to a more realistic packing structure compared to ideal spherical grains. Furthermore, the model considered compaction forces, simulating the gradual densification of the pack as the grains precipitated at the bottom of the container. Key assumptions referred to the grains accumulating in a cylindrical geometry resembling the size of the rock cores under atmospheric pressure conditions.

Thanks to the homogeneous nature of the sandstone sediments, sand packs of sandstones were relatively easy to create. Layers of carbonates, on the other hand, cannot be easily replicated owing to the high heterogeneity that carbonate rocks exhibit. Avizo was also able to deduce the porosity of the constructed packs, like the one illustrated in Figure 4.7.

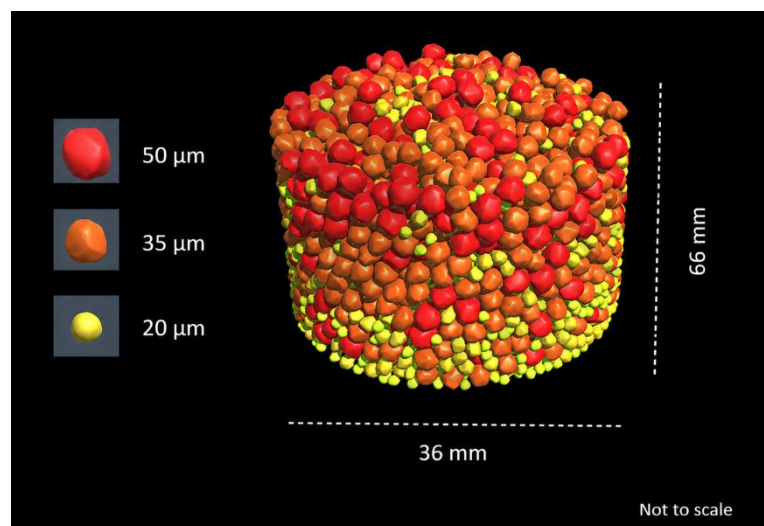


Figure 4.7: Creation of unconsolidated sand packs using the Particula 1.3 software.

After the generation of these samples, the Avizo suite was used to segment, reconstruct, and render the volume of the lattices, as summarised in Figure 4.8. In parallel, it was possible to validate the porosity and compute the absolute permeability, the gas entrained in the pores, and the gas flow rates. Equally important, the same porous material can be replicated if the same properties, such as porosity, grain distribution, and mass density are maintained. In other words, fixing some of these parameters offers control over permeability. Hence, unconsolidated sample material structures were obtained from the same porosity and permeability with minute changes to their internal structure.

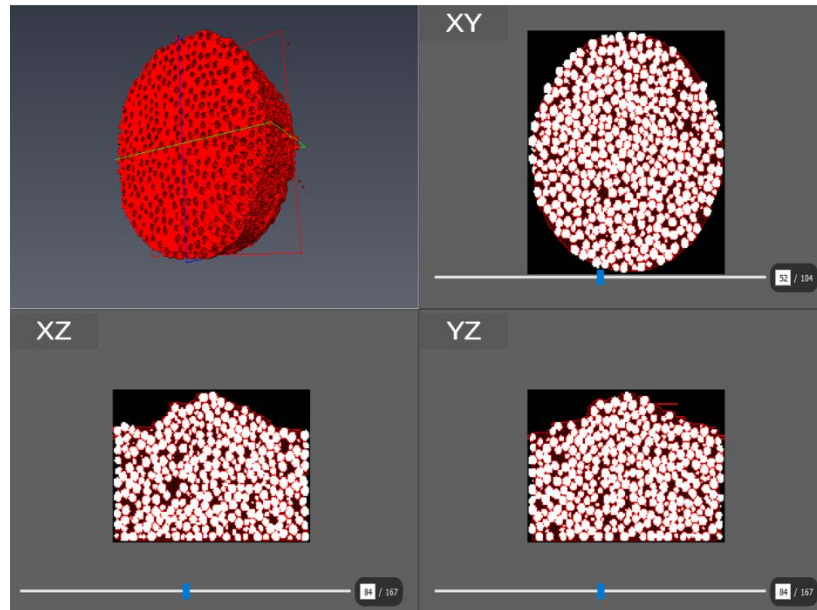


Figure 4.8: Segmentation of an unconsolidated material pack using the Avizo analysis and visualisation tool, showing 3D reconstruction and orthogonal views (XY, XZ, YZ) of the pore structure.

4.2 Framework of Arsenic Behaviour in Carbonate-Rich Aquifers

Most research on arsenic mobility in groundwater systems has focused on Fe-bearing aquifers, particularly those in South and Southeast Asia, where the reductive dissolution of iron oxyhydroxides is recognised as the principal release mechanism. In contrast, carbonate-dominated aquifers, such as those found in Cyprus, remain comparatively underexplored, despite their regional importance as primary groundwater reservoirs. The geochemical behaviour of arsenic in these systems is expected to be fundamentally different, as immobilisation and mobilisation processes are controlled by calcite-arsenic interactions rather than Fe-oxide cycling.

To address this gap, representative carbonate rock samples were collected from the Kantou area (Cyprus) as a particular case study. A combination of X-ray fluorescence (XRF) and X-ray diffraction (XRD) techniques was applied to determine the bulk chemical composition and mineralogical phases, respectively. These analyses provide valuable insights into the lithological framework of the aquifer and establish the mineralogical controls that govern arsenic reactivity in carbonate settings.

4.2.1 Analytical Techniques

This section summarises the analytical characterisation of the Kantou carbonate samples using the X-ray Fluorescence (XRF) and the X-ray Diffraction (XRD) techniques. XRF analysis revealed that sample C459 is a calcite-dominated carbonate rock, containing CaO (49.35 wt.%) as the major oxide, minor SiO₂ and MgO, and trace amounts of metals such as Ni, Cr, Zn, and Sr, confirming its purity and compositional uniformity. Complementary XRD analysis identified calcite (83.8%) and quartz (16.2%) as the main crystalline phases, corroborating the XRF findings. Together, these results establish the chemical and mineralogical framework of the Kantou samples, providing essential input for subsequent modelling of arsenic-mineral interactions and reactive transport behaviour.

4.2.1.1 X-ray Fluorescence (XRF)-based Chemical Composition

X-ray fluorescence (XRF) spectroscopy is a well-established, non-destructive technique for determining the major, minor, and trace element composition of geological materials. The method relies on the excitation of atoms in a sample by a primary X-ray beam, which induces the emission of element-specific secondary (fluorescent) X-rays. The energy and intensity of these emissions are measured to quantify the elemental abundances. For geological applications, powdered rock samples are typically homogenised and pressed into pellets or fused into glass beads to ensure representative and reproducible measurements. XRF is widely regarded as a robust method for bulk chemical characterisation owing to its high accuracy, reproducibility, and minimal sample preparation bias.

Table 4.3: Calibration curve ranges, accuracy, limits of detection (LOD), and limits of quantitation (LOQ) for major oxides and trace elements determined by XRF analysis of the Kantou carbonate samples.

Element/Compound	Calibration Curve Range (mg/kg)	Calibration Curve Accuracy (mg/kg)	Method Limit of Detection (LOD) (mg/kg)	Method Limit of Quantitation (LOQ) (mg/kg)
SiO ₂	2.69-89.43	3.0505	2.69	8.07
K ₂ O	0.02-3.07	0.1093	0.02	0.06
CaO	0.21-50.50	2.7527	0.21	0.63
TiO ₂	0.02-0.98	0.064	0.02	0.06
Fe ₂ O ₃	0.65-47.78	1.3328	0.65	1.95
MgO	0.21-22.36	0.8841	2.17	6.51
Al ₂ O ₃	0.10-17.48	1.0617	0.2	0.6
SO ₃	0.03-46.2	0.9718	0.03	0.09
V	11.4-153.9	18.8164	11.4	34.2
Cr	17.0-143.2	12.2839	17	51
Mn	97.9-1479	64.0713	97.9	293.7
Ni	4.1-112.2	6.1975	4.1	12.3
Cu	3.0-52.1	6.8468	3	9
Zn	19.4-105.11	16.377	19.4	58.2
Rb	24,0-130.02	11.9587	24	72
Sr	27.9-244.5	8.2199	27.9	83.7
Zr	104.7-421.73	12.6534	104.7	314.1
Nb	6.6-16.3	1.3944	2.1	6.3
Cd	0.1-6.74	0.1635	0.72	2.16
Ba	13.7-1049	70.8503	53	159
Pb	15.3-300.3	9.2583	15.3	45.9

To ensure the reliability of the XRF results, instrument calibration and performance parameters were carefully assessed. The Shimadzu EDX-7000 spectrometer was calibrated using certified reference materials covering the expected concentration ranges for both major oxides and trace elements. Table 4.3 presents the calibration ranges, accuracy, method detection limits (LOD), and limits of quantitation (LOQ) for the major oxides and traces.

X-ray fluorescence (XRF) analysis was carried out on carbonate samples from the Kantou area to determine their bulk geochemical composition (Table 4.4). The analysis provided quantitative information on major and minor elemental constituents, which are essential for characterising mineralogical variability and assessing the potential influence of composition on the geochemical behaviour. Among the collected samples, C459 was selected for detailed study because it was the only case where a representative core was available at the Department of Geological Survey of Cyprus. The availability of this rock core allowed for integrated analysis, including imaging, rock characterisation, and subsequent modelling, ensuring consistency between geochemical data and pore-scale observations. Therefore, C459 was considered the most suitable candidate for a detailed study and for linking bulk composition to microstructural and reactive transport behaviour.

Table 4.4: Major oxide composition (mg/kg) (wt.%) of Kantou rock samples determined by X-ray fluorescence (XRF).

Sample Name	Main Oxides Composition (mg/kg)							
	SiO ₂ (%)	K ₂ O (%)	CaO (%)	TiO ₂ (%)	Fe ₂ O ₃ (%)	MgO (%)	Al ₂ O ₃ (%)	SO ₃ (%)
C424	7.62	ND	47.33	0.03	ND	2.91	0.54	0.27
C427	21.64	0.08	38.34	0.04	0.40	0.45	0.80	0.18
C433	3.82	ND	47.74	0.02	ND	1.88	0.51	0.23
C445	11.16	0.18	45.93	0.05	0.13	1.88	1.26	0.20
C452	8.27	ND	46.64	0.02	ND	1.44	0.53	0.20
C455	9.03	ND	46.20	0.02	ND	1.94	0.56	0.21
C459	6.58	ND	49.35	0.02	ND	0.65	0.48	0.21
C461	6.95	ND	49.13	0.02	ND	1.13	0.45	0.24
C466	5.53	ND	50.19	0.02	ND	1.37	0.42	0.29
C470	4.23	ND	50.73	0.02	ND	1.07	0.42	0.24

ND = Not detected.

As shown in Table 4.4, the major oxide composition of C459 confirms the carbonate-dominated nature of the rock, with CaO (49.35 wt.%) as the principal component. Minor but significant amounts of SiO₂ (6.58 wt.%) and MgO (0.65 wt.%) were detected, reflecting the presence of quartz impurities and limited dolomitic substitution. Other oxides, including Al₂O₃ (0.48 wt.%), SO₃ (0.21 wt.%), and TiO₂ (0.02 wt.%), occur only in trace quantities, consistent with a nearly pure calcitic lithology.

Trace element concentrations (Table 4.5) show enrichment in selected metals, particularly Ni (44.5 mg/kg), Cr (6.4 mg/kg), and Zn (16.5 mg/kg), along with Sr (433.4 mg/kg), the latter being typical of calcite-rich rocks where strontium substitutes for calcium in the crystal lattice. Minor amounts of Cu (8.6 mg/kg) and Ba (3.3 mg/kg) were also detected, while heavy metals such as lead (Pb) were below detection limits.

Table 4.5: Traces composition (mg/kg) of Kantou rock samples determined by X-ray Fluorescence (XRF).

Traces Composition (mg/kg)													
Sample Name	V	Cr	Mn	Ni	Cu	Zn	Rb	Sr	Zr	Nb	Cd	Ba	Pb
C424	ND	3.5	2.5	37.1	16.4	ND	3.7	183.1	75.0	6.6	0.4	67.0	ND
C427	ND	9.8	33.2	25.3	13.4	ND	9.3	165.1	80.8	6.8	0.2	60.0	ND
C433	ND	1.7	ND	50.8	6.0	36.3	5.2	182.0	71.5	6.1	0.5	ND	ND
C445	ND	12.2	4.7	38.8	18.3	ND	9.0	300.0	68.5	6.6	0.1	16.8	ND
C452	ND	8.9	26.6	44.9	15.6	ND	6.5	298.7	71.0	6.5	0.3	ND	ND
C455	ND	12.8	8.7	38.0	16.5	ND	5.9	315.3	66.4	6.3	0.3	5.5	ND
C459	ND	6.4	ND	44.5	18.1	ND	1.8	433.4	70.3	6.2	0.2	ND	ND
C461	ND	23.0	ND	42.9	17.3	ND	1.2	445.2	70.9	5.8	0.2	ND	ND
C466	ND	5.8	ND	45.0	20.5	ND	0.1	472.4	69.8	6.1	0.4	ND	ND
C470	ND	4.5	ND	45.4	21.4	ND	0.2	814.0	81.9	5.9	0.1	8.4	ND

ND stands for Not Detected.

Taken together, the XRF results establish that sample C459 is a calcite-dominated carbonate rock with minor quartz admixtures and trace metal enrichments, rendering it representative of carbonate lithologies in the Kantou aquifer system. This chemical framework provides the basis for linking mineralogical composition with sorption-desorption processes relevant to arsenic mobility.

4.2.1.2 X-ray Diffraction (XRD)-based Chemical Composition

X-ray diffraction (XRD) is a widely used analytical technique for identifying and quantifying crystalline phases in geological samples. The method relies on the constructive interference of monochromatic X-rays with the periodic atomic planes of a crystal lattice, as described by Bragg's law. When X-rays strike a powdered sample, they are diffracted at specific angles characteristic of the mineral's crystallographic structure, producing a unique

diffraction pattern (fingerprint) for each phase present (Dinnebier and Billinge, 2008). In practice, the powdered rock samples are exposed to Cu K α radiation under controlled conditions, and the resulting diffractograms are recorded over a range of 2 θ angles. These patterns are then compared with reference databases to identify mineral phases and determine their relative abundances through semi-quantitative analysis. In this study, the XRD results were obtained from the Department of Geological Survey of Cyprus, where phase identification was performed using the International Centre for Diffraction Data (ICDD) Powder Diffraction File (PDF) database. XRD thus provides critical information about the mineralogical composition of the Kantou carbonate samples, complementing the bulk chemical data obtained from XRF.

X-ray diffraction (XRD) analysis was performed on sample C459 to determine its crystalline mineral phases. The diffractogram (Figure 4.9) displays well-defined peaks corresponding primarily to calcite (CaCO₃) and quartz (SiO₂). The major peak near 29.4° 2 θ is characteristic of calcite and corresponds to the (104) crystallographic plane, confirming its dominance in the mineralogical composition, while secondary peaks attributed to quartz appear at ~20.8° (100), 26.6° (101), and 50.1° (112) 2 θ .

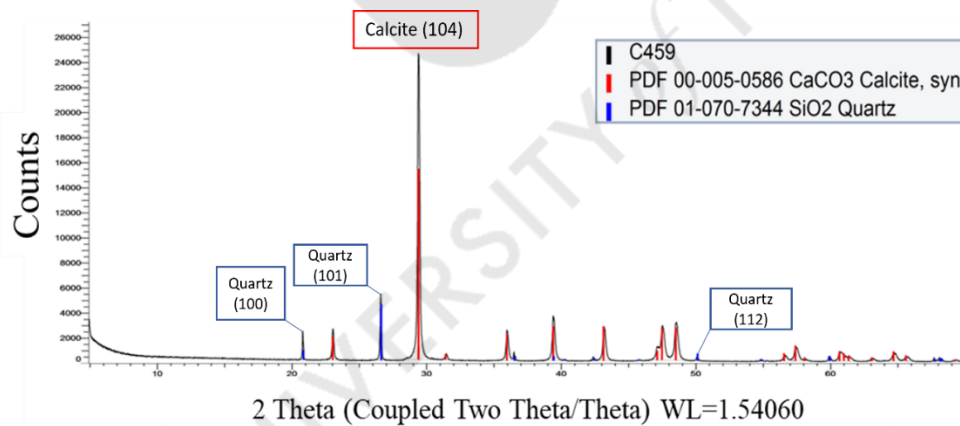


Figure 4.9: XRD diffractogram of sample C459 showing major peaks of calcite (red) and quartz (blue).

Quantitative phase analysis, conducted using Rietveld refinement, indicates that calcite constitutes approximately 83.8% of the sample, while quartz accounts for 16.2%. The refinement was performed by fitting a calculated diffraction pattern, based on known crystal structures, to the measured XRD data using a least-squares approach. This method enables the accurate determination of phase proportions by accounting for peak intensities,

background, and overlapping reflections across the entire diffractogram. The high calcite content aligns with the XRF results, which identified CaO as the dominant oxide, and reflects the carbonate-dominated nature of the samples. The subordinate quartz fraction represents the siliceous detrital input, consistent with the geological setting of the region. This mineralogical composition highlights the predominance of carbonate phases, which play a critical role in pH buffering and in regulating arsenic interactions through adsorption, precipitation, and dissolution processes.

4.2.2 Generation of 2D Domains from Imaging Data for Numerical Modelling

High-resolution imaging and reconstruction provided the link between rock characterisation and reactive transport simulations. By combining thin section petrography, nanoscale cyclotron imaging, and field-scale permeability measurements, a multiscale framework was established to represent the heterogeneity of carbonate aquifers in Cyprus. This approach ensured that both pore-scale processes and aquifer-scale flow properties were captured in numerical models.

4.2.2.1 Nuclear Magnetic Resonance (NMR) Imaging

At the micrometre scale, pore structure characterisation was carried out using Nuclear Magnetic Resonance (NMR) imaging, which provides high-resolution measurements of pore geometry and connectivity without the need for destructive sample preparation (Figure 4.10). NMR techniques are particularly powerful in carbonate systems because they enable the detection of both connected and isolated pores and can quantify pore size distributions through relaxation-time (T_2) analysis. The acquired NMR data were further analysed to extract pore size distribution by correlating T_2 relaxation times with pore radius using established calibration relationships. The acquired NMR data were further analysed to extract pore size distribution by correlating T_2 relaxation times with pore radius using established relationships. Image processing and segmentation were performed using Avizo (2019.1) software, where pore space was distinguished from the solid matrix through thresholding and morphological filtering. The resulting segmented images were then processed in MATLAB to quantify pore size distribution, pore volume fraction, and connectivity metrics which are critical for evaluating fluid flow behaviour. Compared with thin section imaging, NMR also captures sub-micrometre pores and fluid-accessible pathways, thereby complementing petrographic observations.

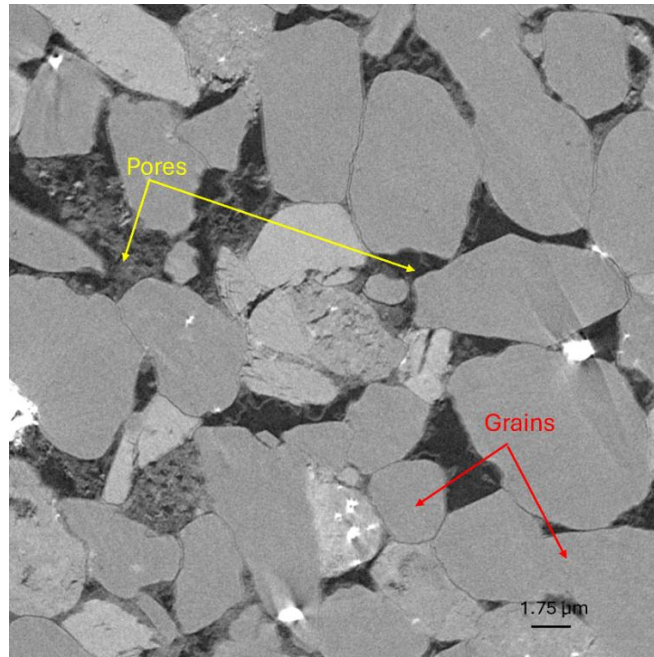


Figure 4.10: NMR-derived microscale image of C459 sample showing pore-solid differentiation. Scale: 1cm = 1.75 μ m.

4.2.2.2 Optical Thin Sectioning

At the millimetre scale, classical thin sectioning was used to capture the pore microstructure of the carbonate rock. A representative core sample (C459) was cut, polished, and mounted to produce 30 μ m-thick sections (Figure 4.11). The sections were scanned at 18cm \times 18cm, corresponding to an actual field of view of 2.25mm \times 2.25mm (calibration: 125 μ m per cm). The images revealed calcite cement, grain contacts, and pore geometry. After digitisation, the images were converted into grayscale and calibrated to differentiate pore space from solid matrix. Binary masks were then produced, which served as the basis for generating permeability maps using MATLAB.

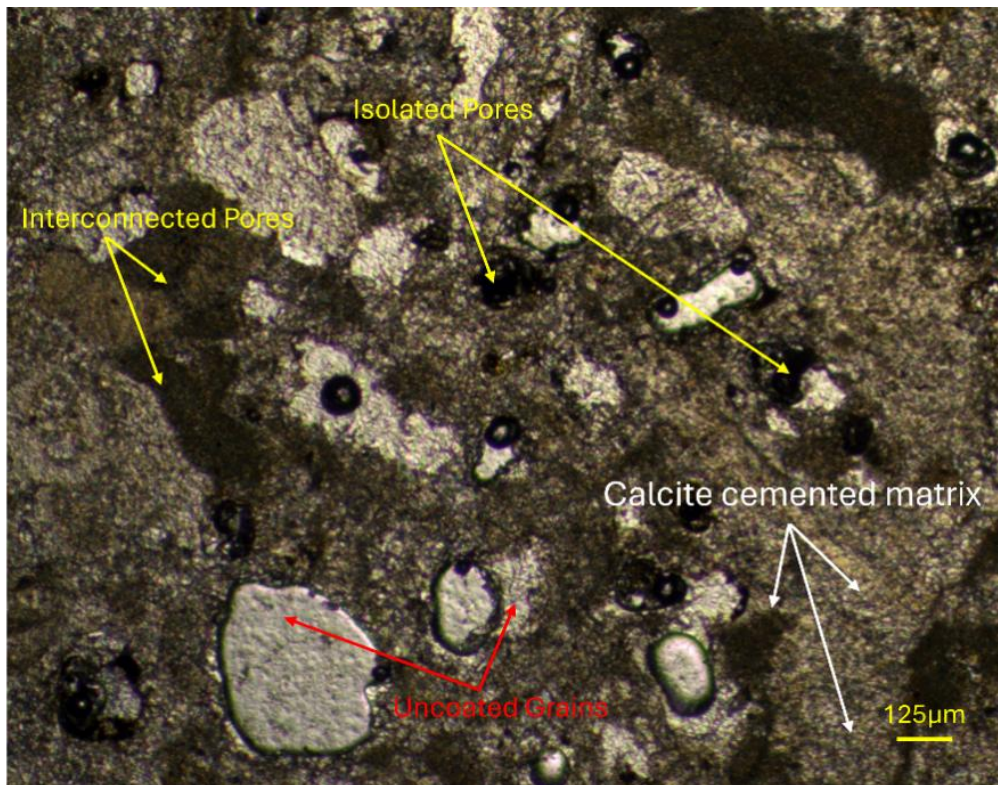


Figure 4.11: Thin section micrograph of a carbonate rock (sample C459) showing pore types and mineral matrix. Scale: 1cm = 125µm.

4.2.2.3 Hydraulic Conductivity Mapping

At the metre scale, no thin section or NMR imaging was possible. Instead, the domain was constructed from directly measured permeability values, which were used to generate a hydraulic conductivity map representative of aquifer-scale variability. The measurements were interpolated to create a continuous field of spatially variable hydraulic properties, ensuring that large-scale simulations captured realistic flow pathways and heterogeneity. This approach grounded the macroscale model in real aquifer conditions, making it more reliable for groundwater quality predictions.

4.2.3 Domain Geometry and Mesh

Three representative 2D simulation domains were constructed at different physical scales to investigate arsenic transport across a range of spatial resolutions: 1) a macroscopic domain (2,000 mm×3,000 mm), 2) an intermediate-scale domain (180 mm×180 mm), and 3) a pore-scale domain (95 mm×95 mm). For the intermediate and fine-scale domains, thin section images were used to define internal structure and spatial heterogeneity. These grayscale images were processed in MATLAB to create binary masks that distinguish pore space from

solid grains. From these masks, spatially variable permeability maps were derived by assigning permeability values across the domain using a defined scaling approach (Figure 4.12).

Each 2D simulation domain was assigned with a uniform thickness of 5 mm to represent a volumetric slice and, at such, support 3D flow computations. A structured grid was used for all cases. The high-resolution domains (intermediate and pore-scale) were discretised using 100×100 grid cells, while the large-scale domain used a coarser resolution of 31×41 cells (Figure 4.12). This ensured numerical stability and efficient computations while preserving the essential geometric and hydraulic features of the subterranean porous media. The permeability maps show clear scale-dependent behaviour. At the micrometre scale, permeability is generally low ($<0.2 \times 10^{-12} \text{ m}^2$, $\sim 0.2 \text{ mD}$) with isolated zones reaching $\sim 1.0 \times 10^{-12} \text{ m}^2$ ($\sim 1 \text{ mD}$). At the millimetre scale, permeability increases to $\sim 0.6\text{--}1.0 \times 10^{-12} \text{ m}^2$ ($\sim 0.6\text{--}1 \text{ mD}$), reflecting improved connectivity and preferential flow pathways. At the metre scale, values range from ~ 0.1 to $1.0 \times 10^{-11} \text{ m}^2$ ($\sim 1\text{--}10 \text{ mD}$) and become more spatially uniform due to upscaling. This trend marks the transition from pore-scale heterogeneity to effective large-scale flow behaviour.

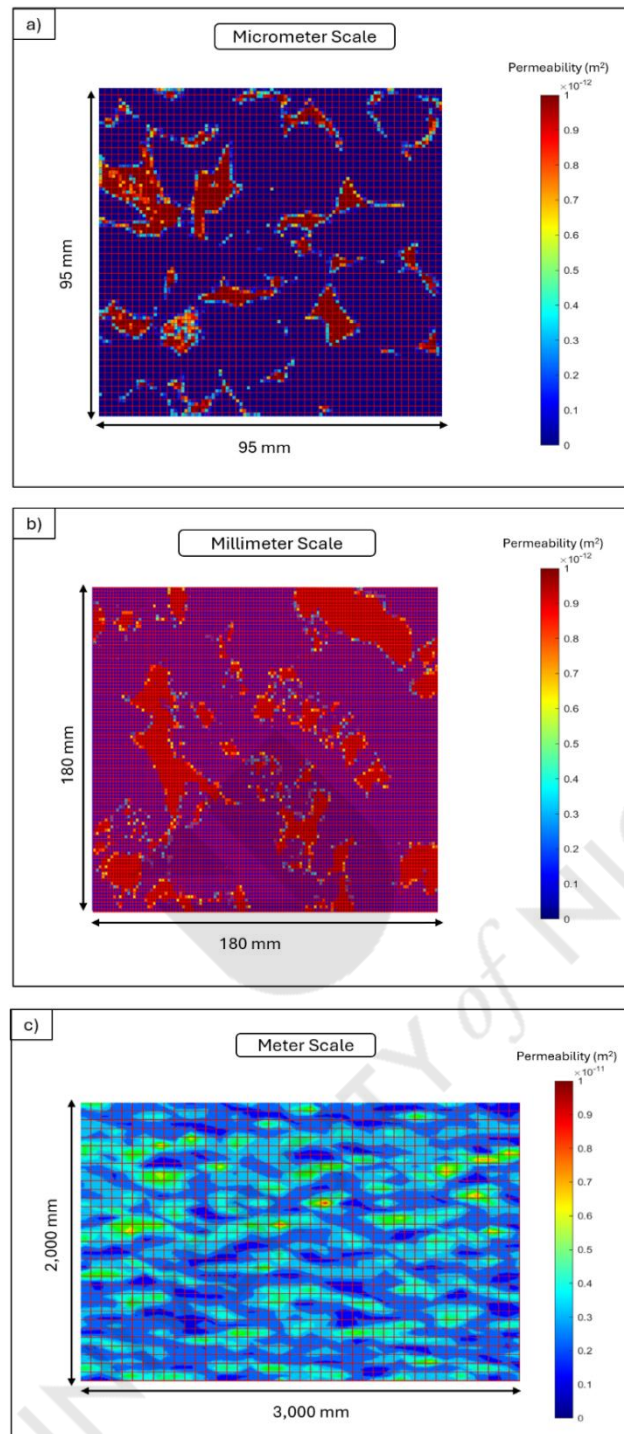


Figure 4.12: Permeability maps across different spatial scales: (a) Micrometre scale, (b) Millimetre scale, and (c) Metre scale representations showing spatial variability in permeability (m^2). The colour gradient from blue to red indicates increasing permeability values, with corresponding scales expressed in scientific notation.

4.2.4 Simulating Arsenic Mobility and Retention Using Crunchflow

CrunchFlow is a continuum-scale reactive transport tool that rigorously solves coupled equations for fluid flow, solute transport, and complex geochemistry in porous media (Steeffel et al., 2015). It tracks advective and dispersive transport while modelling aqueous speciation, kinetic mineral precipitation/dissolution, and both equilibrium and kinetic surface complexation reactions, within a finite-volume framework. This renders CrunchFlow well suited for this study, enabling accurate simulation of arsenic-calcite interactions at multiple scales.

4.2.4.1 Mass Balance Equation

In CrunchFlow, reactive transport in porous bodies is described by a mass-balance equation that captures the combined effects of fluid flow, dispersion, and chemical reactions (Steeffel et al., 2015). Equation (4.4) quantifies how the concentration of each chemical species evolves over time due to advection and dispersion processes and reactions including aqueous speciation, surface complexation, and mineral precipitation or dissolution:

$$\frac{\partial(\phi\rho_f C_i)}{\partial t} + \nabla \cdot (qC_i - D\nabla C_i) = R_{aq,i} + R_{surf,i} + R_{min,i} \quad (4.4)$$

here, ϕ denotes the porosity of the porous medium, ρ_f is the fluid density, and C_i represents the concentration of species i in the fluid phase. The term $\frac{\partial(\phi\rho_f C_i)}{\partial t}$ accounts for the temporal accumulation of the species within the pore space. The divergence term $\nabla \cdot (qC_i)$ represents advective transport due to the bulk motion of the fluid, where q is the Darcy flux. The dispersion and diffusion processes are represented by $-D\nabla C_i$, with D denoting the hydrodynamic dispersion coefficient, which incorporates both molecular diffusion and mechanical dispersion. $R_{aq,i}$ is the rate of aqueous-phase reactions (e.g., complexation, oxidation-reduction), $R_{surf,i}$ represents surface reactions such as adsorption and desorption on mineral surfaces. Finally, $R_{min,i}$ accounts for mineral reactions, including dissolution and precipitation.

4.2.4.2 Surface complexation

Surface complexation modelling in CrunchFlow allows the simulation of chemical interactions between solutes and mineral surfaces by defining surface sites, reactions, and associated thermodynamic constants (Steeffel and Lasaga, 1994, Steeffel et al., 2015). It supports both equilibrium and kinetic formulations and incorporates electrostatic effects in models like the diffuse layer model (DLM). Surface complexation reactions are governed by the law of mass action, expressed generally as:

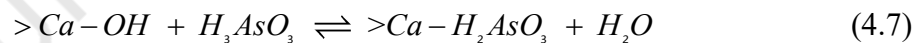
$$K = \frac{\prod_i a_i^{v_i}}{\prod_j a_j^{v_j}} \quad (4.5)$$

where \prod is the product operator, K is the intrinsic equilibrium constant, a represents the species activity, and v is the stoichiometric coefficient. For electrostatically sensitive systems, CrunchFlow adjusts the apparent equilibrium constant using an electrostatic correction term:

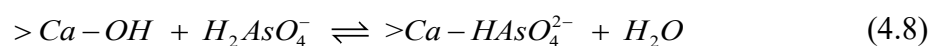
$$K_{eq} = K_{int} \cdot \exp\left(\frac{zF\psi_o}{RT}\right) \quad (4.6)$$

here K_{int} is the intrinsic equilibrium constant, z is the ionic charge of the sorbing species, F is the Faraday constant, ψ_o is the surface potential, R is the universal gas constant, and T is the absolute temperature, in Kelvin.

In this study, surface complexation reactions were used to simulate the adsorption of arsenic species onto calcite surfaces of pH 8, at 25°C. The calcite surface was represented by $>Ca-OH$ groups, which participate in ligand exchange and electrostatic interactions with arsenic species. The selection of pH 8 reflects typical groundwater conditions in carbonate aquifers, where buffering by calcite maintains near-neutral to slightly alkaline environments. According to Lin and Puls (2000), Arsenite (As(III)), manifests predominantly as the neutral molecule H_3AsO_3 at this pH, and adsorbs weakly onto the surface via:

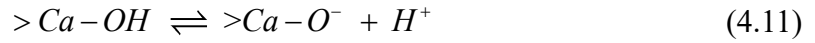
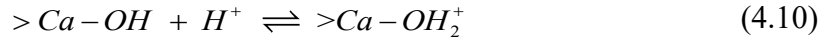


In contrast, arsenate (As(V)) exists as anionic species mainly in the form of $HAsO_4^{2-}$ and $H_2AsO_4^-$ displaying stronger interactions with the calcite-coated grain surfaces in the rock matrix (Farquhar et al., 2002, Vital et al., 2019). These occur through monodentate and bidentate complexation reactions expressed by the following equations :





Surface protonation and deprotonation reactions (4.10) and (4.11) were also considered to account for pH-dependent changes of the surface charges, which govern arsenic sorption (Dzombak and Morel, 1991):

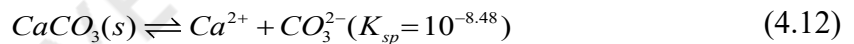


This modelling approach helps elucidate the various adsorption and desorption behaviours of As(III) and As(V) under near-neutral pH conditions pertinent to many natural and engineered environments. Such understanding is critical, as surface complexation directly controls arsenic retention or release, thereby affecting its concentration and potential contamination risks in ground freshwater.

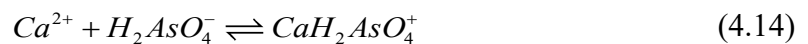
4.2.4.3 Precipitation and Dissolution of Arsenic

In addition to adsorption via surface complexation, precipitation and dissolution processes play a crucial role in controlling arsenic mobility in subsurface environments. These processes contribute to the long-term retention of arsenic through mineral precipitation, especially in carbonate-rich systems with elevated calcium levels. Under such conditions, arsenic can form low-solubility secondary minerals or co-precipitate with calcite, thereby reducing its aqueous concentration (Guo et al., 2007, Farquhar et al., 2002).

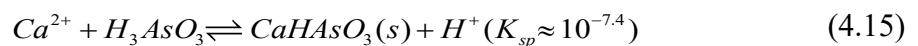
The dissolution and precipitation of calcite govern the availability of both pH and calcium. This fundamental equilibrium is represented as:



At near-neutral pH conditions, arsenate species may react with calcium to form low-solubility arsenate minerals:



While Arsenite (As(III)) is typically more mobile, it can also participate via the following reaction:



These K_{sp} values are used in CrunchFlow to determine mineral saturation and control equilibrium precipitation/dissolution. Thermodynamic data were compiled from the literature and relevant databases (Palmer and Wittbrodt, 1991, Zhu and Anderson, 2002, Serkiz et al., 1996). Additional aqueous species and mineral reactions were incorporated into the B-dot and ThermoChimie databases, the latter being a thermodynamic database providing equilibrium constants and properties for chemical species in geochemical modelling, using data derived from the EQ3/6 framework.

Incorporating these reactions in the model captures key geochemical interactions between arsenic, calcium, and carbonate minerals. It also enables the more accurate simulation of arsenic sequestration potential in natural or engineered systems. Calcite plays a dual role by buffering pH and modulating arsenic speciation, which together influence the extent of precipitation and adsorption.

4.2.5 Arsenic Contamination Scenarios

The modelling framework explored a series of scenarios combining varying levels of solid-phase arsenic contamination with reactive groundwater flow across multiple spatial scales (Table 4.6). All simulations were conducted at a constant temperature of 25°C, assuming a groundwater pH of 8.0 and a neutral rock matrix environment (pH = 7.0), representative of carbonate-rich subsurface conditions. Hydraulic forcing was applied by maintaining a constant pressure of 57.2 psi (3.9 atm) at the inlets and atmospheric pressure at the outlet, enabling water to flow through the domain under realistic gradients.

In the first scenario, the effect of flow rate on arsenic transport was investigated by expanding groundwater pumping rate from 0.36 L/h to 1,800 L/h across three spatial domains capturing the influence of scale-dependent transport and reactivity. This setup allowed for the identification of hydrologic regimes in which arsenic retention is either promoted or suppressed.

Subsequent simulations targeted varying levels of rock contamination. In the low contamination case, 20% of the calcite matrix was initially substituted with calcium arsenate ($\text{Ca}_3(\text{AsO}_4)_2$) while arsenic-bearing water with a total concentration of 4 $\mu\text{g/L}$ permeated the rock matrix from the inlets. Identical water chemistry and scaling were applied in the moderate (60%) and high (100%) contamination scenarios to evaluate the impact of mineral-bound arsenic content on aggregate mobility.

Finally, a dilution scenario was introduced at each contamination level and spatial scale, in which clean groundwater without arsenic was injected at a constant flow rate of 500 L/h.

This case was used to explore the potential for arsenic removal and long-term desorption dynamics under flushing conditions.

Table 4.6: Summary of the key model parameters, boundary conditions, and geochemical processes used in the reactive transport simulations.

Parameter	Value
	Metre: 2×3 m
Spatial Scale	Millimetre: 4.5 × 4.5 mm Micrometre: 16.6 × 16.6 μm
Inlets	Location: Right, Left, Bottom Overburden pressure: 57.2 psi (3.9 atm)
Outlet	Location: Top Pressure: 14.7 psi (1 atm)
Groundwater Arsenic Concentration	4 μg/L (Dilution scenario: 20 μg/L initially)
pH	Rock Matrix: 7.0 Groundwater: 8.0
Temperature	25°C
Mineralogy	Calcite (primary phase) Calcium arsenate (Ca ₃ (AsO ₄) ₂) as contaminant
Rock Matrix Contamination Levels	<ul style="list-style-type: none"> • Low: 20% • Moderate: 60% • High: 100%
Simulation Duration	Short-term simulations: 24 hours Dilution scenario: 50 years

Pumping/Flow Rates	0.36 L/h to 1,800 L/h (0.0001 L/s to 0.5 L/s)
Surface Complexation	Modelled on calcite using constant capacitance model Site types: weak and strong
Arsenic precipitation/dissolution	Included $\text{Ca}_3(\text{AsO}_4)_2$ formation and dissolution with K_{sp} -based equilibrium

4.2.6 Model Development and Reactive Transport Framework

The simulation domain was initialised with a neutral rock matrix environment ($\text{pH} = 7.0$), representative of carbonate-rich subsurface conditions. The solid phase primarily consisted of calcite, partially contaminated with arsenic incorporated as calcium arsenate ($\text{Ca}_3(\text{AsO}_4)_2$), mimicking realistic scenarios in which arsenic is embedded within mineral phases.

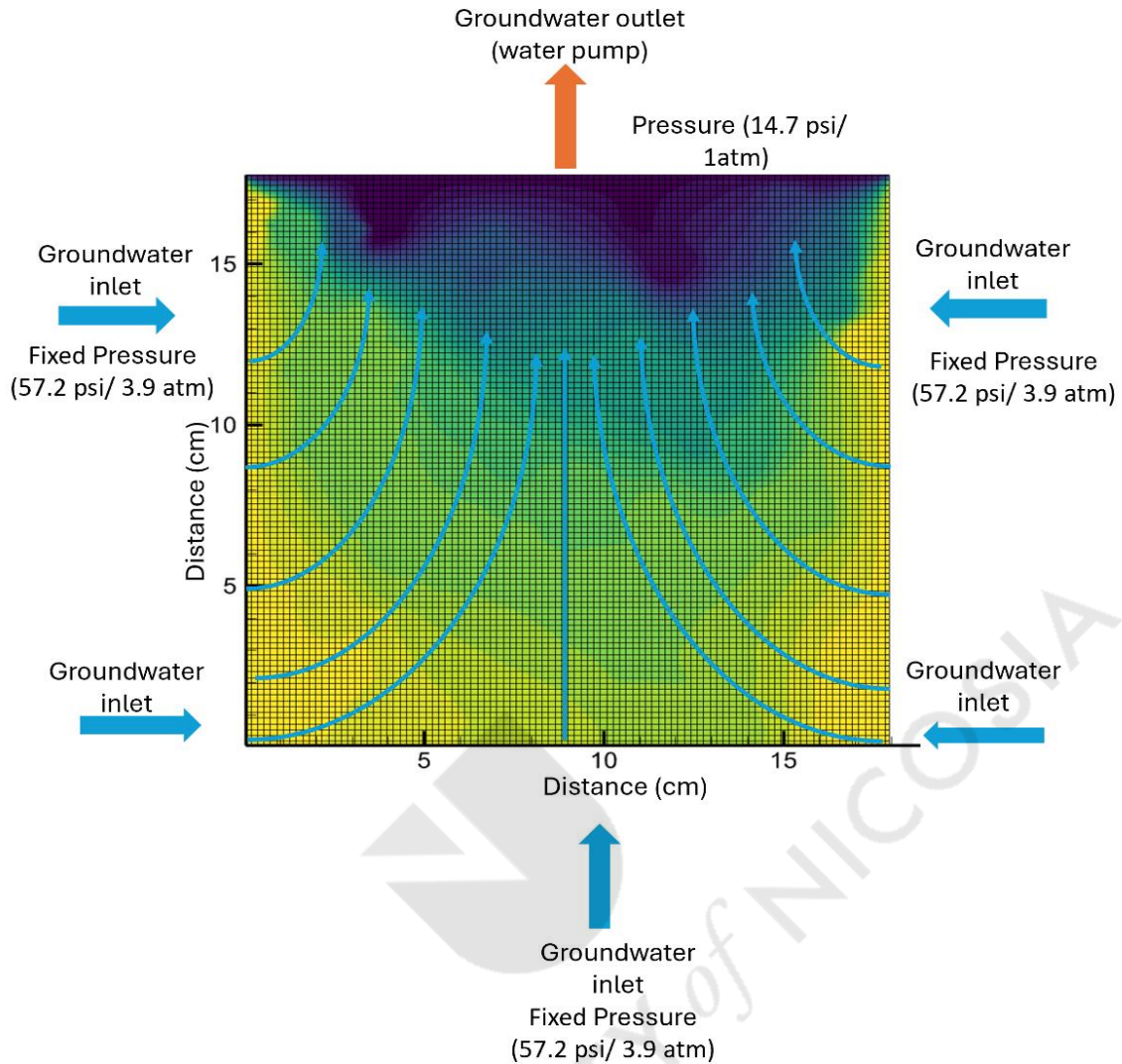


Figure 4.13: Reactive transport model of arsenic in groundwater under pump-induced upward flow, in a 2D porous medium.

Figure 4.13 illustrates Arsenic-bearing groundwater that was introduced through three inlets positioned at the left, right, and bottom boundaries. A single outlet at the top boundary was used to mimic water extraction. A range of pumping rates, from 0.36 L/h to 1,800 L/h, was tested to evaluate how varying hydrodynamic forcing influences arsenic transport and retention.

The inflowing water which exhibited a pH of 8.0 and a total arsenic concentration of $4 \mu\text{g/L}$ was selected to represent realistic groundwater conditions in Cyprus, where arsenic concentrations are commonly within low to moderate ranges and typically below the WHO guideline value of $10 \mu\text{g/L}$ (Christodoulidou et al., 2012, Golfopoulos et al., 2021). Along with this, low concentrations of calcium and carbonate species to maintain buffering capacity.

Surface complexation on calcite was modelled using a constant capacitance approach with both weak and strong site types. Site densities and equilibrium constants were derived from the CrunchFlow thermodynamic database to ensure compatibility with the software's internal geochemical framework. Transient simulations utilised adaptive time steps spanning from 0.001 hours (3.6s) to 0.01 hours (36s). Key properties that comprised porosity, permeability, and surface site coverage, were dynamically updated to reflect changes due to sorption, mineral dissolution, and precipitation. This allowed a fully coupled assessment of geochemical and hydrological feedback during arsenic migration.

4.3 Framework for Modelling Methane Leakage from Nord Stream Pipelines

As a side project, a complementary computational study was undertaken to simulate the methane release following the Nord Stream 1 and 2 pipeline ruptures in the Baltic Sea, in September 2022. The purpose of this exercise was to strengthen the numerical modelling expertise applied in this thesis by analysing multiphase flow dynamics under transient marine conditions.

The simulation was conducted using OLGA, a dynamic multiphase flow simulator designed to model coupled gas-liquid transport in pipelines, in conjunction with COMSOL Multiphysics for validation and visualisation. The pipelines were assumed to contain dry methane (specific gravity 0.55) at initial pressures of 175 bar for Nord Stream 1 and 105 bar for Nord Stream 2, each extending 1,224 km in length with a uniform internal diameter of 1,153mm. The model incorporated Baltic Sea bathymetry, with depths ranging from 63m to 180m, to capture hydrostatic pressure variations along the route (Figure 4.14).

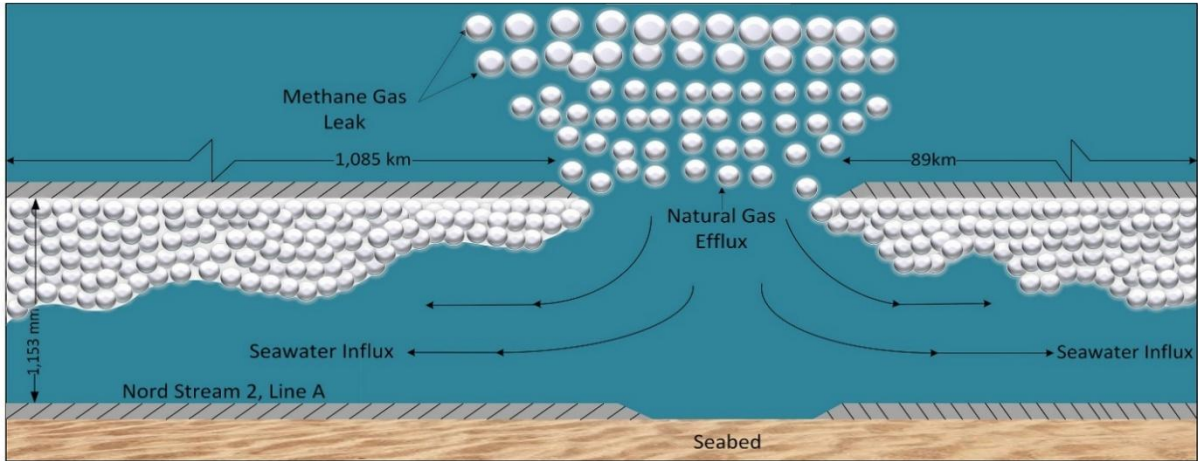


Figure 4.14: Rendering of a breached cross-section of the Nord Stream 2 pipeline displaying the concurrent leakage of gas out of the pipeline and the line seawater flooding during the early stages of the leak Drawing not to scale.

The two-fluid model solved the mass, momentum, and energy conservation equations numerically to simulate methane discharge and seawater intrusion through the ruptured sections:

$$\partial_t m_i + \partial_z (m_i U_i) = \sum_j \psi_{ji} + G_i \quad (4.16)$$

where U_i the mass field velocity, ψ_{ji} denotes the rate of mass transfer between the seawater and the natural gas mass systems and G_i constitutes a mass source/sink. Likewise, two momentum balance expressions were considered for the continuous water phase and the modelling of gas liquid droplets, concisely denoted by:

$$\partial_t (m_i U_i) + \partial_z (m_i U_i^2) = m_i \cdot g \cdot \cos(\varphi) + P_i + G_i U_i + \sum_j (\psi_{ji}^+ U_j - \psi_{ji}^- U_i) + \sum_j F_{ji}^l (U_j - U_i) - F_i^w U_i \quad (4.17)$$

where ψ is the pipe angle of inclination, P_i is the pressure force, ψ_{ji}^+ and ψ_{ji}^- refer to the net contribution emanating from mass field i to j and mass field j to i , respectively. Here, F_{ji}^l accounts for the frictional forces between the i -th and j -th mass field whereas F_i^w is the wall friction. Besides determining the volume of the fluids, the transient model considered the following energy balance equation:

$$\partial_t (m_i E_i) + \partial_z (m_i U_i H_i) = Q_i + \sum_j T_{ij} E_j + S_i \quad (4.18)$$

Term H_i is the field enthalpy, E_i refers to the field energy, Q_i represents the heat flux through the pipe wall, symbol T_{ij} denotes the energy transfer between the fields and, finally, S_i is an enthalpy source/sink.

Boundary conditions included hydrostatic backpressure from seawater and transient outflow at the ruptured sections. Thermophysical properties were defined using Multiflash thermodynamic correlations, and OLGA's High-Definition (HD) stratified flow model was employed to capture detailed gas-liquid interactions.

The combined OLGA-COMSOL simulations estimated that about 478,000 tonnes of methane were released into the atmosphere over a five- to seven-day period, making it the largest recorded submarine gas leak. Beyond its environmental implications, this study provided practical experience in modelling coupled flow and transport processes, reinforcing the computational framework utilised in the main groundwater contamination analysis.

CHAPTER 5: RESEARCH FINDINGS



5 Research Findings

This chapter presents the main outcomes of the study, combining laboratory analyses, digital rock physics, and numerical modelling to evaluate fluid transport and contaminant behaviour in porous media. The results include image-based characterisation of sandstone and carbonate samples, multiscale reactive transport simulations of arsenic mobility, and a computational side study on the Nord Stream methane leak. Collectively, these findings provide a comprehensive assessment of how pore structure, permeability, and geochemical conditions influence fluid flow and reactive processes in subsurface environments.

5.1 Results and Analysis of Rock Characterisation

This section presents the main results derived from laboratory measurements, digital rock analysis, and numerical simulations performed on sandstone and carbonate samples collected from carefully selected locations onshore Cyprus. The outcomes encompass both experimental determinations of porosity and permeability, and their digital counterparts obtained through image-based modelling in Avizo (2019.1). The comparison between measured and simulated values provides insights into the reliability of digital methods for characterising petrophysical properties and assessing pore-scale flow behaviour. Additionally, the section discusses the microstructural features revealed by micro-CT imaging, the statistical relationship between porosity and permeability, and their implications for reservoir quality, storage capacity, and flow performance. These results establish the foundation for subsequent numerical simulations of reactive transport processes and contaminant migration in carbonate aquifers.

5.1.1 Experimentally Determined Porosities and Permeabilities

Both the porosities and the permeabilities of the eleven natural rock cores are shown in Table 5.1. Sandstone cores possess a porosity that ranges between $\approx 19\%$ and 32.5% . Notably, carbonate cores, such as X1 and X2, exhibit high porosities that range between 30.7% and 33.1% . The preceding values indicate that these cores are highly porous and could potentially constitute good reservoir formations. Porosity alone is not sufficient to evaluate the quality of sandstone and carbonate reservoir rocks. Although it indicates the total void fraction available for fluid potential storage, it does not provide enough information about the connectivity of the pore space. Permeability must also be considered, as it reflects the ability of fluids to flow

through the rock. Only by combining porosity and permeability can the storage capacity and producibility of a reservoir be reliably assessed.

Table 5.1: Experimentally obtained core porosity and permeability measurements.

Core Name	Experimental Porosity (%)	Porosity SD (%)	Experimental Permeability (mD)	Permeability SD (mD)
K1	29.10	0.25	2.044	0.03
K2	27.03	0.22	2.141	0.02
A.T.C1	18.99	0.20	<1	-
A.T.C2	22.10	0.21	<1	-
A.T.S1	27.62	0.24	<1	-
A.T.S2	22.39	0.23	<1	-
A.T.S3	25.97	0.21	<1	-
A.T.S4	22.88	0.22	<1	-
T1	32.51	0.25	3.188	0.05
X1	30.67	0.21	0.049	0.07
X2	33.10	0.24	0.031	0.06

SD = Standard deviation across triplicate measurements ($n = 3$).

Determining the permeability of the core samples proved to be more challenging than initially anticipated. Due to the relatively tight nature of the rocks, measurable flow was obtained only for a subset of samples, including K1, K2, T1, X1, and X2, with permeability values ranging from 0.03 mD to 3.188 mD. For the lower-permeability cores, steady-state flow rates were extremely small; values below 1 mD could still be quantified but required prolonged measurement times—often several hours to a few days—to accumulate sufficient effluent volume at a stable pressure differential. When the observed flow remained below the detection threshold of the instrument, permeability was reported as “<1 mD,” indicating a methodological limitation rather than an absence of flow. Collectively, these results suggest that the analysed cores are generally tight and likely represent heterogeneous or low-permeability intervals within the reservoir system rather than high-quality, productive zones.

In total, eleven cores underwent CT scanning to generate three-dimensional digital volumes, from which six representative samples were selected for detailed reconstruction and pore-scale modelling. Porosity and permeability were quantified using the Avizo 2019.1 software suite, as summarised in Table 5.2. The computed digital porosity values were, on average, 1.97% higher than laboratory measurements (95% confidence interval: 1.60–2.34; paired t -test, $p = 3.6 \times 10^{-5}$), indicating a consistent yet small positive deviation with strong

overall agreement. For the three samples with experimentally derived permeability (K1, T1, and X2), statistical comparison of the $\log_{10}(k)$ values revealed that the Xpore-derived permeability was approximately 1.43 times higher than the laboratory results, while the Xlab method yielded values around 1.40 times greater—both within acceptable uncertainty limits. This close correspondence confirms the reliability of the digital rock approach for estimating permeability trends.

The coexistence of high porosity and low permeability implies that much of the pore volume is poorly interconnected or separated by narrow throats, thereby restricting fluid flow despite significant total void space. From a reservoir perspective, such characteristics denote favourable storage capacity but limited flow potential. Consequently, permeability must be evaluated alongside porosity when assessing or predicting the hydraulic performance of porous formations.

Table 5.2: The experimental and digital porosities and permeabilities of various sandstone and carbonate rock cores.

Core Name	Experimental ϕ (%)	Digital ϕ (%)	$\Delta(\phi)$ (%)	Experimental k (mD)	Absolute k (mD) via Xpore Network Modelling	Absolute k (mD) via X-Lab Extension	$\Delta\log_{10}(k)$ (Xpore-Exp)	$\Delta\log_{10}(k)$ (Xlab-Exp)
X2	33.1	35.2	2.10	0.031	0.049	0.047	0.179	0.177
T1	32.51	33.92	1.41	3.188	3.873	3.856	0.085	0.083
A.T.S2	22.39	24.56	2.17	-	3.569	3.554	-	-
K1	29.1	31.23	2.13	2.044	3.089	3.069	0.199	0.181
A.T.C1	18.99	20.67	1.68	-	1.568	1.537	-	-
A.T.C2	22.1	24.43	2.33	-	1.672	1.656	-	-

5.1.2 The Porosity-Permeability Relationship in Sandstone Cores

The numerical analysis of the sandstone cores revealed a clear relationship between porosity and permeability (Figure 5.1). As demonstrated in Figure 5.1 the coefficient of determination (R^2), which amounts almost to 1, captures a perfect straight-line relationship between porosity and permeability. Sandstone samples establish a clear porosity-permeability correlation, as reflected by the gradient of the straight line, which is almost 1 and intersects the origin. There seems to be a linear relationship between these two physical rock properties. This means that an increase in porosity will be accompanied by a rise in permeability. As

porosity increases from 0% to 35%, permeability grows from 0 mD to 3.34 mD. This relation is valid for all scanned natural sandstone cores. For example, the A.T.S2 core possesses a porosity (ϕ) of 24.6%, while T1 exhibits a higher porosity of 33.9%. Likewise, the permeabilities for A.T.S2 amounted to 3.57 mD while T1 boasts an even higher permeability of 3.87 mD. Apparently, the homogenous nature of the sandstone cores explains their porosity-permeability correlation. However, caution should be exercised when interpreting these results as the cohort of core samples tested is rather limited. Thus, to draw more concrete conclusions the investigation needs to be expanded to consider a wider spectrum of samples possessing a broader range of permeabilities.

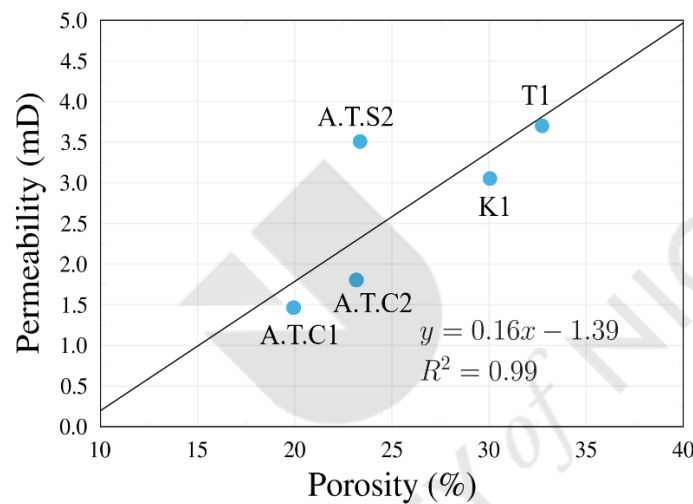


Figure 5.1: Relationship between porosity and permeability for sandstone natural cores. The blue dots correspond to natural sandstone cores (T1, K1, A.T.S2, A.T.C1, and A.T.C2). The black line represents the best-fit linear regression through these cores' values.

5.1.3 Gas Volumetric Flow Rate-Permeability Relationship in Sandstone Cores

To date, Darcy's law has been extensively applied in the analysis of fluid flow behaviour in porous media. Among others, currently, the law is used for rock core investigations, reservoir characterisation and fluid flow simulations (Kovalchuk and Hadjistassou, 2019). As suggested by Darcy and Edwards (1984), four different flow regimes can be observed in porous media depending on the flow velocity and the properties of the porous body. These four regimes comprise: (1) pre-Darcy, (2) Darcy or laminar, (3) Forchheimer, and (4) turbulent flow. Generally, the differentiation between the flow regimes is based on the

Reynolds number, with flow transitions in porous media considered smooth, albeit lacking a distinct threshold.

The Reynolds number in a porous medium can be obtained from $Re = (\rho U d) / \mu$, where ρ is the fluid mass density, U is the fluid velocity, μ is the dynamic viscosity of the fluid, and d is the average diameter of the grains in the porous medium. In the laminar flow domain, the Reynolds number is smaller than 1 (Kovalchuk and Hadjistassou, 2019). In this regime, the flow is dominated by viscous forces, and the pressure gradient varies linearly with the flow rate. However, the Forchheimer flow is characterised by intense inertial effects, and the pressure gradient is a parabolic function of the flow rate.

Being smaller than 1, these Reynolds numbers indicate the presence of laminar flow in the rocks (Dybbs and Edwards, 1984). The average Reynolds number for the samples examined herein was ≈ 0.72 , thus lending credibility to the utilisation of Darcy's law which is applicable to laminar flow conditions. Figure 5.2 depicts the linear relationship between the natural gas flow rate (fm^3/s) and the pressure gradient ΔP (psi) where $R^2 \approx 1$. It must be noted that other sandstone natural cores show similar linearity with different slopes. Furthermore, Figure 5.2 demonstrates the application of Darcy's law and confirms that the flow regime is creeping, so the gas is treated as an incompressible fluid.

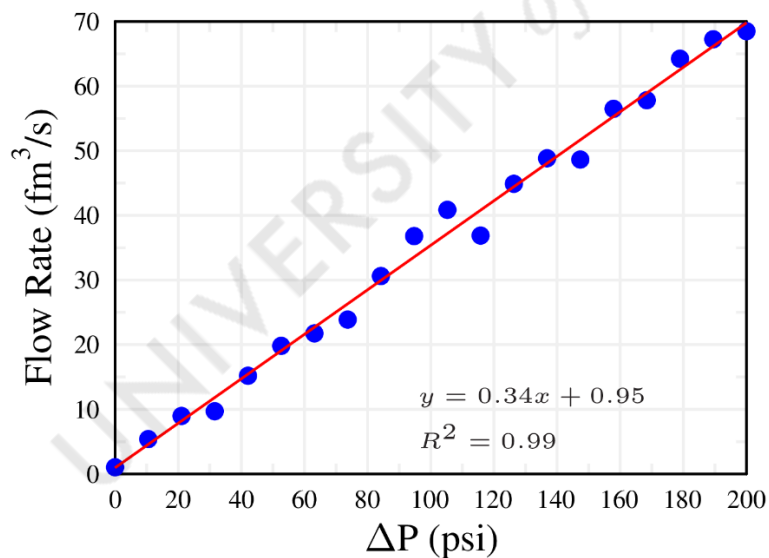


Figure 5.2: Correlation between the natural gas flow rate and the pressure gradient ΔP for a sandstone natural core (K1). The blue dots are measured data points whereas the red line is their linear regression.

To further demonstrate a linear correlation of the gas flow rate as a function of pressure, the relationship between the gas flow rate and the rock permeability were considered. Figure 5.2 displays the gas volume flow rate relative to the porous medium's permeability (mD).

Figure 5.3 reveals that as permeability increases, the gas flow rate rises proportionally. More specifically, the volumetric gas flow rate almost doubled from 13 fm³/s, at 1.568 mD, to 36 fm³/s when permeability increased to 3.873 mD. It also becomes apparent that the rock samples exhibiting high permeability and constant porosity, sustain a significantly elevated gas flow rate. As expected, enhancing the permeability of a sandstone sequence exerts a bigger impact on the gas flow rate compared to higher porosity. Finally, the gas production rate and the recovery of the natural gas are more sensitive to changes in permeability than fluctuations in porosity.

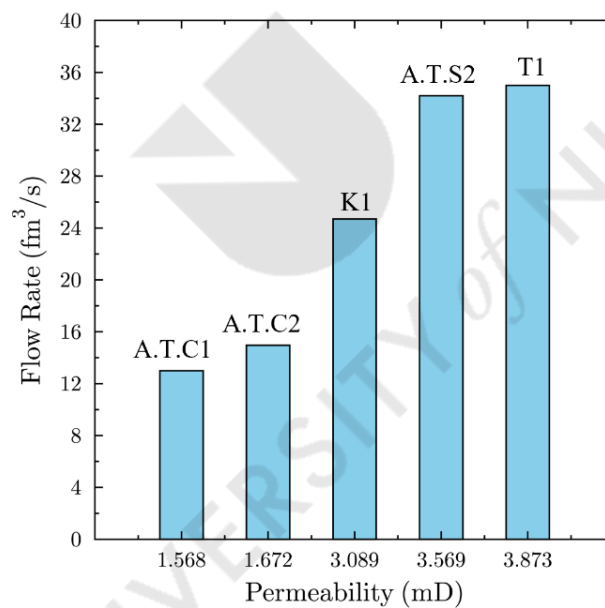


Figure 5.3: Magnitude between the gas flow rate and permeability for sandstone natural cores.

It is important to note that the flow rates derived from permeability-flow correlations (Figure 5.3) and those obtained from porosity-flow relationships (Figure 5.4) are not expected to coincide. In the first case, flow is directly related to permeability, which governs pore connectivity and fluid transport. In the second case, flow is inferred indirectly from porosity, which only reflects void space and is a weaker predictor of transmissivity. The discrepancy

between the two approaches underscores the dominant role of permeability in controlling fluid flow, whereas porosity provides complementary but less definitive insights.

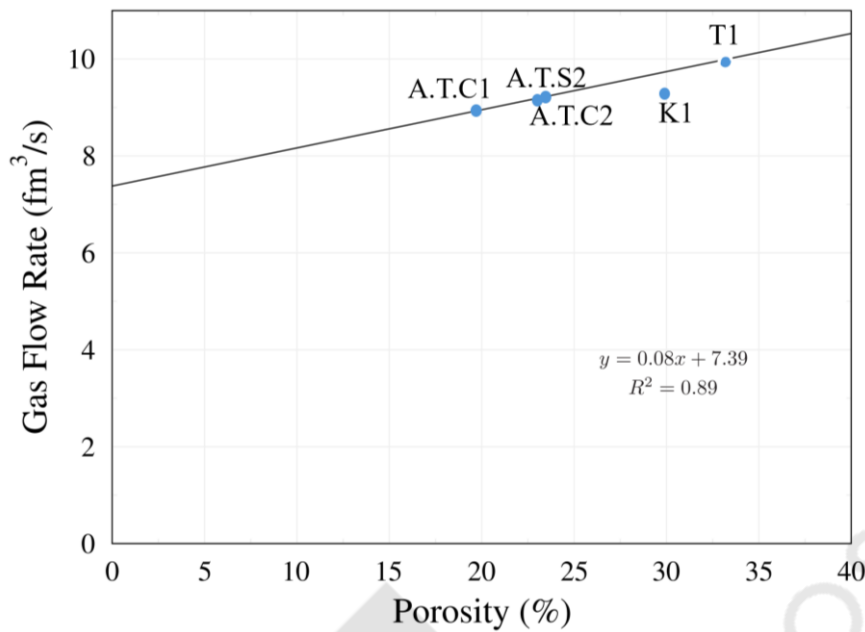


Figure 5.4: Relationship between natural gas flow rate and porosity for the sandstone natural cores. The blue dots correspond to natural sandstone cores (T1, K1, A.T.S2, A.T.C1, and A.T.C2). The black line represents the best-fit linear regression through these cores' values.

5.1.4 Gas Volumetric Flow Rate-Porosity Relationship in Sandstone Cores

To further validate the relationship between porosity and permeability of the real sandstone cores, another parameter considered was the gas volumetric flow rate (in femto cubic metres per second, fm³/s). Clarifying the relation between porosity and gas flow rate can improve the accuracy of reservoir performance predictions and support the optimisation of natural gas production strategies. Figure 5.4 shows the variation in the volume flow rate (fm³/s) of the gas as a function of porosity (%). Additionally, Figure 5.4 demonstrates that the increase in porosity does not exert a proportionate impact on the gas flow rate. Therefore, the enhanced porosity does not seem to play a major role in boosting natural gas production.

5.1.5 Storage Capacity-Porosity Relationship in Sandstone Packs

Besides the influence of porosity and permeability on the gas flow rate, the storage capacity or the volume of the gas entrained in the porous media was computed. Table 5.3 lists

the volume of gas entrained in various sand packs as part of a parametric investigation considering a porosity range spanning between 5% and 35%.

Table 5.3: The variation in gas volume as a function of the porosity and the sand pack's permeability.

Pack Number	Porosity (%)	Permeability (mD)	Gas Volume ($\times 10^{-15} \text{ m}^3$)
1	5	0.75	3.59
2	10	0.98	7.18
3	15	1.27	10.77
4	20	1.66	13.53
5	25	1.87	17.21
6	30	2.47	21.55
7	35	3.34	25.14

Increases in porosity and permeability enhance the gas holding capacity of the rocks and the stored gas volume. In other words, natural gas storage is collectively affected by the structure's porosity and permeability. Since the sandstone samples' permeabilities are very small compared to the permeabilities of other natural gas reservoirs, which can range between 100 mD and 800 mD, it can be inferred that, in this case, gas storage is chiefly governed only by porosity. These packs are tight with low permeabilities, so they transmit only small flow rates; the gas that can enter the connected pore network and be stored/delivered is very small.

Therefore, a higher natural gas storage capacity is possible only if the rock porosity is appreciable. Figure 5.5 displays the relationship between rock porosity and the gas volume.

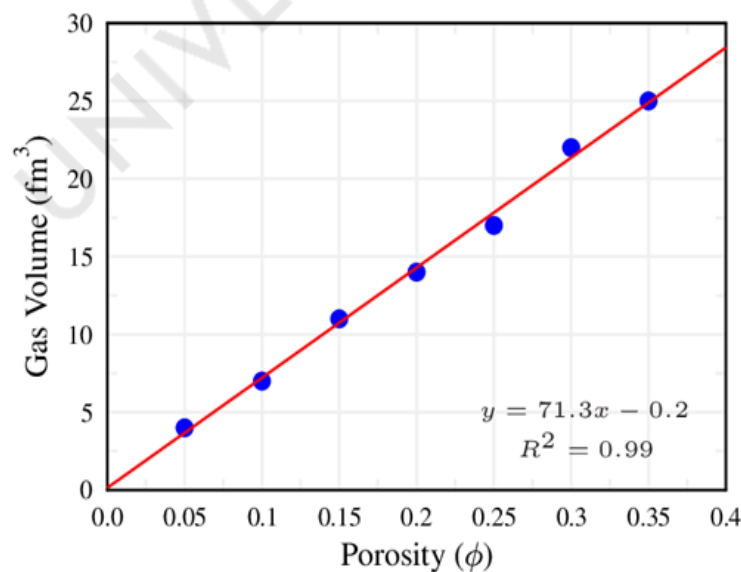


Figure 5.5: Variation of the gas volume inventory relative to the rock porosity for sand packs. The blue dots are the measured gas volumes for seven different sand packs while the red line is the linear regression of the recorder data.

A coefficient of determination (R^2) of almost 1 reveals a linear function (straight line fit) between the stored gas volume and the rock porosity (Figure 5.5). That is, the obtained linear relation facilitates the calculation of the gas volume storage capacity of the sandstone cores as a function of lithological porosity. For in sandstone cores, it was possible to obtain the corresponding natural gas volume, as shown in Table 5.4.

Table 5.4: The respective gas volume of natural sandstone core samples at specific porosities.

Core Name	Porosity (%)	Gas Volume ($\times 10^{-15} \text{ m}^3$)
T1	33.92	24.18
A.T.S2	24.56	17.5
K1	31.23	22.26
A.T.C1	20.67	14.73
A.T.C2	24.43	17.14

5.1.6 The Impact of Granular Roundness on Storage Capabilities

The impact of the grains' roundness on the storage capabilities of sandstone lithologies has been examined using the Particula 1.3 software package. As mentioned earlier, several sand packs were prepared, each exhibiting distinct roundness and grain size. Individual sand packs were collected in a cylindrical container, carefully designed to replicate the dimensions of its corresponding natural rock core. Moreover, the porosity, 3D volume, and gas volume of each sandstone accumulations were determined, as illustrated in Table 5.5.

Close inspection of the results in Table 5.5 reveal that when the grains assumed a more spherical shape, as reflected from an increase in their roundness indicator from 0 (no roundness) to 1 (perfectly spherical shape), an enhancement in rock porosity is induced from 30% to 41%, which translates into a 26.8% boost in porosity. In parallel, the stored gas volume grew by 47.6% to 42 fm^3 (femto cubic metres).

Table 5.5: The variation of porosity and gas volume in relation to grain roundness.

Grain Roundness	Porosity (%)	Gas Volume ($\times 10^{-15} \text{ m}^3$)
0	30	22
0.1	33	26
0.2	35	29
0.3	37	30
0.4	38	31
0.5	38.3	32
0.6	38.7	32
0.7	39	35
0.8	39.4	37
0.9	39.8	40
1	41	42

5.2 Results and Interpretation of Arsenic Transport Behaviour

This part presents the key outcomes of the multiscale reactive-transport simulations, highlighting how pumping rate, spatial scale, and rock-matrix contamination jointly shape arsenic mobility and retention in carbonate aquifers. Across all cases, higher flow rates increased arsenic release and reduced retention, with the strongest effects observed at the micrometre and millimetre scales. Increasing contamination levels amplified mobilisation, while desorption tests confirmed hydrodynamic control on arsenic liberation. Long-term dilution reduced aqueous concentrations but only slightly changed the solid-phase inventory, reflecting the strong buffering capacity of carbonate systems. Overall, the results demonstrate the importance of scale-aware modelling for predicting arsenic behaviour under different groundwater extraction scenarios.

5.2.1 Effect of Flow Rate on Arsenic Transport Across Scales

A series of simulations was first conducted at a low level of rock matrix contamination (20%) across the three spatial scales. At the macroscale (metre level), increasing the pumping rate from 0.36 L/h to 1,800 L/h led to a notable rise in total arsenic concentration in the extracted water from 3.47 $\mu\text{g/L}$ to 17.54 $\mu\text{g/L}$ (Figure 5.6). This trend indicates that higher water flow rates enhance the mobilisation of arsenic previously adsorbed onto or precipitated with calcite, resulting in greater flushing of arsenic into the aqueous phase.

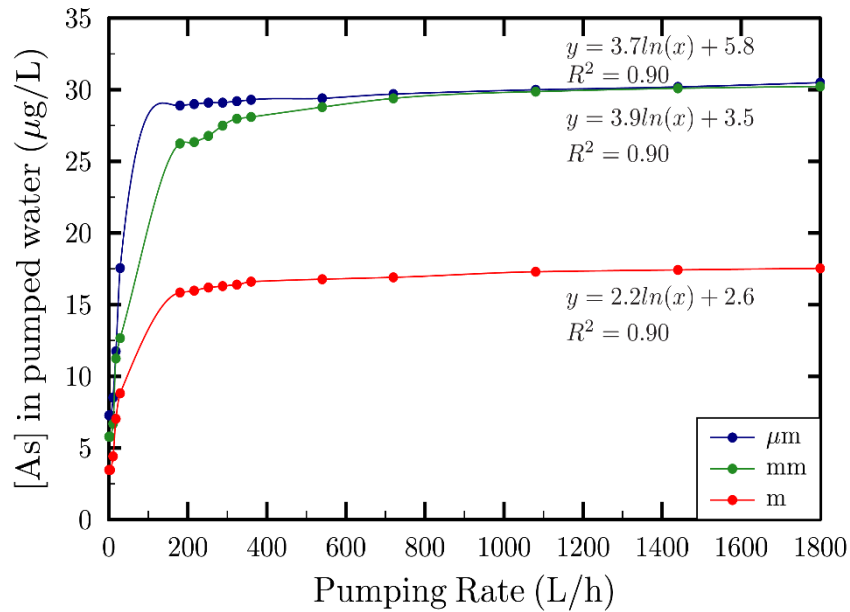


Figure 5.6: Arsenic concentration in pumped water ($\mu\text{g/L}$) as a function of the pumping rate for different porous media scales (μm , mm , m) where rock matrix contamination is set at 20%.

At low pumping rates ranging from 0.36 L/h to 50 L/h, arsenic concentrations increased gradually at the outlet (Figure 5.6) from 3.47 $\mu\text{g/L}$ to 8.82 $\mu\text{g/L}$. As the flow rate entered the moderate range between 50 L/h and 500 L/h, arsenic concentrations continued to rise from 8.82 $\mu\text{g/L}$ to 15.85 $\mu\text{g/L}$, reflecting the more rigorous interactions between the flowing water and the contaminated matrix. When the pumping rate reached the high range between 500 L/h to 1,800 L/h, the arsenic concentration contamination level became less pronounced, rising only slightly from 15.85 $\mu\text{g/L}$ to 17.54 $\mu\text{g/L}$ (Figure 5.6). This suggests that most of the readily mobilisable arsenic had already been flushed, and additional surges in flow rate contributed minimally to further release. These findings highlight the critical role of hydrodynamic forcing in controlling arsenic transport, with lower rates allowing for greater retention while higher water rates are poised to be more efficient and yet enhancing arsenic flushing.

At the millimetre scale, arsenic concentrations in the extracted water surged from 5.79 $\mu\text{g/L}$ to 30.23 $\mu\text{g/L}$ as the pumping rate grew from 0.36 L/h to 1,800 L/h. Even though the overall pattern was observed at the meter scale, the magnitude of arsenic release was considerably higher at this finer scale. For instance, at a moderate pumping rate of 180 L/h, the arsenic concentration reached 26.25 $\mu\text{g/L}$, compared to only 15.85 $\mu\text{g/L}$ at the same flow

rate at the metre-scale domain. When the pumping rate was further increased to 1,800 L/h, arsenic concentration continued to rise, ultimately monotonically peaking at 30.23 $\mu\text{g/L}$. This enhanced release can be attributed to the greater surface reactivity and reduced retention efficiency at smaller spatial domains, where faster transport limits the time available for arsenic to adsorb onto or precipitate with the mineral matrix.

As shown in Figure 5.6, at the microscale, arsenic concentrations has risen from 7.28 $\mu\text{g/L}$ to 30.5 $\mu\text{g/L}$ as the pumping rate ballooned from 0.36 L/h to 1,800 L/h, following the same general trend observed at the larger scales. However, the magnitude of arsenic mobilisation was even more pronounced. At a moderate pumping rate of 180 L/h, arsenic concentration reached 28.9 $\mu\text{g/L}$, compared to 26.25 $\mu\text{g/L}$ at the millimetre scale and 15.85 $\mu\text{g/L}$ at the meter scale. At high water flow rates, the concentration peaked at 30.5 $\mu\text{g/L}$ — like the millimetre scale. These results suggest that arsenic retention through adsorption or precipitation is less effective at smaller scales, where the available surface area is reduced and contact time between groundwater and the rock matrix is shorter. As a result, flushing becomes the dominant process, and a greater fraction of arsenic is released into the extracted water.

To confirm and reinforce these findings, an additional set of simulations was conducted under higher levels of rock matrix contamination, with arsenic incorporation lifted to 60% and then to full saturation of 100% (Figure 5.7).

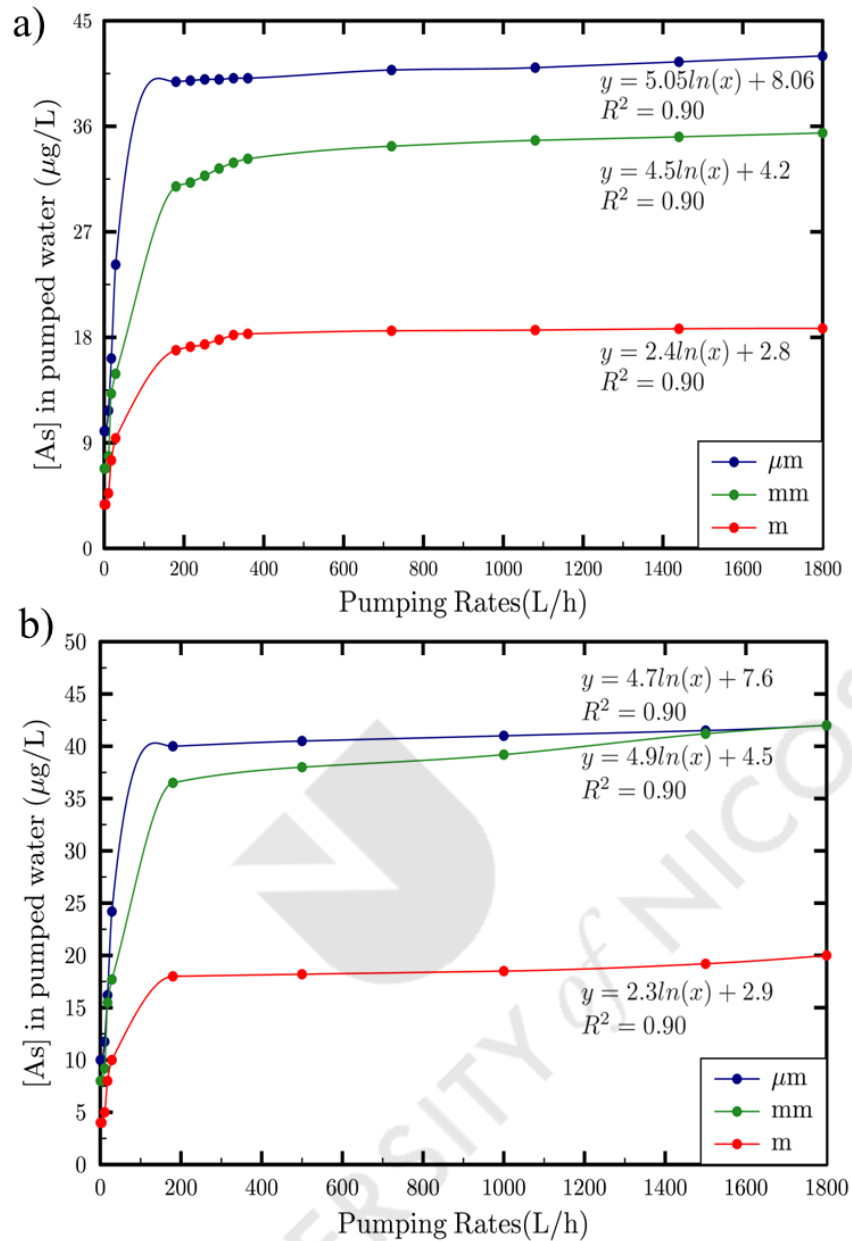


Figure 5.7: Arsenic concentrations in pumped water as a function of pumping rate across three spatial scales (μm , mm, m) for two levels of rock matrix arsenic contamination: a) 60% and b) 100%.

As shown in Figure 5.7, these simulations were also performed across the three spatial scales to ensure consistency and comparability. Throughout all conditions, the same trend of increasing arsenic mobilisation with higher flow rates was observed, confirming that the relationship between hydrodynamic forcing and arsenic release holds even under more heavily contaminated conditions. The results, illustrated in the graphs, further demonstrate how scale, flow rate, and contamination level jointly influence arsenic transport behaviour.

5.2.2 Influence of the Rock Matrix Contamination Level

To investigate the influence of rock matrix contamination on arsenic mobility, additional cases were considered under moderate and high pumping rates across all three spatial scales (Figure 5.8). Here, the level of arsenic contamination in the solid phase was broadened from 20% to 60%, and then to complete saturation (100%). At the metre scale, arsenic concentrations in the extracted water expanded by 7.6% when contamination rose from 20% to 60%, and by an additional 6.23% when the contamination level peaked at 100%. At the millimetre scale, the corresponding increases were more pronounced: 14.8% for the 20%–60% range and 18.3% from 60%–100%. At the microscale, arsenic concentrations rose by 15.36% and 14% for the same respective contamination increments.

At lower pumping rates (≤ 300 L/h), arsenic concentrations remain relatively constant across all scales and contamination levels, indicating the limited sensitivity of the system to these variations. In contrast, more pronounced variations occur at moderate to high pumping rates (>300 L/h), where increased flow enhances arsenic mobilisation and transport.

These results clearly reveal that the effect of contamination level becomes more significant as the spatial scale shrinks. Apparently, this behaviour is likely due to the higher surface-area-to-volume ratio at finer scales, which facilitates more pronounced interaction between the contaminated rock and the flowing water. However, limited contact time under elevated flow conditions reduces the system's ability to retain arsenic through sorption or precipitation. As a result, more arsenic is mobilised and flushed out at smaller scales, even under comparable levels of rock contamination. This highlights the coupled importance of scale, flow dynamics, and source contamination in predicting arsenic transport in porous media.

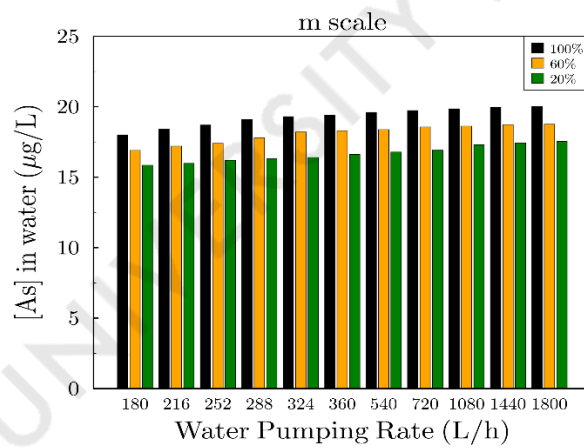
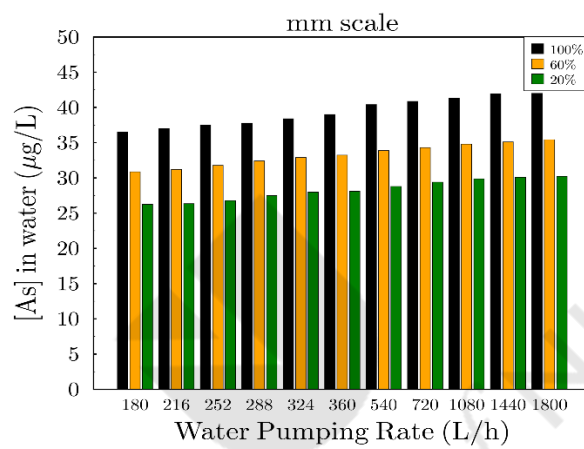
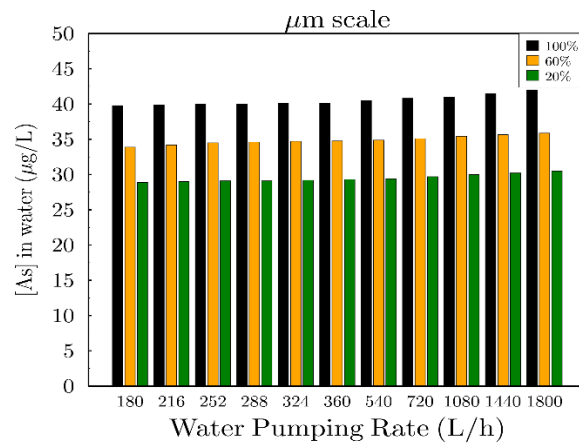


Figure 5.8: Influence of rock matrix and Arsenic contamination level on arsenic concentrations in pumped water, at three spatial scales of μm , mm and m.

5.2.3 Validation of Arsenic Release Through Desorption Analysis

To corroborate the trends observed in arsenic mobilisation across different pumping rates and spatial scales, a separate set of tests was conducted focusing specifically on desorption from the rock matrix.

These simulations were run under conditions of complete rock matrix contamination (100%) to capture the maximum potential for arsenic release. As shown in Figure 5.9, the desorbed arsenic concentrations strongly align with the trends previously discussed.

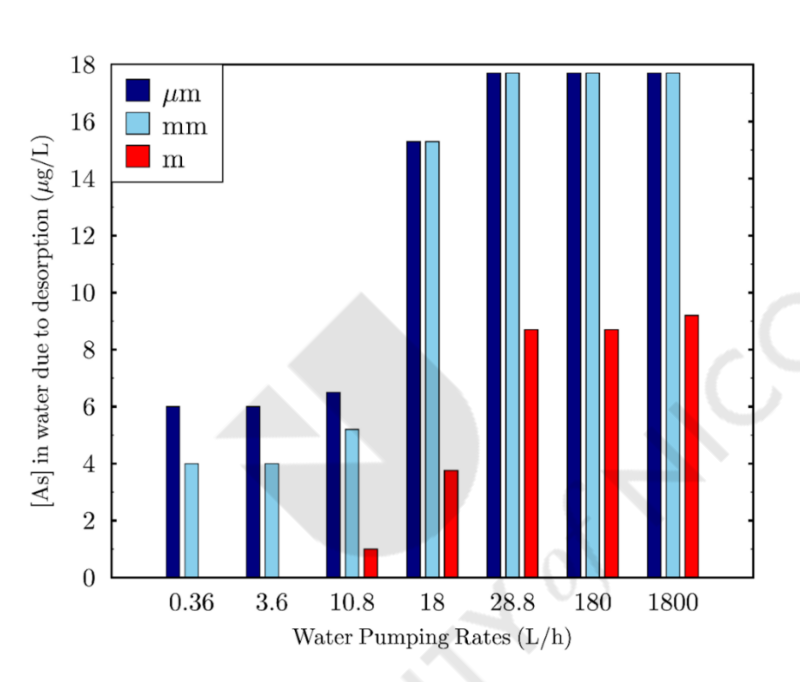


Figure 5.9: Arsenic released via desorption at varying pumping rates across spatial scales (µm, mm and m).

At the microscale, arsenic desorption increases rapidly with pumping rate, rising from 6 µg/L at 0.36 L/h to a peak of 17.7 µg/L at 28.8 L/h. A similar pattern is observed at the millimetre scale, with concentrations increasing from 4 µg/L to 17.7 µg/L across the same flow range. In contrast, desorption at the metre scale remains significantly depressed under slow flow (1 µg/L at 10.8 L/h), but increases steadily with higher water pumping, reaching a maximum of 9.2 µg/L at 1,800 L/h.

These results confirm that elevated pumping rates enhance arsenic mobilisation by reducing the contact time necessary for adsorption or precipitation processes to occur. The effect is more noticeable at smaller spatial scales, where the surface area-to-volume ratio is higher and the rock's capacity to retain arsenic is rather limited. Overall, the desorption data

provide a mechanistic validation of the observed increases in arsenic concentration in extracted groundwater, particularly under high flow and low-retention conditions.

Direct quantitative comparison of absolute arsenic concentrations is not appropriate in this case, due to differences in mineralogy, pore structure, contamination levels, and modelling frameworks. However, a qualitative comparison of transport behaviour is possible. In particular, the observed increase in arsenic mobilisation with increasing pumping rates is consistent with Garg and Singh (2016), Rukh et al. (2024), which report enhanced contaminant transport under higher flow conditions. Thus, even though numerical values differ, the underlying trend of flow-driven arsenic mobilisation is comparable.

5.2.4 Arsenic Removal Under Dilution Conditions

To assess the effectiveness of dilution in reducing arsenic concentrations in extracted groundwater, a series of long-term runs were conducted over a 50-year period at a moderate pumping rate of 500 L/h, assuming a low rock matrix contamination level (20%). Simulations were conducted at three spatial scales, beginning at the metre domain. As shown in Figure 5.10, the arsenic concentration in the produced water was 20 $\mu\text{g/L}$, rising slightly to 21.5 $\mu\text{g/L}$ during the first year, which was likely attributed to the early flushing of loosely bound arsenic on the mineral surfaces. Over time, however, the concentration steadily declined, reaching 16.3 $\mu\text{g/L}$ by year 20 and remaining constant thereafter, indicating that prolonged dilution and consistent flow facilitate the gradual removal of mobilisable arsenic from the system.

In a parallel test, where the arsenic concentration in the inflowing groundwater was reduced fivefold, the initial arsenic level in the extracted water was 17.54 $\mu\text{g/L}$ in the first year and dropped to 13.4 $\mu\text{g/L}$ by year 20, eventually stabilising at this amount after 50 years (Figure 5.10). This outcome further highlights the effectiveness of dilution, especially when combined with long-term pumping, in lowering arsenic concentrations even under minimal contamination conditions.

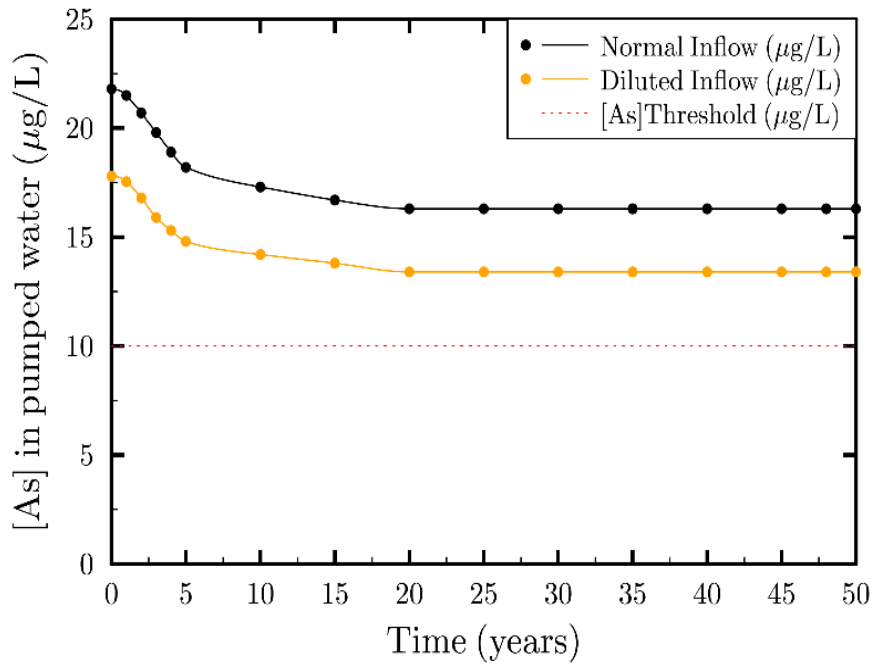


Figure 5.10: Long-term effect of dilution on arsenic concentrations in pumped water at 500 L/h, at the metre scale considering initial concentrations of $[As] = 20 \mu\text{g/L}$ under normal flow and $[As] = 4 \mu\text{g/L}$ and diluted flow conditions.

At both the millimetre and micrometre scales, a similar dilution-driven trend was observed. When the initial arsenic concentration in the groundwater was $20 \mu\text{g/L}$, the arsenic levels in the extracted water decreased from $35.2 \mu\text{g/L}$ to $31.3 \mu\text{g/L}$ over a 20-year simulation period (Figure 5.11). Examined in a parallel scenario where the inflowing groundwater was diluted to $4 \mu\text{g/L}$ of arsenic, the produced water concentration declined from $30.23 \mu\text{g/L}$ to $25.7 \mu\text{g/L}$, after 20 years. These results further demonstrate that dilution is effective even at finer spatial resolutions, although absolute concentrations remain higher due to the increased surface area and contact with arsenic-bearing material. Over time, the progressive flushing of mobile arsenic species drives the system toward a more stable and lower contamination state.

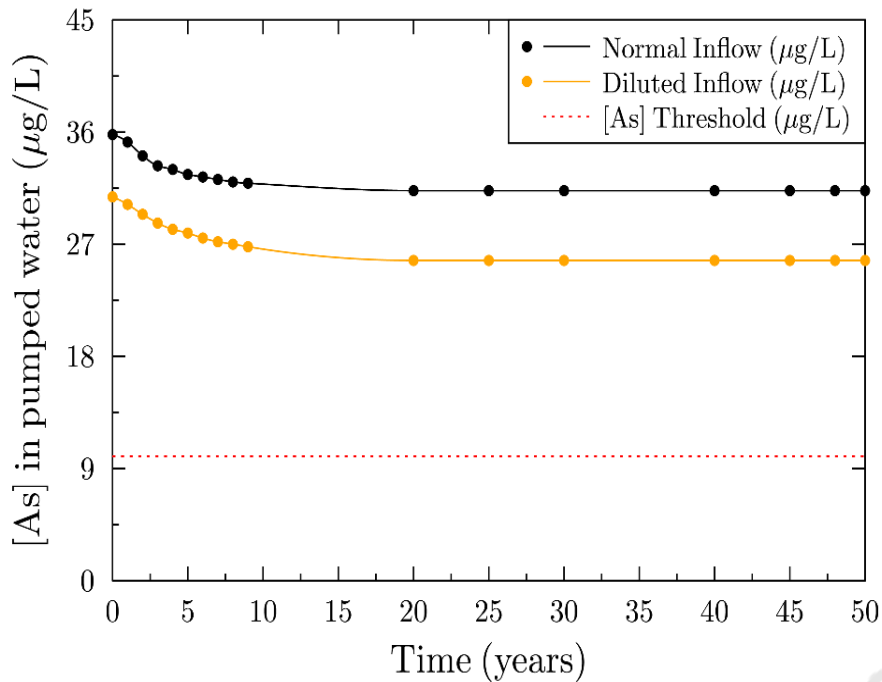


Figure 5.11: Long-term effect of dilution on arsenic concentrations in pumped water, at 500 L/h for the micrometre and the millimetre scales considering initial concentrations of $[As] = 20 \mu\text{g/L}$ under normal flow and $[As] = 4 \mu\text{g/L}$ and diluted flow conditions.

5.2.5 Arsenic Retention to Rock Matrix

This section investigates how pumping rate, spatial scale, rock matrix contamination level, and dilution conditions collectively influence arsenic retention in carbonate-hosted systems. Through a series of numerical simulations, the effects of flow rate on arsenic immobilisation across the pore (μm), core (mm), and reservoir (m) scales were examined, as well as the influence of matrix contamination levels on the retention capacity and flow sensitivity. The long-term behaviour of arsenic retention was also investigated under dilution scenarios. The analyses quantify how contact time, reactive surface area, and sorption-precipitation processes interact to control arsenic mass transfer between the aqueous and solid phases. Overall, the results provide a scale-aware understanding of how hydrodynamic and geochemical factors jointly govern the stability and persistence of arsenic within aquifer systems under variable extraction and recharge conditions.

5.2.6 Effect of Flow Rate on Arsenic Retained Across Scales

Figure 5.12 shows that the mass of arsenic retained in the rock matrix decreases systematically with stronger pumping rate across all spatial scales. At low pumping rates (< 20 L/h), retention is at its maximum, ranging between ~35 μg –39 μg depending on the spatial scale. As the pumping rate increases, $m(\text{As})$ declines sharply, stabilising beyond ~200 L/h. At this point, retention plateaus at ~12 μg –13 μg for the μm and the mm scales, and at ~24–25 μg for the metre scale.

This trend demonstrates that higher pumping rates reduce the contact time between groundwater and the mineral surfaces, limiting the re-adsorption and precipitation of arsenic released from the contaminated matrix, which immobilise arsenic. Conversely, at lower pumping rates, the longer residence time allows for more extensive interaction with calcite surfaces, enhancing adsorption and thereby increasing arsenic retention. The logarithmic fits ($R^2 = 0.90$) capture this inverse relationship, highlighting that the sensitivity of arsenic retention to pumping rate is greatest at the pore and core scales, while at the reservoir scale the effect is moderated.

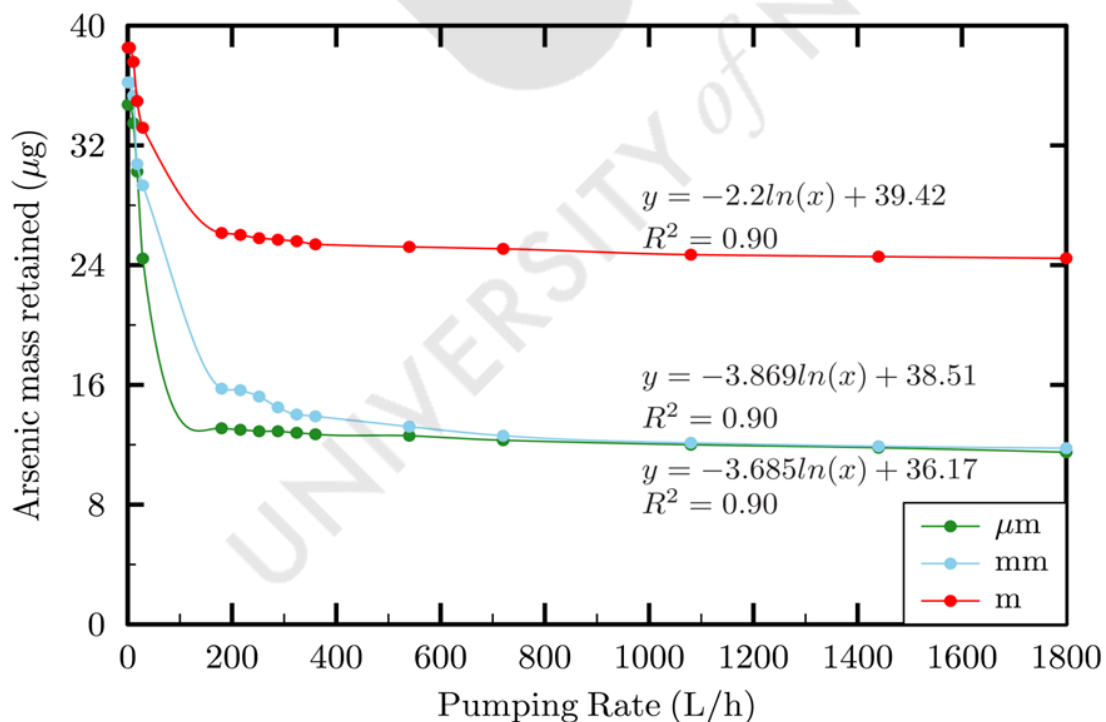


Figure 5.12: Arsenic mass retained to rock matrix (μg) as a function of the pumping rate for different porous media scales (μm , mm, m) for a rock matrix contamination set at 20%.

To confirm and emphasise these findings, an additional set of simulations was conducted under higher levels of rock matrix contamination, with arsenic incorporation elevated to 60%. Figure 5.13 shows that the mass of arsenic retained in the rock matrix again declines systematically with increasing pumping rate across all scales. At low water pumping rates (< 20 L/h), retention is highest—approximately $32\ \mu\text{g}$ – $36\ \mu\text{g}$ depending on the scale. As pumping rates rise, the mass of Arsenic ($m(\text{As})$) drops sharply and then levels off beyond ~ 150 – 200 L/h. At the high-flow plateau, retention is $\sim 7\ \mu\text{g}$ – $8\ \mu\text{g}$ for the μm and mm domains and ~ 23 – $24\ \mu\text{g}$ for the metre-scale. At higher pumping rates (≥ 500 L/h), the retention values at the micrometre and the millimetre scales converge, reflecting a transition from reaction-controlled to transport-controlled behaviour. Under these conditions, reduced residence time limits adsorption and precipitation processes, diminishing the influence of surface area and pore-scale heterogeneity. As a result, arsenic transport becomes dominated by advective flow, leading to similar retention behaviour across the smaller scales.

The logarithmic pattern signifies that arsenic retention depends on the flow rate and exhibits steeper slopes at the micrometre and the millimetre scales, indicating stronger sensitivity to pumping there, while the metre scale exhibits a more moderate decline and maintains the highest residual retention.

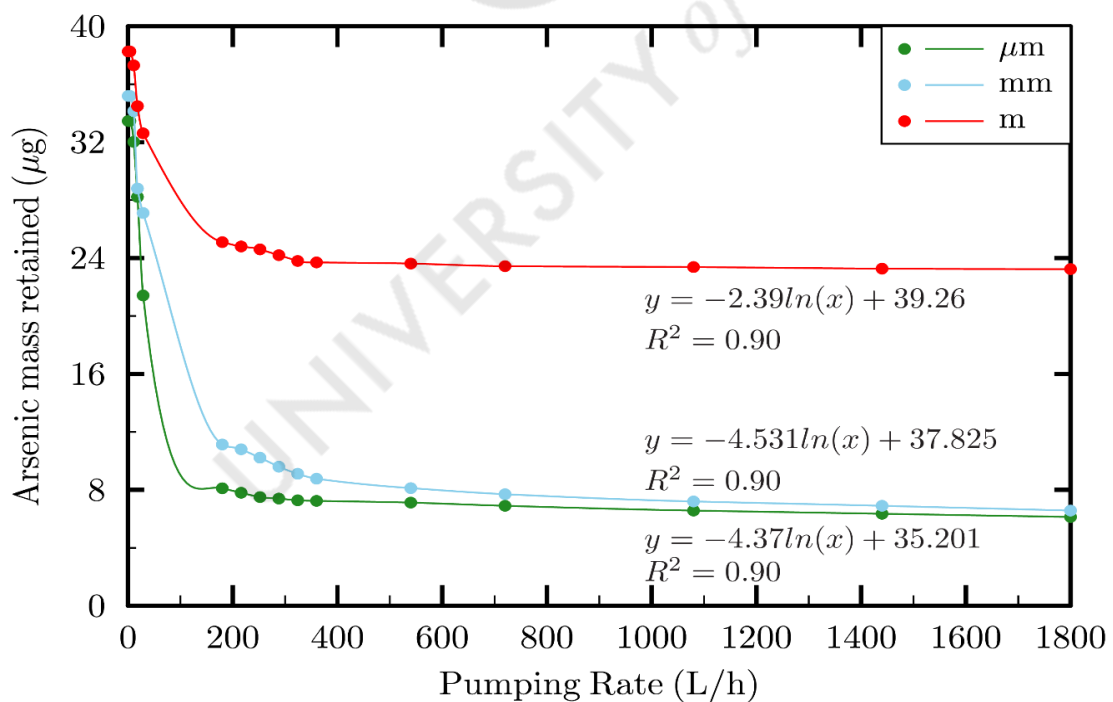


Figure 5.13: Arsenic mass retained to rock matrix (μg) as a function of the pumping rate for different porous media scales (μm , mm , m) where rock matrix contamination is set at 60%.

5.2.7 Influence of the Rock Matrix Contamination Level

Across all the spatial scales, the mass of arsenic retained decreases as pumping rises from 180 L/h to 1,800 L/h. At the μm scale, Arsenic retention falls from 13.2 μg (rock contamination 20%), and 7.9 μg (rock contamination 60%) at 180 L/h to 11.8 μg and 6.3 μg at 1,800, L/h respectively. At the millimetre scale, the drop was more pronounced, that is, from ~ 15.8 μg (20%) and 10.1 μg (60%) to ~ 11.5 μg and 6.4 μg , correspondingly. The metre spatial scale is least sensitive, decreasing the Arsenic contamination from ~ 25.8 μg (20%) and 24.7 μg (60%) to ~ 24.1 μg and 23.7 μg ($\approx 7\%$ and 4%). This trend is consistent with residence-time control where higher pumping shortens contact time, limiting sorption/co-precipitation and thus retention (Figure 5.14).



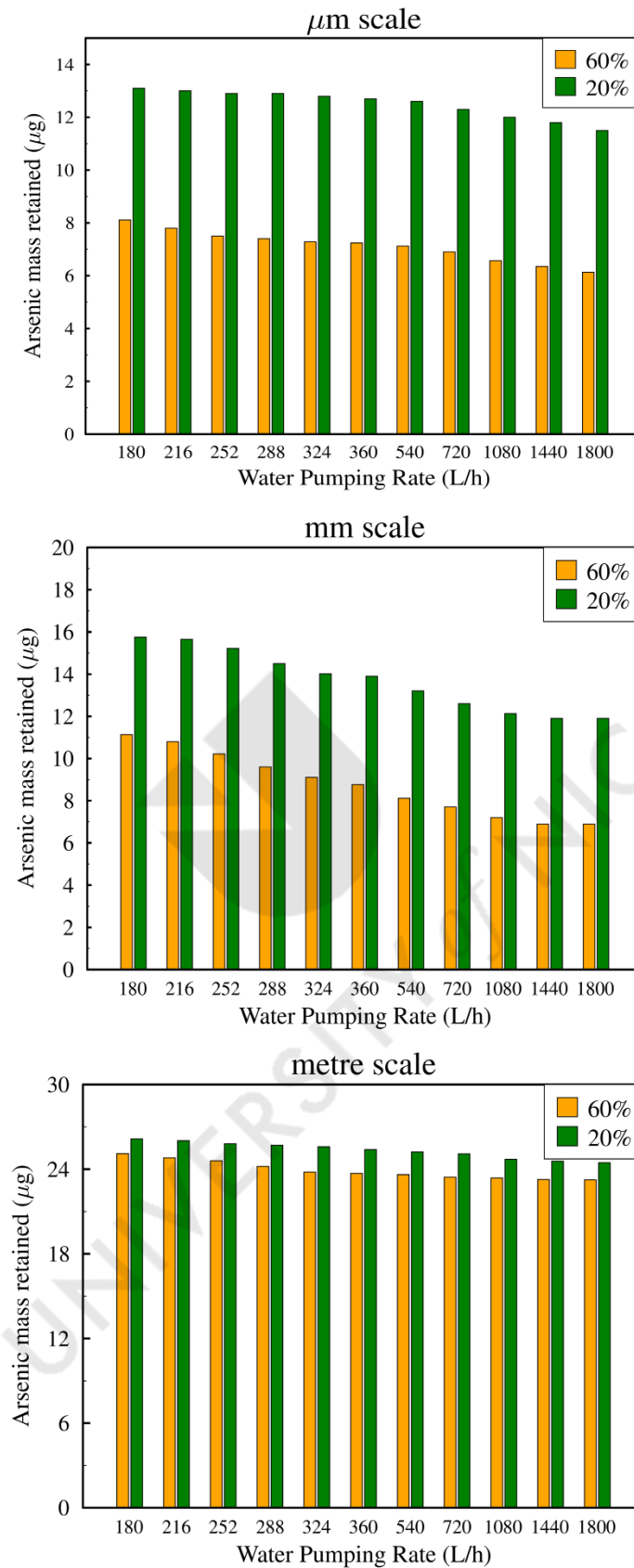


Figure 5.14: Arsenic mass retained (μg) at three spatial scales as a function of pumping rate (180–1,800 L/h), for two initial contamination levels (20% and 60%).

Figure 5.14 shows that absolute arsenic retention increases with domain size. At 180 L/h, the metre-scale domain retains $\sim 25.8 \mu\text{g}$ decreasing to $4.1 \mu\text{g}$ at 1,800 L/h, the millimetre-scale retains $15.8 \mu\text{g}$ decreasing to $11.5 \mu\text{g}$, and the micrometre-scale retains $13.2 \mu\text{g}$ decreasing to $11.8 \mu\text{g}$ over the same flow range. This order reflects the fact that larger domains contain greater reactive volume and pore surface area, which in turn provide more sites for sorption and precipitation, thereby enhancing the overall capacity for arsenic retention.

The results demonstrate that arsenic retention is jointly controlled by scale, contamination level, and pumping rate. While smaller domains exhibit greater sensitivity to flow conditions, larger aquifer-scale systems function as more stable arsenic sinks with only minor declines in retention under increased pumping. Together, these findings highlight the importance of adopting a scale-aware perspective when predicting arsenic fate and assessing groundwater quality under different extraction scenarios.

5.2.8 Arsenic Retention Under Dilution Conditions

As demonstrated in Figure 5.15, for over 50 years, both scenarios show a rapid early increase in retained Arsenic during the first ~10–12 years, then progress to at a slow pace to a plateau.

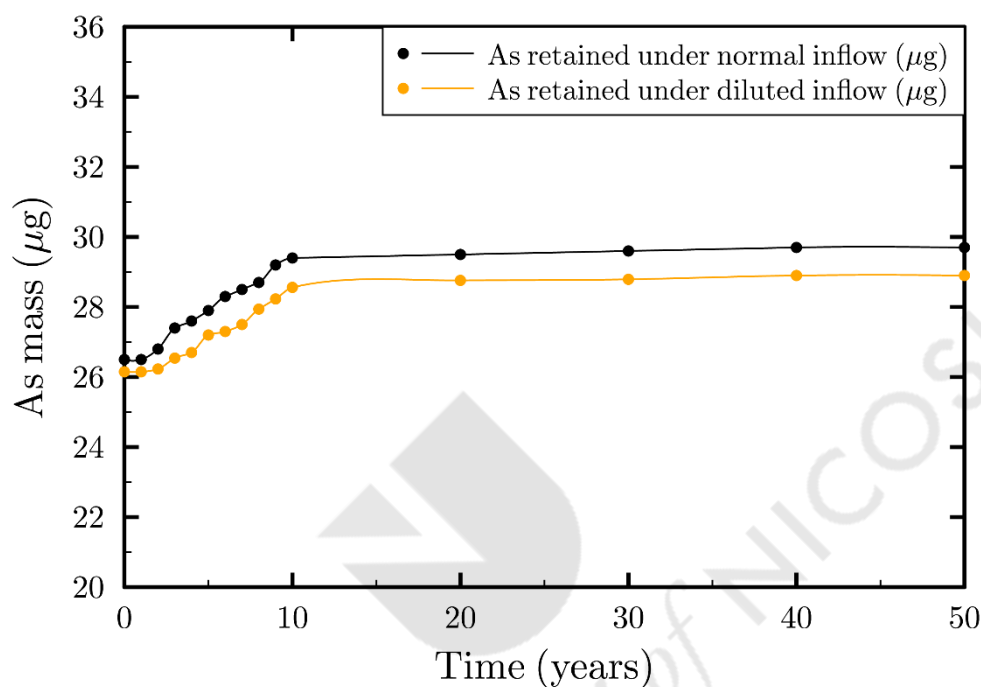


Figure 5.15: Long-term effect of dilution on arsenic mass retained at the metre scale under 20% rock-matrix contamination.

In the normal-inflow case, the retained mass of arsenic rises from ~26–27 µg to ~29.3–29.4 µg after 50 years, whereas in the diluted-inflow case, the retained mass of arsenic climbs from ~26 µg to ~28.8–28.9 µg. Thus, dilution lowers the retained inventory by only ~0.4–0.6 µg (≈ 1 –2%) at any given time, despite a 5× lower inflowing concentration. This indicates that, at 20% matrix contamination, solid-phase capacity and carbonate buffering dominate the long-term mass balance: the rock continues to sorb and co-precipitate arsenic until sites approach quasi-equilibrium. Concurrently, the difference in inflow concentration mainly shifts asymptotically downwards rather than changing the overall trajectory (Figure 5.15).

Practically, dilution effectively lowers aqueous concentrations but only modestly reduces the accumulated solid phase over decadal timescales. Apparently for dilution to significantly

deplete the solid inventory it needs to be combined with strategies that increase desorption/dissolution such as longer residence times and geochemical perturbation, otherwise the system remains a resilient long-term storage reservoir.

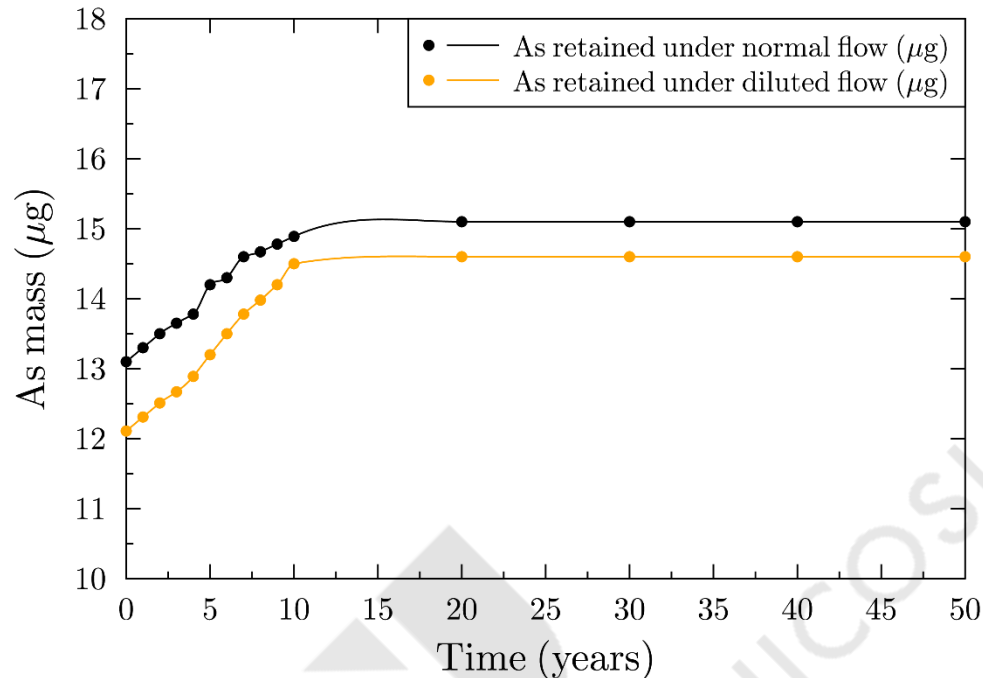


Figure 5.16: Long-term effect of dilution on arsenic mass retained at the μm and mm scale under 20% rock-matrix contamination.

Over the 50-year simulation time window, the mass of arsenic retained increases rapidly during the first decade and then approaches a steady state, indicating that sorption sites become progressively saturated. Under normal flow conditions, retention rises from $\sim 13 \mu\text{g}$ at year 0 to $\sim 15.2 \mu\text{g}$ by years 10–15, after which it remains essentially constant. Under diluted flow, the same pattern is observed but with consistently lower values: $\sim 12.1 \mu\text{g}$ initially, levelling off near $\sim 14.6\text{--}14.7 \mu\text{g}$ (Figure 5.16). Thus, normal flow retains about 0.4–0.6 μg more arsenic than diluted transport throughout most of the record. Indeed, a small but persistent advantage that suggests either higher advective delivery of arsenic to reactive surfaces or reduced competitive effects under the undiluted regime. The asymptotic behaviour in both cases implies that, beyond ~ 10 years, additional exposure time does not materially increase retained mass, consistent with near-equilibrium sorption/precipitation kinetics and a finite capacity of the solid phase to immobilise arsenic.

5.2.9 Numerical Robustness and Model Verification

To assess the numerical robustness of the simulations, a grid sensitivity analysis was conducted. Simulations for the meter-scale domain at 100% contamination were repeated using a refined spatial discretization, increasing the grid resolution from 100×100 to 200×200 cells while keeping all other parameters unchanged. Across all pumping rates, the outlet response expressed as normalized concentration (C/C_0) exhibited an average change of approximately 1.5%, with a maximum deviation within the 2–5% range. These results indicate that the reported trends are not sensitive to spatial discretization and confirm the lend credibility to the modeling framework (Table 5.6).

Table 5.6: Grid sensitivity analysis of normalized outlet arsenic concentration (C/C_0) for meter-scale simulations.

Pumping rate (L/h)	Grid size (cell)	C/C_0 (20%)	C/C_0 (60%)	C/C_0 (100%)
0.36	100 × 100	0.86	0.94	1.00
	200 × 200	0.89	0.89	0.99
	Relative difference* (%)	2.6	4.8	1.0
1,800	100 × 100	4.30	4.70	5.00
	200 × 200	4.40	4.71	4.95
	Relative difference* (%)	0.39	0.31	1.0

*Relative difference (%) is calculated as the absolute percentage change in C/C_0 between the 100×100 and 200×200 grid resolutions.

To evaluate the numerical robustness of the simulated arsenic retention behaviour, selected scenarios were independently reproduced using the reactive transport code MIN3P and compared against CrunchFlow results for contamination levels of 20% and 60%. As shown in Figure 5.17, the comparison focuses on the total mass of arsenic retained in the rock matrix as a function of the pumping rate across three spatial scales (μm , mm, and m). For both contamination levels, the two codes exhibit highly consistent retention patterns over the

full pumping range (≈ 0 – $1,800$ L/h). At low pumping rates (< 50 – 100 L/h), both codes predict strong retention, with retained arsenic masses of approximately 30 – 36 μg at the micrometre and the millimetre scales and 35 – 39 μg at the metre scale. As pumping rates mount, both codes capture a pronounced decline in retained mass, followed by convergence toward stable high-flow plateaus beyond ~ 300 – 500 L/h. At high pumping rates ($> 1,000$ L/h), retained arsenic stabilises at about 11 – 13 μg (μm), 13 – 16 μg (mm), and 22 – 25 μg (m), with nearly identical plateau behaviour in both numerical frameworks.

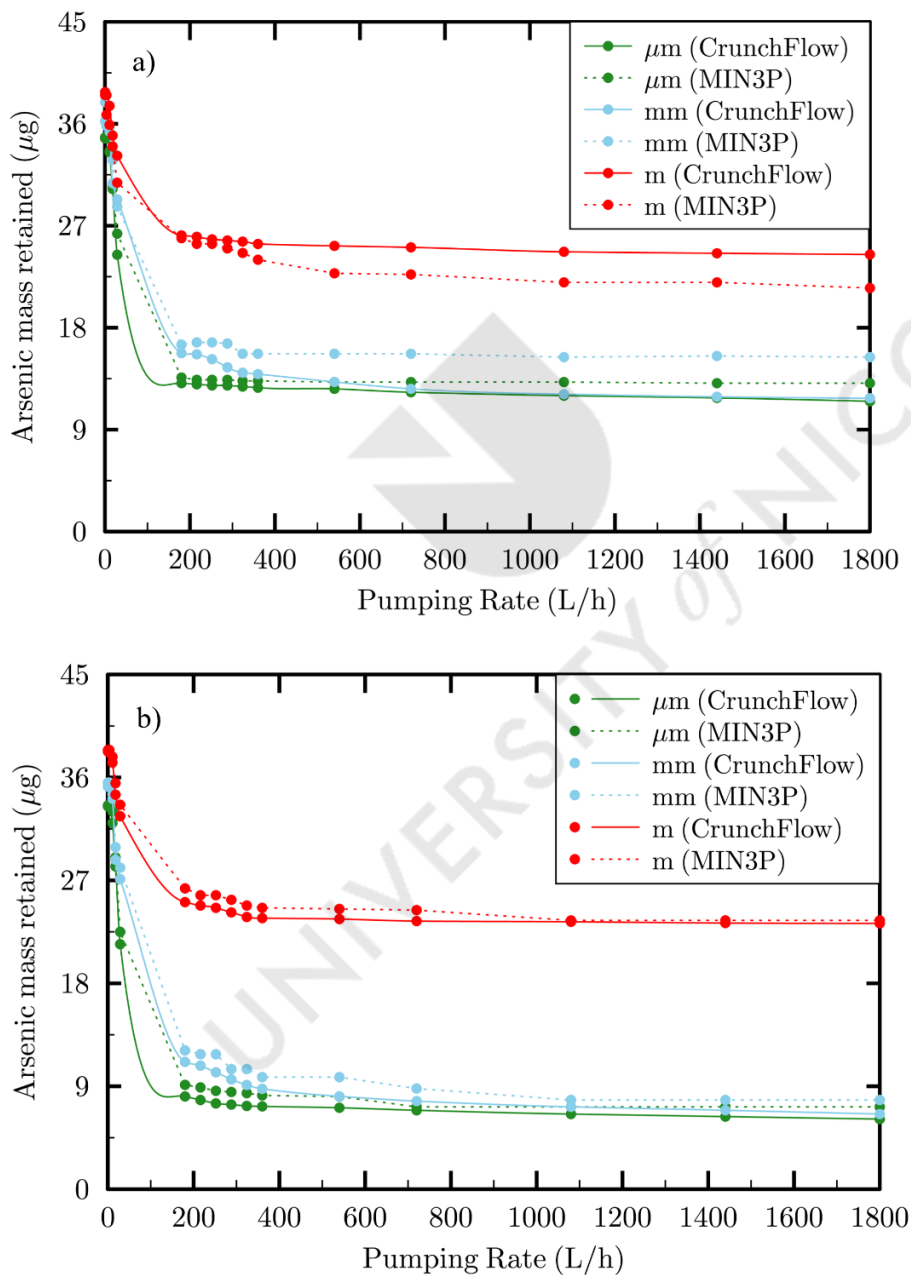


Figure 5.17: CrunchFlow and MIN3P comparison of scale-dependent arsenic retention versus pumping rate for: a) 20% and b) 60% rock-matrix contamination levels.

Quantitative differences between CrunchFlow and MIN3P remain limited and systematic across all conditions examined. For the 20% contamination case, deviations in retained mass between the two codes are generally within 1–2 μg at the μm and mm scales and within 2–3 μg at the metre scale, corresponding to relative differences of approximately 5–10% across most pumping rates. Similar magnitudes of deviation are observed for the 60% contamination case, with MIN3P typically predicting slightly higher retention at the μm and mm scales and slightly lower retention at the metre scale compared to CrunchFlow. Importantly, these differences are smooth across pumping rate(s) and do not lead to curve crossings, changes in slope, or reordering of scale-dependent retention. In all cases, both codes consistently predict higher retention at larger spatial scales and identify pumping-rate-controlled residence time as the dominant control on arsenic immobilisation. The close quantitative agreement across two independent reactive transport codes and across multiple contamination levels demonstrates that the retention trends and scale dependence reported in this study are robust and not artefacts of a specific numerical implementation offering an independent way for cross-verification of the findings.

5.3 Methane Release from the Nord Stream Pipeline System

The numerical simulations effectively reproduced the transient multiphase flow behaviour of methane following the rupture of the Nord Stream 1 and Nord Stream 2 pipelines in the Baltic Sea. Using the OLGA multiphase flow simulator, the model captured the rapid depressurization of both pipelines—from initial pressures of 175 bar (NS1) and 105 bar (NS2)—as methane escaped through the severed sections into the surrounding seawater. Results indicated that most of the methane discharge occurred within the first 48 hours, with flow rates decaying exponentially as internal pressure diminished, and that both pipelines reached hydrostatic equilibrium at approximately 9 bar after about one week. Integration of the gas flow rates over time yielded an estimated total release of around 477 kilotonnes ($\pm 6\%$), corresponding to roughly 789 million standard cubic metres (mscm) of methane which is in strong agreement with independent satellite and atmospheric measurements. Spatial pressure profiles revealed asymmetrical depressurisation near the leak sites close to the Bornholm Island, while seawater inflow accelerated pressure stabilisation and limited the total release time duration. Complementary COMSOL Multiphysics simulations of the near-field bubble plumes confirmed that gas dissolution into seawater was minimal compared to direct atmospheric venting. Collectively, these results demonstrate that the Nord Stream incident represents one of the largest anthropogenic methane emissions ever documented and

validate the use of OLGA and COMSOL as reliable coupled tools for modelling large-scale, transient multiphase flow phenomena under variable marine conditions.



CHAPTER 6: CONCLUSIONS

UNIVERSITY of NCOSIA

6 Conclusions

6.1 Concluding Remarks

This thesis investigated fluid transport, pore structure, and reactive processes across multiple spatial scales, integrating digital rock physics, reactive transport modelling, and multiphase flow simulations. The work combined micro-CT imaging, numerical modelling, and geochemical simulations to advance the prevailing understanding of flow and contaminant dynamics in porous carbonate and sandstone systems of Cyprus. The principal findings are summarised below:

- Digital rock characterisation using Avizo 2019.1 successfully quantified the microstructural and petrophysical properties of sandstone and carbonate samples obtained from onshore Cyprus. The micro-CT reconstructions enabled the direct measurement of porosity and permeability, revealing that porosity values ranged between 5% and 22%, while permeability varied from 0.03 mD to 3.188 mD. Results confirmed that high porosity does not necessarily imply high permeability due to poor pore connectivity and narrow throat apertures, emphasising the role of pore geometry in controlling porous media fluid flow.
- The porosity-permeability correlations derived from digital rock analysis were used to develop a MATLAB-based algorithm capable of generating synthetic permeability maps from 2D thin sections. This approach provided a reproducible digital workflow for translating image-based data into numerical input for reactive transport simulations, thus bridging pore-scale characterisation and continuum-scale modelling.
- The reactive transport simulations revealed that arsenic concentrations in groundwater increase with flow rate, primarily owing to smaller residence time and reduced solid-liquid interaction. At a high flow rate of 1,800 L/h, aqueous arsenic concentrations exceeded 30 $\mu\text{g/L}$, while at lower rates (0.36 L/h), concentrations remained below 18 $\mu\text{g/L}$. This behaviour is consistent with enhanced arsenic flushing at higher pumping rates and increased retention under low-flow conditions.
- Scale effects were clearly observed across the micrometre-, millimetre-, and metre-scale models. Larger domains exhibited lower arsenic concentrations due to greater reactive surface area and more efficient sorption, whereas smaller domains responded rapidly to flow perturbations, confirming the scale dependency of reactive transport in carbonate aquifers.

- Contamination level strongly influenced arsenic mobility. Simulations with 100% substitution of calcite by $\text{Ca}_3(\text{AsO}_4)_2$ produced the highest aqueous concentrations, reaching $\sim 30 \mu\text{g/L}$ at the pore scale, $\sim 22 \mu\text{g/L}$ at the millimetre scale, and $\sim 17\text{--}18 \mu\text{g/L}$ at the metre scale at high pumping rates. In contrast, 20% contamination resulted in much lower concentrations, typically $\sim 10\text{--}12 \mu\text{g/L}$ (μm), $\sim 7\text{--}9 \mu\text{g/L}$ (mm), and $\sim 3\text{--}5 \mu\text{g/L}$ (m). Higher contamination also reduced solid-phase retention, which declined from $\sim 35\text{--}40 \mu\text{g}$ at 20% contamination to $\sim 20\text{--}25 \mu\text{g}$ at 100% contamination, demonstrating that the initial geochemical state and contamination history directly control long-term arsenic release and aquifer quality. Contamination levels strongly influenced arsenic mobility.
- Long-term dilution simulations (500 L/h over 50 years) showed a gradual decline in aqueous arsenic concentrations, with values decreasing by $\sim 20\text{--}25\%$ within the first 20 years before stabilising. Despite this reduction, solid-phase arsenic dropped by only $\sim 1\text{--}2\%$, indicating that most arsenic remained adsorbed to carbonate mineral surfaces. These results demonstrate that carbonate aquifers act as persistent arsenic reservoirs, with dilution lowering aqueous concentrations but having limited impact on long-term arsenic retention.
- Geochemical analysis confirmed that arsenic mobility is governed by surface complexation, desorption, and co-precipitation with calcite. Under circumneutral to alkaline conditions ($\text{pH} \sim 7.5\text{--}8.5$), arsenate was preferentially retained by calcite through surface complexation and limited co-precipitation. However, during sustained pumping, reduced residence times led to progressive desorption, increasing aqueous arsenic concentrations by $\sim 10\text{--}15\%$ relative to low-flow conditions. These results identify desorption from calcite surfaces as the dominant mobilisation mechanism under prolonged hydraulic stress, while co-precipitation acts as a secondary, flow-limited sink.
- Finally, the Nord Stream side project validated the modelling methodology applied in this work. Transient multiphase simulations using OLGA and COMSOL Multiphysics estimated a total methane release of $\sim 478 \text{ kt}$, while showing that no more than $\sim 4\%$ of the released methane dissolved in the water column, with the vast majority reaching the atmosphere.

In summary, this research establishes a quantitative and scalable methodology for linking rock microstructure, flow behaviour, and geochemical reactivity. By combining digital rock

physics, reactive transport modelling, and advanced computational techniques, the thesis contributes to a deeper understanding of contaminant mobility in carbonate aquifers and strengthens the predictive basis for groundwater quality assessment and sustainable resource management.

6.2 Future Research Directions

The findings of this thesis present multiple opportunities for further research, particularly in expanding the integration of image-based rock characterisation, synthetic pore structure modelling, and reactive transport simulation. While this work established strong connections between pore geometry and arsenic mobility, additional developments could refine its scope and broaden its applicability in both the environmental and energy realms.

In the field of digital rock physics (DRP), future research should focus on incorporating a wider variety of lithologies and improving segmentation accuracy using AI-assisted classification techniques. Expanding synthetic sediment modelling to include heterogeneous grain distributions and cementation effects would allow for more realistic representations of natural reservoir and aquifer materials. Additionally, larger-scale micro-CT datasets could be processed using automated workflows to improve statistical robustness across lithologies.

To advance both the scientific understanding and practical groundwater management, future investigations should broaden the methodological approaches, deepen the geochemical and biological complexity, coupled with experimental validation, and translate scientific insights into applied field management strategies.

From a methodological standpoint, future work should extend the numerical approaches developed here enabling more rigorous simulations. The current study employed two-dimensional domains that provided valuable insights into the coupled effects of flow and chemistry. However, carbonate aquifers are three-dimensional in nature, with anisotropy, fractures, and preferential pathways that cannot be fully captured in 2D models. Developing 3D representations would provide a more realistic picture of aquifer heterogeneity and contaminant transport. Similarly, future modelling efforts could integrate geomechanically changes such as compaction, fracturing, and porosity-permeability correlation. These processes may alter flow patterns and sorption dynamics over time, thereby reshaping the retention capacity of aquifers. Another promising direction is the explicit consideration of multi-contaminant systems, since real aquifers often contain competing oxyanions such as

phosphate, bicarbonate, and silicate that influence arsenic mobility. High-performance computing, including GPU-enabled simulations, could also extend the spatial and temporal reach of these models, rendering them more applicable to field-scale predictions and long-term water management scenarios.

At the geochemical and biological level, further work is needed to explore the dynamic conditions that regulate arsenic speciation and retention. The present study emphasised surface complexation and precipitation with calcite, but aquifer chemistry is rarely static. Seasonal recharge, seawater intrusion, or agricultural activity may induce temporal fluctuations in pH and redox potential that strongly affect arsenic stability. In addition, microbial communities are known to mediate arsenic oxidation and reduction, yet their role in carbonate aquifers remains largely unexplored. Incorporating microbial kinetics into reactive transport frameworks would provide a more complete and realistic representation of arsenic transformations. Mineralogical diversity also deserves greater attention. Although calcite dominates in many carbonate aquifers, the presence of dolomite, clays, or iron oxides could substantially alter sorption equilibria. Expanding the scope of simulations to mixed mineralogies would enhance the generality of results and make them applicable to aquifers with more complex compositions.

Experimental and field validation represent another essential frontier. Modelling alone, no matter how advanced, requires calibration and verification against empirical data. Pore-scale visualisation techniques such as microfluidics or synchrotron imaging could directly observe arsenic adsorption and precipitation at mineral surfaces, providing valuable evidence of the modelling mechanisms. Core-flooding experiments using intact carbonate samples under controlled flow and chemistry would generate new or supply from existing critical datasets for upscaling simulations. At the field scale, long-term monitoring of Cypriot aquifers, including pumping tests and tracer experiments, would establish the connection between numerical predictions and real-world contaminant dynamics. By integrating laboratory, field, and computational approaches, future research could generate a robust and multi-scale framework for predicting the fate of arsenic.

The Nord Stream side investigation served as a valuable computational case study for simulating multiphase methane release. A potential extension of this work could involve refining temporal and spatial resolution in OLGA-COMSOL coupling to capture rapid transient effects during gas leakage events. Applying this framework to other subsurface

leakage scenarios, including the leak of CO₂ or aquifer gas intrusion, could expand its relevance to environmental risk assessments and infrastructure monitoring.

Collectively, future research should aim for greater integration of pore-scale physics, microbial processes, and real-world geological complexity, ensuring that numerical simulations continue to evolve as powerful tools for both hydrogeological interpretation and contaminant risk prediction.



References

- Aeoliki Ltd, 2009. Institutional framework and decision-making practices for water management in Cyprus: Towards the development of a strategy for aquifer protection and management in Pegeia, Paphos. Cyprus: INECO
- World Health Organization (WHO). *Arsenic* [Online]. Available: <https://www.who.int/news-room/fact-sheets/detail/arsenic> [Accessed 5/8/2025].
- Ahmed, K. M., Bhattacharya, P., Hasan, M., Alam, S. M. M., Bhuiyan, A., Imam, B., Khan, A. & Sracek, O. 2004. Arsenic Enrichment in Groundwater of the Alluvial Aquifers in Bangladesh: An Overview. *Applied Geochemistry*, 19, 181-200.
- Ahr, M. 2008. *Geology of Carbonate Reservoirs: The Identification, Description, and Characterization of Hydrocarbon Reservoirs in Carbonate Rocks*, Hoboken, New Jersey John Wiley & Sons.
- Al Ibrahim, M., Kerimov, A., Mukerji, T. & Mavko, G. 2018. Digital rocks with irregularly shaped grains: A simulator tool for computational rock physics. *Physical Review E*, 75.
- Andrä, H., Combaret, N., Dvorkin, J., Glatt, E., Han, J., Kabel, M., Keehm, Y., Krzikalla, F., Lee, M., Madonna, C., Marsh, M., Mukerji, T., Saenger, E. H., Sain, R., Saxena, N., Ricker, S., Wiegmann, A. & Zhan, X. 2013a. Digital rock physics benchmarks—Part I: Imaging and segmentation. *Computers & Geosciences*, 50, 25-32.
- Andrä, H., Combaret, N., Dvorkin, J., Glatt, E., Han, J., Kabel, M., Keehm, Y., Krzikalla, F., Lee, M., Madonna, C., Marsh, M., Mukerji, T., Saenger, E. H., Sain, R., Saxena, N., Ricker, S., Wiegmann, A. & Zhan, X. 2013b. Digital rock physics benchmarks—part II: Computing effective properties. *Computers & Geosciences*, 50, 33-43.
- Angelakis, A. & Gikas, P. 2014. Water reuse: Overview of current practices and trends in the world with emphasis in EU states. *Water Utility* 6, 67-78.
- Arns, C., Bauget, F., Limaye, A., Sakellariou, A., Senden, T., Sheppard, A., Sok, R., Pinczewski, V., Bakke, S. & Berge, L. I. 2005. Pore Scale Characterization of Carbonates Using X-Ray Microtomography. *Society of Petroleum Engineers*, 10, 475-484.
- Arns, C. H., Knackstedt, M. A., Pinczewski, W. V. & Martys, N. S. 2004. Virtual permeametry on microtomographic images. *Journal of Petroleum Science and Engineering*, 45, 41-46.
- Arora, B., Şengör, S. S., Spycher, N. F., Steefel, C. I., Yabusaki, S. B., Fang, Y. & Molins, S. 2015. A reactive transport benchmark on heavy metal cycling in lake sediments. *Computational Geosciences*, 19, 613-633.
- Bear, J. & Cheng, A. 2010. *Modeling Groundwater Flow and Contaminant Transport*, United States Geological Survey.

- Benedetto, F., Costagliola, P., Benvenuti, M., Lattanzi, P., Romanelli, M. & Tanelli, G. 2006. Arsenic incorporation in natural calcite lattice: Evidence from electron spin echo spectroscopy. *Earth and Planetary Science Letters*, 246, 458-465.
- Berg, M., Stengel C Fau - Pham, T. K. T., Pham Tk Fau - Pham, H. V., Pham Hv Fau - Sampson, M. L., Sampson Ml Fau - Leng, M., Leng M Fau - Samreth, S., Samreth S Fau - Fredericks, D. & Fredericks, D. 2007. Magnitude of arsenic pollution in the Mekong and Red River Deltas: Cambodia and Vietnam. *Science Environmental Journal* 10.1016/j.scitotenv.2006.09.010
- Bhattacharya, P., Welch, A. H., Stollenwerk, K. G., Mclaughlin, M. J., Bundschuh, J. & Panaullah, G. 2007. Arsenic in the environment: Biology and Chemistry. *Science of The Total Environment*, 379, 109-120.
- Bia, G., García, M. G., Rueda, E. S., Mors, R. A., Mlewski, E. C., Gomez, F. J. & Borgnino, L. 2021. Arsenic in natural carbonates: The role of the biogeochemical conditions in its solid speciation. *Chemical Geology*, 583, 120477.
- Blatt Harvey, G. V. M., Raymond C. Murray 1980. *Origin of Sedimentary Rocks*, Englewood Cliffs, New Jersey, USA, Prentice Hall.
- Blunt, M. J. 2017. *Multiphase Flow in Permeable Media: A Pore-Scale Perspective*, Cambridge, Cambridge University Press.
- Boggs, J. S. 2009. *Petrology of Sedimentary Rocks*, Cambridge, Cambridge University Press.
- Bundschuh, J., Litter, M. I., Parvez, F., Román-Ross, G., Nicolli, H. B., Jean, J.-S., Liu, C.-W., López, D., Armienta, M. A., Guilherme, L. R. G., Cuevas, A. G., Cornejo, L., Cumbal, L. & Toujaguez, R. 2012. One century of arsenic exposure in Latin America: A review of history and occurrence from 14 countries. *Science of The Total Environment*, 429, 2-35.
- Cai, D., Kong, S., Shao, Y., Liu, J., Liu, R., Wei, X., Bai, B., Werner, D., Gao, X. & Li, C. 2022. Mobilization of arsenic from As-containing iron minerals under irrigation: Effects of exogenous substances, redox condition, and intermittent flow. *Journal of Hazardous Materials*, 440, 129736.
- Chen, L., He, A., Zhao, J.-L., Kang, Q., Li, Z.-Y., Carmeliet, J., Shikazono, N. & Tao, W.-Q. 2022. Pore-scale modeling of complex transport phenomena in porous media. *Progress in Energy and Combustion Science*, 88, 100968.
- Choquette, P. W. & Pray, L. C. 1970. Geologic Nomenclature and Classification of Porosity in Sedimentary Carbonates1. *AAPG Bulletin*, 54, 207-250.
- Chou, P.-I., Wu, X., Gao, Z., Zhu, Y. & Jun, Y.-S. 2025. Bicarbonate Concentrations Affect Arsenic Release from Arsenopyrite and Nanoscale Iron (III) (Hydr)oxide Formation: Importance of Unconfined Aquifer Carbonate Chemistry. *Environmental Science: Nano*, 12.
- Christodoulidou, M., Charalambous, C., Aletrari, M., Kanari, P., Petronda, A. & Ward, N. 2012. Arsenic concentrations in groundwaters of Cyprus. *Journal of Hydrology*, s 468–469, 94–100.

- Chung, J.-Y., Yu, S.-D. & Hong, Y.-S. 2014. Environmental Source of Arsenic Exposure. *Journal of Preventive Medicine and Public Health*, 47, 253-257.
- Cnudde, V. & Boone, M. 2013. High-resolution X-ray computed tomography in geosciences: A review of the current technology and applications. *Earth-Science Reviews*, 123, 1–17.
- Dar, Q. U. Z. Z., Pu, R., Baiyegunhi, C., Shabeer, G., Ali, R. I., Ashraf, U., Sajid, Z. & Mehmood, M. 2022. The impact of diagenesis on the reservoir quality of the early Cretaceous Lower Goru sandstones in the Lower Indus Basin, Pakistan. *Journal of Petroleum Exploration and Production Technology*, 12, 1437-1452.
- Degnan, J. R., Lindsey, B. D., Levitt, J. P. & Szabo, Z. 2020. The relation of geogenic contaminants to groundwater age, aquifer hydrologic position, water type, and redox conditions in Atlantic and Gulf Coastal Plain aquifers, eastern and south-central USA. *Science of The Total Environment*, 723, 137835.
- Dillon, P., Stuyfzand, P., Grischek, T., Lluria, M., Pyne, D., Jain, R., Bear, J., Schwarz, J., Weiping, W., Escalante, E., Stefan, C., Pettenati, M., Van Der Gun, J., Sprenger, C., Massmann, G., Scanlon, B., Xanke, J., Jokela, P., Zheng, Y. & Sapiano, M. 2019. Sixty years of global progress in managed aquifer recharge. *Hydrogeology*, 10.1007/s10040-018-1841-z.
- Dinnebier, R. E. & Billinge, S. J. L. 2008. *Powder Diffraction: Theory and Practice*, Royal Society of Chemistry.
- Dixit, S. & Hering, J. G. 2003. Comparison of Arsenic(V) and Arsenic(III) Sorption onto Iron Oxide Minerals: Implications for Arsenic Mobility. *Environmental Science & Technology*, 37, 4182-4189.
- Dybbs, A. & Edwards, R. V. 1984. A New Look at Porous Media Fluid Mechanics — Darcy to Turbulent. *Journal of Petroleum Science and Engineering*, 16, 1–3.
- Dzombak, D. A. & Morel, F. M. M. 1991. *Surface complexation modeling: hydrous ferric oxide*, John Wiley & Sons.
- El-Fattah, B. K. A., Moustafa, A. R. & Yousef, M. 2021. A new insight into the structural evolution of Rosetta Fault, eastern margin of Herodotus Basin, East Mediterranean. *Marine and Petroleum Geology*, 131, 105161.
- Elimelech, M. & Phillip, W. 2011. The Future of Seawater Desalination: Energy, Technology, and the Environment. *Science (New York, N.Y.)*, 333, 712-7.
- Ellinas, C. 2025. *Water scarcity in Cyprus* [Online]. Cyprus Economic Society Available: <https://cypruseconomicsociety.org/water-scarcity-in-cyprus/> [Accessed 12/10/2025].
- European Environment Agency (Eea). 2018. *Water is life* [Online]. [Accessed 8/10/2025].
- European Union 2020. Directive (EU) 2020/2184 of the European Parliament and of the Council of 16 December 2020 on the quality of water intended for human consumption (recast).

- Farquhar, M. L., Charnock Jm Fau - Livens, F. R., Livens Fr Fau - Vaughan, D. J. & Vaughan, D. J. 2002. Mechanisms of arsenic uptake from aqueous solution by interaction with goethite, lepidocrocite, mackinawite, and pyrite: an X-ray absorption spectroscopy study. *Environmental Science & Technology*, 36(8), 1757–1762.
- Flewelling, S. A. & Sharma, M. 2014. Constraints on Upward Migration of Hydraulic Fracturing Fluid and Brine. *Groundwater*, 52, 9-19.
- Ganat, T. 2020. *Technical Guidance for Petroleum Exploration and Production Plans*.
- Garg, S. & Singh, S. 2016. Modeling of arsenic transport in groundwater using MODFLOW: A case study. *International Journal of Geomatics and Geosciences*, 6, 56-81.
- Gholami, R., Shahraki, A. R. & Jamali Paghaleh, M. 2012. Prediction of Hydrocarbon Reservoirs Permeability Using Support Vector Machine. *Mathematical Problems in Engineering*, 2012, 670723.
- Golfinopoulos, S. K., Varnavas, S. P. & Alexakis, D. E. 2021. The Status of Arsenic Pollution in the Greek and Cyprus Environment: An Overview. *Water*, 13.
- Grohmann, S., Romero-Sarmiento, M.-F., Nader, F., Baudin, F. & Littke, R. 2019. Characterization of Potential Source Rock Intervals of Late Mesozoic to Cenozoic Age in the On- and Offshore Area of Cyprus and Their Impact on Petroleum Systems in the Eastern Mediterranean Sea.
- Guo, H., Stüben D Fau - Berner, Z. & Berner, Z. 2007. Adsorption of arsenic(III) and arsenic(V) from groundwater using natural siderite as the adsorbent. *J. Colloid Interface Sci.* , 315(1), 47–53.
- Hadjigeorgiou, P. 2022. Achieving Water Security – Cyprus Case. *Adaptation for Hydro-diplomacy and Water Security in the EMME Region*. Cyprus, Nicosia
- Islam, A. B. M. R., Maity, J. P., Bundschuh, J., Chen, C.-Y., Bhowmik, B. K. & Tazaki, K. 2013. Arsenic mineral dissolution and possible mobilization in mineral–microbe–groundwater environment. *J. Hazard. Mater.*, 262, 989-996.
- Kahveci, H. 2019. "Eastern Mediterranean Hydrocarbons: Regional Potential, Challenges Ahead, and the ‘Hydrocarbon-ization’ of the Cyprus Problem" PERCEPTIONS, Summer-Autumn 2017, Volume XXII, Number 2-3, pp. 31-56.
- Khan, M. Y. & Mandal, A. 2022. The impact of permeability heterogeneity on water-alternating-gas displacement in highly stratified heterogeneous reservoirs. *Journal of Petroleum Exploration and Production Technology*, 12, 871-897.
- Konstantinou, K., Christofi, C. & Rigas, M. 2014. Concentration and distribution of arsenic, cadmium, lead and mercury in Cyprus groundwater (2007–2013). Nicosia, Cyprus: Geological Survey Department, Republic of Cyprus.
- Kovalchuk, N. & Hadjistassou, C. 2019. Laws and principles governing fluid flow in porous media. *The European Physical Journal E*, 42, 56.

- Latham, S., Varslot, T. & Sheppard, A. 2008. Image Registration: Enhancing and Calibrating X-Ray Micro CT Imaging. *International Symposium of the Society of Core Analysts (SCA)*. Abu Dhabi, United Arab Emirates: Society of Core Analysts (SCA).
- Lee, D., Ruf, M., Karadimitriou, N., Steeb, H., Manousidaki, M., Varouchakis, E. A., Tzortzakis, S. & Yiotis, A. 2024. Development of stochastically reconstructed 3D porous media micromodels using additive manufacturing: numerical and experimental validation. *Scientific Reports*, 14, 9375.
- Li, H., Zhang, Q., Zheng, B., Chen, C., Wu, N., Guo, H., Zhang, Y., Zheng, Y., Li, X. & He, K. 2018. Nitrate-driven urban haze pollution during summertime over the North China Plain. *Atmospheric Chemistry and Physics*, 18, 5293-5306.
- Liang, J., Gurevich, B., Lebedev, M., Vialle, S., Yurikov, A. & Glubokovskikh, S. 2020. Elastic Moduli of Arenites From Microtomographic Images: A Practical Digital Rock Physics Workflow. *Journal of Geophysical Research: Solid Earth*, 125.
- Lin, Z. & Puls, R. 2000. Adsorption, Desorption and Oxidation of Arsenic Affected by Clay Minerals and Aging Process. *Environmental Geology*, 39, 753-759.
- López-Pamo, E., Baretino, D., Antón-Pacheco, C., Ortiz, G., Arránz, J. C., Gumiel, J. C., MartíNez-Pledel, B., Aparicio, M. & Montouto, O. 1999. The extent of the Aznalcóllar pyritic sludge spill and its effects on soils. *Science of The Total Environment*, 242, 57-88.
- Lu, P. & Zhu, C. 2011. Arsenic Eh–pH diagrams at 25°C and 1 bar. *Environmental Earth Sciences*, 62, 1673-1683.
- Lucia, F. J. 2007. *Carbonate Reservoir Characterization*, Berlin, Heidelberg, Springer
- Marle, C.-M. 2006. Henry Darcy et les écoulements de fluides en milieu poreux. *Oil & Gas Science and Technology - Revue de l'IFP*, 61.
- Matschullat, J. 2000. Arsenic in the geosphere — a review. *Science of The Total Environment*, 249, 297-312.
- Mehmani, A., Kelly, S. & Torres-Verdín, C. 2020. Leveraging digital rock physics workflows in unconventional petrophysics: A review of opportunities, challenges, and benchmarking. *Journal of Petroleum Science and Engineering*, 190, 107083.
- Michele Kambas & Kourtoglou, Y. 2025. Cyprus steps up desalination as worsening droughts parch the island. <https://www.reuters.com/sustainability/cop/cyprus-steps-up-desalination-worsening-droughts-parch-island-2025-09-02/>. [Accessed 12/10/2025].
- Missimer, T. M. & Maliva, R. G. 2018. Environmental issues in seawater reverse osmosis desalination: Intakes and outfalls. *Desalination*, 434, 198-215.
- Morrow, N. & Mason, G. 2001. Recovery of oil by spontaneous imbibition. *Current Opinion in Colloid & Interface Science*, 6, 321-337.

- Nadeau, P. H. & Ehrenberg, S. 2006. Sandstone vs. carbonate petroleum reservoirs: A global perspective on porosity-depth and porosity-permeability relationships: Reply. *American Association of Petroleum Geologists*, 90, 811-813.
- Nicolli, H. B., Suriano, J. M., Gomez Peral, M. A., Ferpozzi, L. H. & Baleani, O. A. 1989. Groundwater contamination with arsenic and other trace elements in an area of the pampa, province of Córdoba, Argentina. *Environmental Geology and Water Sciences*, 14, 3-16.
- Nikolaou, G., Neocleous, D., Christophi, C., Heracleous, T. & Markou, M. 2020. Irrigation Groundwater Quality Characteristics: A Case Study of Cyprus. *Atmosphere*, 11, 15.
- Oremland, R. S. & Stolz, J. F. 2003. The Ecology of Arsenic. *Science*, 300, 939-944.
- P. Ravenscroft, Brammer, H. & Chichester, K. R. 2009. *Arsenic Pollution: A Global Synthesis*, United Kingdom, Cambridge University Press.
- Palmer, C. D. & Wittbrodt, P. R. 1991. Processes affecting the remediation of chromium-contaminated sites. *Environmental Health Perspectives*, 92, 25 - 40.
- Pan, H., Feng, J.-C., Wang, B., Zhang, Y., Zhang, H., Xie, Y., Yang, Z.-F. & Zhang, S. 2025. Carbonate precipitation characteristics in porous media of deep-sea cold seep environment by X-ray CT imaging. *Deep Sea Research Part I: Oceanographic Research Papers*, 224, 104556.
- Parkhurst, D. & Appelo, T. 2013. *Description of input and examples for PHREEQC version 3—a computer program for speciation, batch-reaction, one-dimensional transport, and inverse geochemical calculations.*, United States (U.S.), U.S. Geological Survey.
- Parkinson, G. S. 2016. Iron oxide surfaces. *Surface Science Reports*, 71, 272-365.
- Peter A. Scholle, Don G. Bebout & Moore, C. H. 1983. *Carbonate Depositional Environments*, Tulsa, American Association of Petroleum Geologists.
- Pirot, E. M., Edilbi, A. N. F., Jader, R. F., Mamash, M. M., Jumaa, I. H., Hussein, R. M. & Sharif, D. M. 2025. Comparative study of the pore volume percentages of the carbonate core plug samples using direct, 2D techniques and exploratory data analysis. *Flow Measurement and Instrumentation*, 102, 102813.
- Podgorski, J. & Berg, M. 2020. Global threat of arsenic in groundwater. *Science*, 368, 845-850.
- Poursanidis, K., Sharanik, J. & Hadjistassou, C. 2024. World's largest natural gas leak from nord stream pipeline estimated at 478,000 tonnes. *iScience*, 27, 108772.
- Raats, P. a. C. 1973. Dynamics of Fluids in Porous Media. *Soil Science Society of America Journal*, 37.
- Randall, S. R., Sherman, D. M. & Ragnarsdottir, K. V. 2001. Sorption of As(V) on green rust and lepidocrocite: Surface complexes from EXAFS spectroscopy. *Geochimica et Cosmochimica Acta*, 65, 1015-1023.

- Ranjbarzadeh, R. & Sappa, G. 2025. Numerical and Experimental Study of Fluid Flow and Heat Transfer in Porous Media: A Review Article. *Energies*, 18, 976.
- Renard, F., Putnis, C. V., Montes-Hernandez, G., Ruiz-Agudo, E., Hovelmann, J. & Sarret, G. 2015. Interactions of arsenic with calcite surfaces revealed by in situ nanoscale imaging. *Geochimica et Cosmochimica Acta*, 159, 61-79.
- Roman Ross, G., Cuello, G., Turrillas, X., Fernandez Martinez, A. & Charlet, L. 2008. Arsenite sorption and co precipitation with calcite. *Chem. Geol.*, 255, 93-101.
- Rukh, S., Akhtar, M. S., Alshehri, F., Mehmood, A., Malik, K. M., Almadani, S., Khan, A. & Shahab, M. 2024. Modeling the Transport of Inorganic Arsenic Species through Field Soils: Irrigation and Soil Structure Effect. *Water*, 16, 386.
- Salah, M., Janjuhah, H., Sanjuan Girbau, J. & Maalouf, E. 2023. Impact of diagenesis and pore aspects on the petrophysical and elastic properties of carbonate rocks from southern Lebanon. *Bulletin of Engineering Geology and the Environment*, 82.
- Schicker, A., Gier, S., Schieber, J. & Krois, P. 2021. Diagenesis of the Malmian Mikulov Formation source rock, Vienna Basin: Focus on matrix and pores. *Marine and Petroleum Geology*, 129, 105082.
- Schlüter, S., Sheppard, A., Brown, K. & Wildenschild, D. 2014. Image processing of multiphase images obtained via X-ray microtomography: A review. *Water Resources Research*, 50, 3615-3639.
- Serkiz, S. M., Allison, J. D., Perdue, E. M., Allen, H. E. & Brown, D. S. 1996. Correcting errors in the thermodynamic database for the equilibrium speciation model MINTQA2. *Water Res.*, 30, 1930-1933.
- Shahid, M., Niazi, N. K., Dumat, C., Naidu, R., Khalid, S., Rahman, M. M. & Bibi, I. 2018. A meta-analysis of the distribution, sources and health risks of arsenic-contaminated groundwater in Pakistan. *Environmental Pollution*, 242, 307-319.
- Shankar, S., Shanker, U. & Shikha 2014. Arsenic contamination of groundwater: a review of sources, prevalence, health risks, and strategies for mitigation. *Sci. World J.*, 2014, 304524.
- Sharanik, J., Sarris, E. & Hadjistassou, C. 2025. Storage and Production Aspects of Reservoir Fluids in Sedimentary Core Rocks. *Geosciences*, 15, 386.
- Smedley, P. L. & Kinniburgh, D. G. 2002. A review of the source, behaviour and distribution of arsenic in natural waters. *Applied Geochemistry*, 17, 517-568.
- Smedley, P. L. & Kinniburgh, D. G. 2013. Arsenic in groundwater and the environment. *Essentials of Medical Geology* 279-310.
- Sø, H. U., Postma, D., Jakobsen, R. & Larsen, F. 2012. Competitive adsorption of arsenate and phosphate onto calcite; experimental results and modeling with CCM and CD-MUSIC. *Geochimica et Cosmochimica Acta*, 93, 1-13.

- Sø, H. U., Postma, D. J., Jakobsen, R. & Larsen, F. 2008. Sorption and desorption of arsenate and arsenite on calcite. *Geochimica et Cosmochimica Acta*, 72, 5871-5884.
- Stanton, S. & Macgregor, D. 2018. Petroleum Potential of the Herodotus Basin: Applying Regional Analogues to Predict Plays and Reduce Potential Risk. *AAPG International Conference and Exhibition*. Athens, Greece: American Association of Petroleum Geologists.
- Steefel, C. & Lasaga, A. 1994. A Coupled Model for Transport of Multiple Chemical-Species and Kinetic Precipitation Dissolution Reactions with Application to Reactive Flow in Single-Phase Hydrothermal Systems. *American Journal of Science*, 294, 529-592.
- Steefel, C. I., Appelo, C. a. J., Arora, B., Jacques, D., Kalbacher, T., Kolditz, O., Lagneau, V., Lichtner, P. C., Mayer, K. U., Meeussen, J. C. L., Molins, S., Moulton, D., Shao, H., Šimůnek, J., Spycher, N., Yabusaki, S. B. & Yeh, G. T. 2015. Reactive transport codes for subsurface environmental simulation. *Computational Geosciences*, 19, 445-478.
- Suwanu .2021. Country Report: Cyprus. SUWANU Europe <https://suwanu-europe.eu/cyprus>.
- Tiab, D. & Donaldson, E. 2003. Petrophysics: Theory and Practice of Measuring Reservoir Rock and Fluid Transport Properties: Second Edition.
- Tzanakakis, V. A., Angelakis, A. N., Paranychianakis, N. V., Dialynas, Y. G. & Tchobanoglous, G. 2020. Challenges and Opportunities for Sustainable Management of Water Resources in the Island of Crete, Greece. *Water*, 12.
- Varfolomeev, I., Yakimchuk, I. & Safonov, I. 2019. An Application of Deep Neural Networks for Segmentation of Microtomographic Images of Rock Samples. *Computers*, 8, 72.
- Vital, M., Martínez, D. E., Babay, P., Quiroga, S., Clément, A. & Daval, D. 2019. Control of the mobilization of arsenic and other natural pollutants in groundwater by calcium carbonate concretions in the Pampean Aquifer, southeast of the Buenos Aires province, Argentina. *Science of The Total Environment*, 674, 532-543.
- Wang, C., Tian, L., Sun, C., Deng, Y., Zhou, Y. & Nie, X. 2025. Multi-scale characterization of tight carbonate rocks based on digital cores. *Frontiers in Earth Science*, Volume 13 - 2025.
- Wang, Z., Hu, M. & Steefel, C. 2024. Pore-Scale Modeling of Reactive Transport with Coupled Mineral Dissolution and Precipitation. *Water Resources Research*, 60, e2023WR036122.
- Water Development, D. 2021. Overview of Significant Water Management Issues (WFD, Cyprus). Nicosia, Cyprus: Ministry of Agriculture, Rural Development and Environment.
- Welch, A. 2000. Risk-Based Drinking Water Standards: A Challenge for the Hydrologic Community. *Groundwater*, 38, 481-481.
- Worden, R. & Burley, S. 2009. Sandstone Diagenesis: The Evolution of Sand to Stone.

- Xevgenos, D., Marcou, M., Louca, V., Avramidi, E., Ioannou, G., Argyrou, M., Stavrou, P., Mortou, M. & Küpper, F. 2021. Desalination and Water Treatment Aspects of environmental impacts of seawater desalination: Cyprus as a case study. *Desalination and Water Treatment*, 211, 15-30.
- Xie, M., Mayer, K. U., Claret, F., Alt-Epping, P., Jacques, D., Steefel, C., Chiaberge, C. & Simunek, J. 2015. Implementation and evaluation of permeability-porosity and tortuosity-porosity relationships linked to mineral dissolution-precipitation. *Computational Geosciences*, 19, 655-671.
- Xu, T., Spycher, N., Sonnenthal, E., Zhang, G., Zheng, L. & Pruess, K. 2011. TOUGHREACT Version 2.0: A simulator for subsurface reactive transport under non-isothermal multiphase flow conditions. *Computers & Geosciences*, 37, 763-774.
- Yang, L., Yu, L., Chen, D., Liu, K., Yang, P. & Li, X. 2020. Effects of Dolomitization on Porosity during Various Sedimentation-Diagenesis Processes in Carbonate Reservoirs. *Minerals*, 10, 574.
- Yoon, H., Kang, Q. & Valocchi, A. 2015. Lattice Boltzmann-Based Approaches for Pore-Scale Reactive Transport. *Reviews in Mineralogy and Geochemistry*, 80, 393-431.
- Young, A. H. & Kabala, Z. J. 2024. Hydrodynamic Porosity: A New Perspective on Flow through Porous Media, Part I. *Water*, 16, 2158.
- Zachariadis, T. 2010. Residential Water Scarcity in Cyprus: Impact of Climate Change and Policy Options. *Water*, 2, 788-814.
- Zanganeh Kamali, M., Davoodi, S., Ghorbani, H., Wood, D. A., Mohamadian, N., Lajmorak, S., Rukavishnikov, V. S., Taherizade, F. & Band, S. S. 2022. Permeability prediction of heterogeneous carbonate gas condensate reservoirs applying group method of data handling. *Marine and Petroleum Geology*, 139, 105597.
- Zhang, C., Oostrom, M., Wietsma, T. W., Grate, J. W. & Warner, M. G. 2011. Influence of Viscous and Capillary Forces on Immiscible Fluid Displacement: Pore-Scale Experimental Study in a Water-Wet Micromodel Demonstrating Viscous and Capillary Fingering. *Energy & Fuels*, 25, 3493-3505.
- Zhang, H., Gao, M., Liu, C., Liu, J., Yue, G. & Zhang, J. 2022. Dynamic prediction of in-situ SO₂ emission and operation optimization of combined desulfurization system of 300 MW CFB boiler. *Fuel*, 324, 124421.
- Zhong, X., Jiang, X., He, H., Zhang, W. & Meng, C. 2023. Application of sequential extraction for analyzing source and sink of uranium in Huanghe River sediments, China. *Journal of Oceanology and Limnology*.
- Zhou, Y., Wan, X., Lei, M. & Chen, T. 2024. Arsenic release during groundwater recharge and effects of coexisting ions in a typical inland basin with high arsenic concentration: Modeling and batch experiment. *Science of The Total Environment*, 950, 175359.
- Zhu, C. & Anderson, G. 2002. *Environmental Applications of Geochemical Modeling*, Cambridge, Cambridge University Press.

